Single Molecule Studies of β-amyloid(1-40) peptide in Alzheimer's Disease

by

Hao Ding

A dissertation submitted in partial fulfillment
of the requirements for the degree of
Doctor of Philosophy
(Biophysics)
in The University of Michigan
2009

Doctoral Committee:

Professor Duncan G. Steel, Co-Chair
Professor Ari Gafni, Co-Chair
Professor Charles L. Brooks III
Professor Ayyalusamy Ramamoorthy
Assistant Professor Matthew T. Chapman

ACKNOLEDGEMENTS

First of all, I would like to express my deepest gratitude to my advisors, Duncan Steel and Ari Gafni. Without their support and guidance throughout my Ph.D. study, I would not be able to accomplish anything. They gave me the greatest freedom and patience to follow my interests in science. From them, I learnt not only how to become a better scientist, but also how to become a better person. I felt extremely lucky to have them as my mentors throughout my graduate career. I would also like to thank the rest of my dissertation committee: Charles Brooks, Ayyalusamy Ramamoorthy, and Matt Chapman for their advice during my study.

I am also extremely grateful to all my wonderful colleagues in the Gafni-Steel lab. I really enjoyed working with everyone: Joe Schauerte, Kathleen Wisser, Jue Shi, Jeff Brender, Osman Akcakir, Joe Dertouzos, Pamela Wong, Edgar Lee, Narin Pattaramanon, Yu-Chung Chang, Justin Klein, Robin Johnson, Jamie Van Etten, Navneet Sangha, and Liz Shtrahman. I would especially like to thank Joe Schauerte for helping me on everything in my research, and Kathleen Wisser for helping me taking care of lab activities.

I would also like to thank all the students, staff, and faculties in the Biophysics Graduate Program for all their help and support during my time here.

Last, I would also like to thank my family and friends for always being with me and supporting me. I would especially like to thank my beautiful wife, Jie Xu, for the love and care she has given me. My life would not be complete without her.

Thank you to everyone who has helped me along my journey over the past several years. It has been an important and wonderful chapter in my life!

TABLE OF CONTENTS

CHAPTER

LIST OF FIGURES

Figures

LIST OF APPENDICES

Appendices

ABSTRACT

The formation of β-amyloid fibrils in patient's brain tissues has been the hallmark of Alzheimer's disease. However, recent evidence suggests the early oligomers of β-amyloid peptides are the origin of neurotoxicity. While the importance of identifying the toxic oligomeric species is widely recognized, its realization has been challenging because these oligomers are metastable, occur at low concentration, and are characterized by a high degree of heterogeneity.

This doctoral thesis focuses on the study of β-amyloid(1-40) oligomer and its interaction with lipid membrane through a novel single molecule approach. In the first part of the thesis (Chapter II & III), a single molecule methodology based on photobleaching is developed to identify the β-amyloid(1-40) oligomeric species. By directly counting the photobleaching steps in the fluorescence, we can determine the number of subunits in individual β-amyloid(1-40) oligomers. The results are further analyzed by comparison with stochastic simulations to show that the variability seen in the size of photobleaching steps can be explained by assuming random dipole orientations for the fluorophores in a given oligomer. In addition, by accounting for biasing the oligomer size distribution due to thresholding, the results can be made more quantitative, and show good agreement with the oligomer size distribution determined

using HPLC gel filtration.

In the second part of this thesis (Chapter IV), the interaction of β-amyloid(1-40) peptide with supported planar lipid membrane is investigated in detail through single molecule imaging techniques. The evolution of β-amyloid species on lipid membranes is monitored for up to a few days. The results indicate a tight, uniform binding of β-amyloid(1-40) peptides onto lipid membranes, followed by oligomer formation. The size of the β-amyloid(1-40) oligomers and the rate of their formation are highly dependent on the peptide concentration. Our results suggest there are two different pathways of oligomer formation, which lead to drastically different oligomeric species formed in the membrane.

CHAPTER I

Introduction to Alzheimer's disease and β-amyloid Peptides

1.1 Alzheimer's disease (AD)

Alzheimer's disease (AD), also called Senile Dementia of the Alzheimer Type, is the most common form of dementia in humans. It is an irreversible, progressive neurodegenerative disease that gradually leads to the loss of memory, thinking skills, and the ability to carry out daily activities. Eventually the destruction of brain functions is fatal. According to recent estimates, as many as 2.4 to 4.5 million people in the U.S. (1), and 26.6 million people worldwide, have developed Alzheimer's disease (2), and these numbers are expected to quadruple by 2050 (3).

Alzheimer's disease was first discovered in 1906 by Alois Alzheimer, a Bavarian psychiatrist (4). He examined the brain tissues of a woman who died of an unusual mental illness, and found many abnormal clumps and tangled bundles of fibers, which were later termed amyloid/senile plaques and neurofibrillary tangles, respectively. Since then, these two classical brain lesions have become the major neuropathological features of Alzheimer's disease. In the 1960s, the use of electron microscopy allowed the ultra-structures of these plaques and tangles to be studied, revealing the fine fibrillar structures of these brain lesions (5-8).

With the advances in biochemical pathology, the compositions of the plaques and tangles were identified in the 1980s. It was found that the amyloid plaques mainly contain extracellular deposits of β-amyloid peptides (9-12), while the neurofibrillary tangles are mainly composed of hyperphosphorylated tao proteins (13-16). Both β-amyloid peptides and tao proteins are present in a highly ordered and aggregated form in the plaques and tangles.

Due to the fact that amyloid plaques and neurofibrillary tangles can occur independently of each other, and that neurofibrillary tangles are also present in many less common neurodegenerative diseases in the absence of β-amyloid deposition, it has been suggested that the tangles are likely to occur as a secondary response to the injury of neuronal cells (17, 18). Therefore, Alzheimer's disease studies have primarily focused on β-amyloid peptides.

Indeed, with extensive research on β-amyloid peptides over the years, more evidence was gained in support of their direct involvement in Alzheimer's disease:

1. Genetic studies of the familial forms of early-onset Alzheimer's disease have uncovered several point mutations in the β-amyloid peptide sequence, e.g. Arctic (E22G), Dutch (E22Q), Flemish (A21G), and Iowa (D23N) mutant peptides (19-21). It has been shown that these peptides have greater propensity for oligomerization and aggregation, and are directly linked to the genetically inherited forms of the disease.

2. The direct incubation of β-amyloid peptides with neuronal cells, or the overexpression of amyloid precursor proteins (APP, whose proteolysis generates β-amyloid peptides), results in cell death (22-24).
3. The direct injection of β-amyloid peptides into mice, or the overexpression of amyloid precursor proteins, results in significant neurodegeneration and cognitive deficits in mice (25, 26).

Thus, it is clear that β-amyloid peptides play a critical role in the development of Alzheimer's disease.

1.2 β-amyloid peptides

1.2.1 The origin of β-amyloid peptides

β-amyloid is a small (~4kDa), natively unfolded peptide, which is normally present in both cerebrospinal fluid and blood at extremely low physiological concentrations (nanomolar or less). It is formed by the sequential cleavage of a transmembrane protein, amyloid precursor protein (APP). Although the physiological function of this protein remains unclear, it is known that the cleavage of amyloid precursor protein by β-secretase and then γ-secretase yields β-amyloid peptides and AICD (Amyloid Precursor Protein Intracellular Domain), whereas the cleavage by α-secretase and γ-secretase yields two relatively benign fragments, P3 and AICD (see figure 1.1). The β-amyloid peptide portion of the cleaved amyloid precursor protein is then released extracellularly.

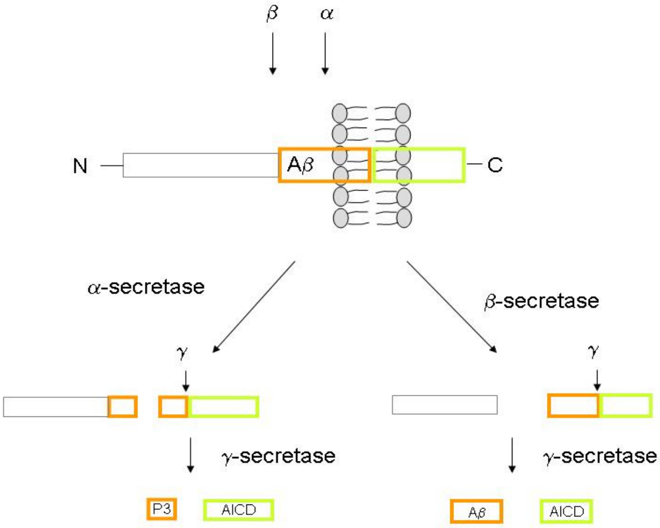

Figure 1.1: Proteolytic processing of amyloid precursor protein (APP) by secretase. The cleavage of amyloid precursor protein by α-secretase followed by γ-secretase cleavage yields the benign P3 and AICD fragments, whereas the cleavage by β-secretase followed by γ-secretase yields β-amyloid peptides and AICD.

The variability in the cleavage site of γ-secretase creates several β-amyloid peptide forms, with lengths varying from 39 to 43 amino acids. Among them, the 40 residue β-amyloid(1-40) and the 42 residue β-amyloid(1-42) are the most common forms (see figure 1.2 for their sequences). Both β-amyloid(1-40) and β-amyloid(1-42) are present in amyloid plaques. While β-amyloid(1-40) is much more abundant, β-amyloid(1-42) is much more amyloidogenic, which means it can oligomerize and fibrilize much more rapidly than β-amyloid(1-40).

β-amyloid(1-40): DAEFRHDSGYEVHHQKLVFFAEDVGSNKGAIIGLMVGGVV
β-amyloid(1-42): DAEFRHDSGYEVHHQKLVFFAEDVGSNKGAIIGLMVGGVVIA

Figure 1.2: Sequences of β-amyloid(1-40) and β-amyloid(1-42).

1.2.2 Oligomerization of β-amyloid peptides

The small intermediates formed in the aggregation process of β-amyloid peptides are commonly called oligomers. However, some ambiguity of this terminology exists in the amyloid field. To date, many types of β-amyloid oligomers have been documented and described in the literature, e.g. protofibrils (27-30), annular structures (31, 32), and Aβ-derived diffusible ligands (ADDLs) (33, 34). In general, β-amyloid oligomers are defined as the peptide assemblies that are still soluble in aqueous solution upon high-speed centrifugation.

The investigation of β-amyloid oligomers revealed that they are heterogeneous, and exist in dynamic equilibrium. This has been demonstrated by gel filtration chromatography (see figure 1.3, data obtained by Wong, P.). The elusion profile of β-amyloid oligomers clearly shows the existence of multiple peaks, indicating the heterogeneity within the oligomers. The dynamic equilibrium of β-amyloid oligomers is demonstrated by an immediate re-run of the collected middle fraction (indicated by the arrow in the figure) through the same gel-filtration column. Instead of showing the original single peak, the re-run profile shows multiple peaks again (figure 1.3(b)). The good alignment of the peaks between the consecutive runnings suggests the same species exist in the oligomer mixture. The experimental detail and chromatogram analysis can be found in Chapter III.

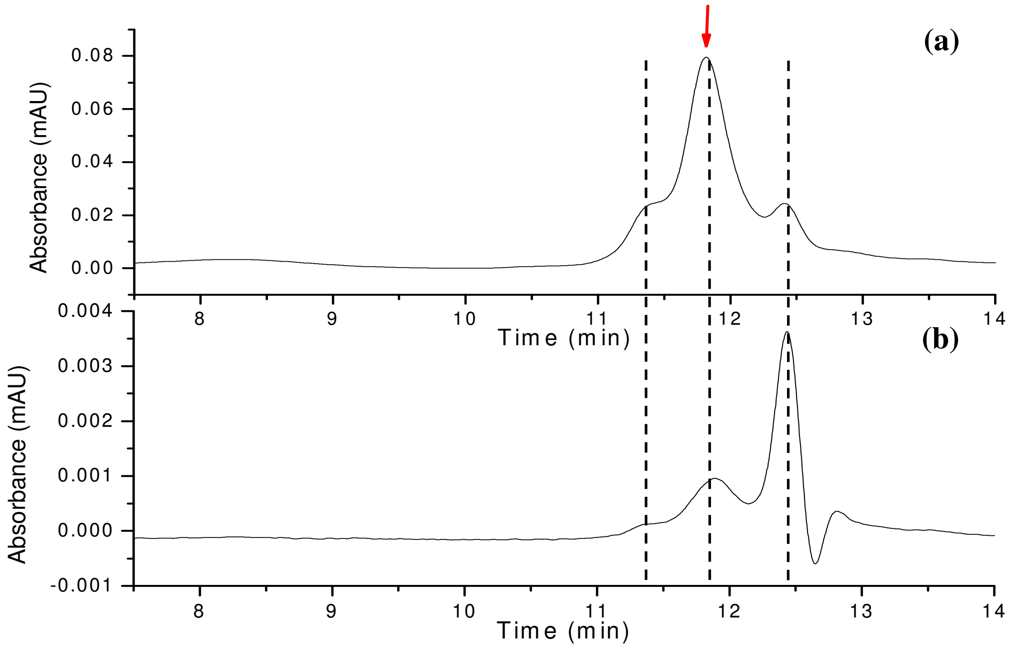

Figure 1.3: Heterogeneity and dynamic equilibrium revealed by gel-filtration chromatography. (a) The elution profile of β-amyloid oligomers through the gel-filtration column. The red arrow indicates the middle fraction was collected. (b) The collected middle fraction was re-run through the column immediately. The peaks in the elution profiles between the consecutive runnings are well aligned to each other, suggesting the same oligomeric species. (Data in courtesy of Wong, P.)

1.2.3 Fibrilization of β-amyloid peptides

β-amyloid peptides can self-assemble into extremely large and highly ordered fibrillar structures. Due to the existence of a lag phase in fibril formation, the fibrilization process of β-amyloid peptides is generally believed to be nucleation dependent. The nucleation process involves the association and dissociation of β-amyloid peptides in forming large oligomers that can nucleate fibril formation. Once the oligomers reach the critical size, a fast, linear elongation of the aggregates can occur via the addition of β-amyloid peptides to the ends. Since fibrils cannot revert back to soluble oligomeric species, fibrilization of β-amyloid peptides is an irreversible process.

The typical appearance of β-amyloid fibrils under an electron microscope is of long, thin filaments with 6-12nm in diameter (35-37). Both X-ray diffraction and NMR studies have revealed the highly ordered, β-sheet rich structure of β-amyloid fibrils (38-41). The structure contains a unique quaternary, intermolecular cross β-sheet that spans across more than one molecule, making the fibril a 'β-sheet of β-sheets' (see figure 1.4) (39).

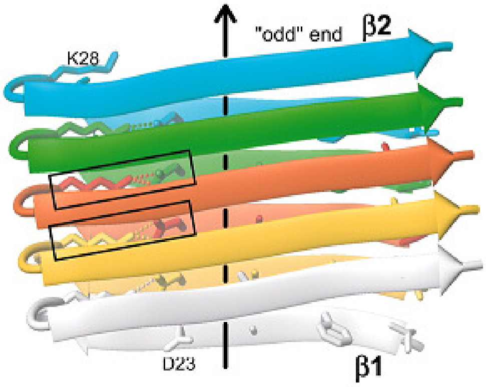

Figure 1.4: NMR structure of β-amyloid(1-42) fibrils. The fibrillar structure consists of unique parallel arrangement of in-register intermolecular β-sheets. (Figure from Luhrs T., et al. (2005) *Proc. Natl. Acad. Sci. USA 102*, 17342-17347.)

A diverse set of peptides and proteins with the capability to form fibrillar structures has been identified. Surprisingly, little sequence homology has been found. Furthermore, several non-amyloidogenic proteins have also been shown to be able to form fibrils under certain conditions (42). Therefore, the fibrilization process has been suggested to be a rather fundamental motif of the polypeptide backbone (42, 43).

1.3 β-amyloid neurotoxicity hypotheses

Although it has been shown that β-amyloid peptides are neurotoxic, and are directly linked to Alzheimer's disease, the underlying mechanism remains unclear. Over the years, different hypotheses for β-amyloid neurotoxicity have been developed.

1.3.1 Original amyloid hypothesis

Since neuropathology studies have shown the existence of amyloid plaques in the brain tissues of Alzheimer's disease patients, these amyloid plaques, which are mainly composed of mature β-amyloid fibrils, have been traditionally linked to the origin of neurotoxicity.

In this amyloid hypothesis, it was proposed that β-amyloid deposits are the fundamental cause of the disease (44, 45). However, recent studies do not agree with the hypothesis. It has been found that, in transgenic animals that over-express amyloid precursor proteins, neuronal abnormalities and cognitive deficits start to appear well before amyloid plaques can be detected (46-48). Furthermore, little correlation between amyloid plaque density and clinical severity of dementia has been found (49, 50). In some cases, a significant amount of amyloid plaques were found in the brain tissues from patients without Alzheimer's disease, whereas in other cases, opposite scenarios were observed in which few amyloid plaques were detected in the brain tissues from patients with severe Alzheimer's disease.

Thus, research interests in amyloid plaques or fibrils have gradually faded, and new hypotheses involving the small oligomeric species of β-amyloid peptides have been developed.

1.3.2 Pore formation hypothesis

Recently, numerous studies have suggested that β-amyloid oligomers are the origin of neurotoxicity, potentially through membrane permeabilization (51-57). Therefore, a new hypothesis was developed, in which β-amyloid oligomers induce neurotoxicity by forming pores/channels in the cell membranes (see figure 1.5). These pores allow a rapid, uncontrolled influx of ions, particularly calcium ions, into the neuronal cells, which may directly lead to the cell death, or trigger the apoptosis signaling pathway (58).

Several studies have provided support for the pore formation hypothesis:

1. In a recent study, a significant increase of the calcium influx into neuronal cells was observed upon incubation with β-amyloid oligomers, supporting the idea of small oligomers being the pore forming species in the membrane (51, 59).
2. Membrane leakage or conductivity in lipid bilayers upon incubation with β-amyloid oligomers was consistently observed by several groups (52, 60-63).
3. AFM images of β-amyloid oligomers reconstituted in lipid membranes revealed annular structures, which consist of only a few monomeric units and resemble the pore formation in the membrane (56, 63).

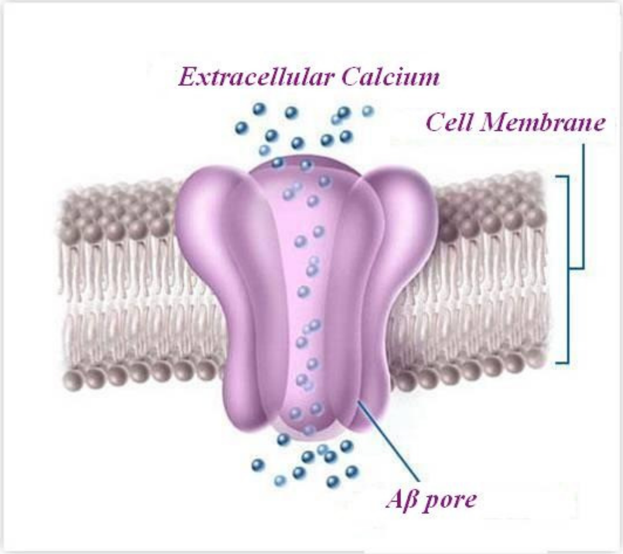

Figure 1.5: Illustration of the pore formation hypothesis.

1.4 Single molecule study of β-amyloid oligomers

Despite the recent emphasis on β-amyloid oligomers, the studies of these small oligomers have been challenging for traditional techniques, because they are metastable, occur at low concentration, and are characterized by a high degree of heterogeneity.

Single molecule techniques hold the promise to study these oligomers at their physiological conditions. With the capability to detect one molecule at a time, β-amyloid oligomer formation and oligomer-membrane interaction can be directly monitored and characterized. Therefore, this thesis opens up new opportunities for Alzheimer's disease to be studied at an earlier stage and at a more fundamental level. In Chapter II, a single molecule methodology based on photobleaching is developed. Chapter III presents a quantitative study of β-amyloid oligomers using the single molecule photobleaching methodology. In Chapter IV, the interaction between β-amyloid peptide and lipid membrane is investigated in detail through single molecule imaging techniques.

In all the studies presented in this thesis, β-amyloid(1-40) is used as the model peptide because it is the more abundant species between the two isoforms, and its slower aggregation properties also facilitate the studies of oligomerization and peptide-membrane interaction.

1.5 Fluorescence labeling of β-amyloid peptide

Since fluorescence detection is essential in our single molecule studies of β-amyloid peptide, it is critical to confirm that the fluorescence labeling of β-amyloid(1-40) does not alter the properties of the peptide.

1.5.1 Structural studies suggest the peptide being minimally perturbed by the labeling

According to the 3D structure of β-amyloid peptide recently determined by NMR studies (39) (see figure 1.4), the N terminus where the fluorophore resides has a rather flexible structure, which suggests the peptide structure should not be significantly altered by the labeling.

1.5.2 Both unlabeled and labeled β-amyloid(1-40) peptides permeabilize membranes

Membrane permeabilization studies often use lipid vesicles as model systems. To measure the permeabilization ability of β-amyloid(1-40) peptides, lipid vesicles were made containing high concentrations of self-quenching fluorescent dyes, 5(6)-

carboxyfluorescein. With intact lipid vesicles, the fluorescence from carboxyfluorescein is largely quenched; however, upon membrane permeabilization, the carboxyfluorescein molecules are released from the vesicles, resulting in a large increase (3-5 folds) in fluorescence due to the disappearance of self-quenching. Figure 1.6 shows the membrane permeabilization by both unlabeled and HiLyte Fluor^{TM} 488 labeled β-amyloid(1-40) peptides (data obtained by Wong, P.). Very similar results, including the percentage and the rate of the leakage, were observed, confirming that the fluorescent labeling does not affect the permeabilization ability of the peptide.

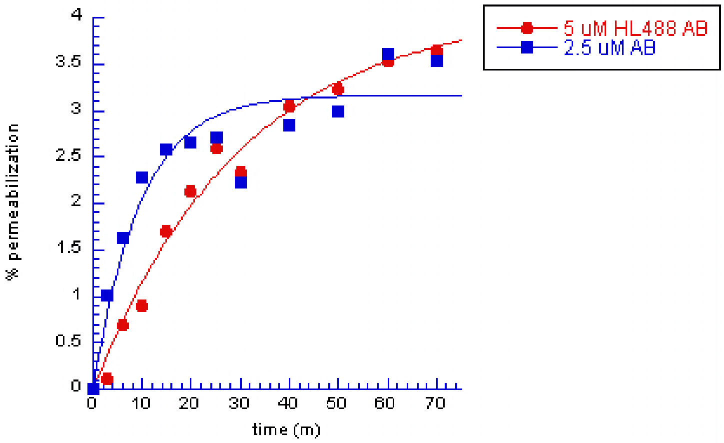

Figure 1.6: Membrane permeabilization by both unlabeled and HiLyte Fluor^{TM} 488 labeled β-amyloid(1-40) peptides. (Unpublished data in courtesy of Wong, P.)

1.5.3 Both unlabeled and labeled β-amyloid(1-40) peptides form fibrils

Imaging of fibrils by transmission electron microscopy (TEM) is a common and direct method to study the fibril formation of β-amyloid peptides. We used TEM to image the fibrils formed by both unlabeled β-amyloid(1-40) and HiLyte Fluor^{TM} 488 labeled β-amyloid(1-40), and compared them side by side (see figure 1.7, data obtained by Lee, E. L.). These images confirm that HiLyte Fluor^{TM} 488 β-amyloid(1-40) is able to form fibrils, and the time scale of its fibril formation as well as the morphology of the fibrils are similar to those of the unlabeled β-amyloid(1-40).

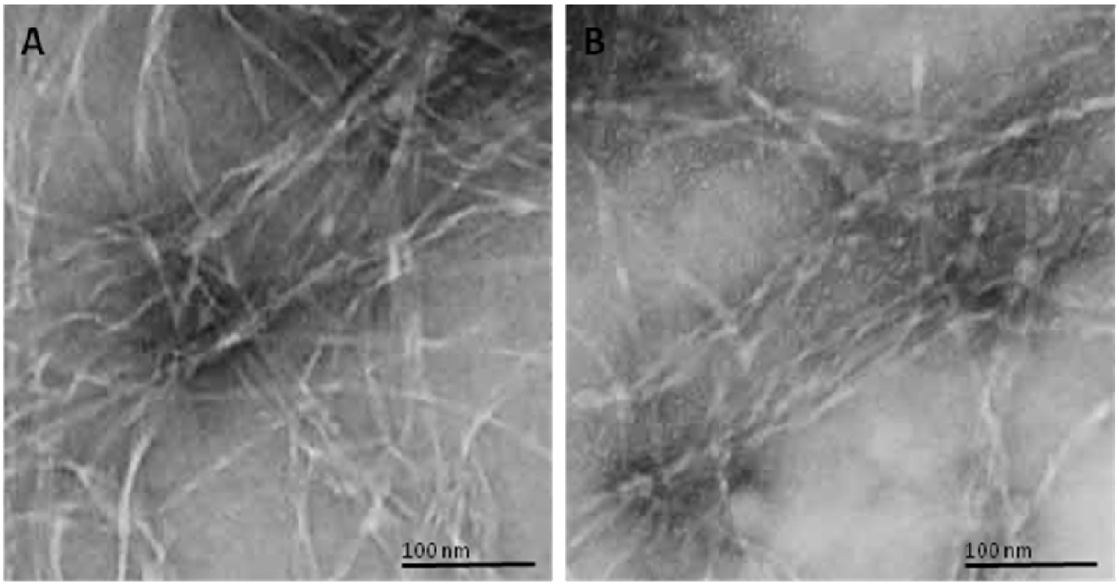

Figure 1.7: Fibril morphology comparison: unlabeled (A) *vs.* HiLyte Fluor^{TM} 488 labeled β-amyloid(1-40) (B). Both unlabeled and labeled β-amyloid(1-40) peptides were incubated for six days and imaged with transmission electron microscope. (Unpublished data in courtesy of Lee, E. L.)

Reference

1. (2009) National Institute on Aging.

2. (2007) World population prospects: the 2006 revision, highlights, *Working Paper No. ESA/P/WP.202. Population Division, Department of Economic and Social Affairs, United Nations.*

3. Brookmeyer, R., Johnson, E., Ziegler-Graham, K., and Arrighi, M. H. (2007) Forecasting the global burden of Alzheimer's disease, *Alzheimer's and Dementia 3*, 186–91.

4. Alzheimer, A., Stelzmann, R. A., Schnitzlein, H. N., and Murtagh, F. R. (1995) An English translation of Alzheimer's 1907 paper, "Uber eine eigenartige Erkankung der Hirnrinde", Clin Anat 8, 429-431.

5. Kidd, M. (1963) Paired Helical Filaments in Electron Microsocpy of Alzheimer's Disease, *Nature 197*, 192-193.

6. Kidd, M. (1964) Alzheimer's Disease: An Electron Microscopic Study, *Brain 86*, 309-310.

7. Terry, R. (1963) The Fine Structure of Neurofibrillary Tangles in Alzheimer's Disease, *J. Neuropathol. Exp. Neurol. 22*, 629-642.

8. Terry, R., Gonatas, N. K., and Weiss, M. (1964) Ultrastructural Studies in Alzheimer's Presenile Dementia, *Am. J. Pathol. 44*, 269-281.

9. Glenner, G. G., and Wong, C. W. (1984) Alzheimer's disease: initial report of the purification and characterization of a novel cerebrovascular amyloid protein, *Biochem. Biophys. Res. Commun. 120*, 885-890.

10. Gorevic, P., Goni, F., Pons-Estel, B., Alvarez, F., Peress, R., and Frangione, B. (1986) Isolation and partial characterization of neurofibrillary tangles and amyloid plaque cores in Alzheimer's disease: immunohistological studies, *J. Neuropathol. Exp. Neurol. 45*, 647-664.

11. Masters, C. L., Simms, G., Weinman, N. A., Multhaup, G., McDonald, B. L., and Beyreuther, K. (1985) Amyloid plaque core protein in Alzheimer disease and Down syndrome, *Proc. Natl. Acad. Sci. USA 82*, 4245-4249.

12. Selkoe, D. J., Abraham, C. R., Podlisny, M. B., and Duffy, L. K. (1986) Isolation of low-molecular-weight proteins from amyloid plaque fibers in Alzheimer's disease, *J. Neurochem. 146*, 1820-1834.

13. Grundke-Iqbal, I., Iqbal, K., Tung, Y. C., Quinlan, M., Wisniewski, H. M., and Binder, L. I. (1986) Abnormal phosphorylation of the microtubule-associated protein τ (tau) in Alzheimer cytoskeletal pathology, *Proc. Natl. Acad. Sci. USA 83*, 4913-4917.

14. Kosik, K. S., Joachim, C. L., and Selkoe, D. J. (1986) Microtubule-associated protein, tau, is a major antigenic component of paired helical filaments in Alzheimer's disease, *Proc. Natl. Acad. Sci. USA 83*, 4044-4048.

15. Nukina, N., and Ihara, Y. (1986) One of the antigenic determinants of paired helical filaments is related to tau protein, *J. Biochem. 99*, 1541-1544.

16. Wood, J. G., Mirra, S. S., Pollock, N. L., and Binder, L. I. (1986) Neurofibrillary tangles of Alzheimer's disease share antigenic determinants with the axonal microtubule-associated protein tau, *Proc. Natl. Acad. Sci. USA 83*, 4040-4043.

17. Terry, R. D., Hansen, L. A., DeTeresa, R., Davies, P., Tobias, H., and Katzman, R. (1987) Senile dementia of the Alzheimer type without neocortical neurofibrillary tangles, *J. Neuropath. Exp. Neurol. 46*, 262-268.

18. Selkoe, D. J. (2001) Alzheimer's Disease: Genes, Proteins, and Therapy, *Physiol. Rev. 81*, 741-766.

19. Revesz, T., Ghiso, J., Lashley, T., Plant, G., Rostagno, A., Frangione, B., and Holton, J. L. (2003) Cerebral amyloid angiopathies: a pathologic, biochemical, and genetic view, *J. Neuropathol. Exp. Neurol. 62*, 885–898.

20. Maia, L. F., Mackenzie, I. R. A., and Feldman, H. H. (2007) Clinical phenotypes of cerebral amyloid angiopathy, *J. Neurol. Sci. 15*, 23–30.

21. Yamada, M. (2000) Cerebral amyloid angiopathy: an overview, *Neuropathology 1*, 8–22.

22. Harper, J. D., and Lansbury, P. T., Jr. (1997) Models of amyloid seeding in Alzheimer's disease and scrapie: mechanistic truths and physiological consequences of the time-dependent solubility of amyloid proteins, *Annu Rev Biochem 66*, 385-407.

23. Selkoe, D. J. (1991) The molecular pathology of Alzheimer's disease, *Neuron 6*, 487-498.

24. LaFerla, F. M., and Oddo, S. (2005) Alzheimer's disease: Abeta, tau and synaptic dysfunction, *Trends Mol Med 11*, 170-176.

25. Chauhan, N. B., and Siegel, G. J. (2002) Reversal of amyloid beta toxicity in Alzheimer's disease model Tg2576 by intraventricular antiamyloid beta antibody, J Neurosci Res 69, 10-23.

26. Banks, W. A., Farr, S. A., Morley, J. E., Wolf, K. M., Geylis, V., and Steinitz, M. (2007) Anti-amyloid beta protein antibody passage across the blood-brain barrier in the SAMP8 mouse model of Alzheimer's disease: an age-related selective uptake with reversal of learning impairment, Experimental neurology 206, 248-256.

27. Harper, J. D., Wong, S. S., Lieber, C. M. and Lansbury, P. T. (1997) Observation of metastable Aβ amyloid protofibrils by atomic force microscopy, *Chem. Biol. 4*, 119–125.

28. Hartley, D. M., Walsh, D. M., Ye, C. P., Diehl, T., Vasquez, S., Vassilev, P. M., Teplow, D. B., and Selkoe, D. J. (1999) Protofibrillar intermediates of amyloid-β protein induce acute electrophysiological changes and progressive neurotoxicity in cortical neurons, *J. Neurosci. 19*, 8876–8884.

29. Walsh, D. M., Lomakin, A., Benedek, G. B., Condron, M. M. and Teplow, D. B. (1997) Amyloid β-protein fibrillogenesis. Detection of a protofibrillar intermediate, *J. Biol. Chem. 272*, 22364–22372.

30. Walsh, D. M., Hartley, D. M., Kusumoto, Y., Fezoui, Y., Condron, M. M., Lomakin, A., Benedek, G. B., Selkoe, D. J., and Teplow, D. B. (1999) Amyloid β-protein fibrillogenesis. Structure and biological activity of protofibrillar intermediates, *J. Biol. Chem. 274*, 25945–25952.

31. Bitan, G., Kirkitadze, M. D., Lomakin, A., Vollers, S. S., Benedek, G. B., and Teplow, D. B. (2003) Amyloid β-protein (Aβ) assembly: Aβ40 and Aβ42 oligomerize through distinct pathways, *Proc. Natl Acad. Sci. USA 100*, 330–335.

32. Lashuel, H. A., Hartley, D., Petre, B. M., Walz, T. and Lansbury, P. T. Jr. (2002) Neurodegenerative disease: amyloid pores from pathogenic mutations, *Nature 418*, 291.

33. Lambert, M. P., Barlow, A. K., Chromy, B. A., Edwards, C., Freed, R., Liosatos, M., Morgan, T. E., Rozovsky, I., Trommer, B., Viola, K. L., Wals, P., Zhang, C., Finch, C. E., Krafft, G. A., and Klein, W. L. (1998) Diffusible, nonfibrillar ligands derived from Aβ1–42 are potent central nervous system neurotoxins, *Proc. Natl Acad. Sci. USA 95*, 6448–6453.

34. Gong, Y., Chang, L., Viola, K. L., Lacor, P. N., Lambert, M. P., Finch, C. E., Krafft, G. A., and Klein, W. L. (2003) Alzheimer's disease-affected brain: presence of oligomeric Aβ ligands (ADDLs) suggests a molecular basis for reversible memory loss, *Proc. Natl Acad. Sci. USA 100*, 10417–10422.

35. Shirahama, T., and Cohen, A. S. (1967) High-resolution electron microscopic analysis of the amyloid fibril, *J. Cell Biol. 33*, 679–708.

36. Kirschner, D. A., Inouye, H., Duffy, L. K., Sinclair, A., Lind, M., and Selkoe, D. J. (1987) Synthetic peptide homologous to β-protein from Alzheimer's disease forms amyloid like fibrils in vitro, *Proc. Natl. Acad. Sci. USA 84*, 6953–6957.

37. Serpell, L. C., and Smith, J. M. (2000) Direct visualization of the β-sheet structure of synthetic Alzheimer's amyloid, *J. Mol. Biol. 299*, 225–231.

38. Sunde, M., Serpell, L. C., Bartlam, M., Fraser, P. E., Pepys, M. B., and Blake, C. C. F. (1997) The common core structure of amyloid fibrils by synchrotron X-ray diffraction, *J. Mol. Biol. 273*, 729–739.

39. Luhrs, T., Ritter, C., Adrian, M., Riek-Loher, D., Bohrmann, B., Dobeli, H., Schubert, D., and Riek, R. (2005) 3D structure of Alzheimer's amyloid-beta(1-42) fibrils, *Proc. Natl. Acad. Sci. USA 102*, 17342-17347.

40. Jaroniec, C. P., MacPhee, C. E., Bajaj, V. S., McMahon, M. T., Dobson, C. M., and Griffin, R. G. (2004) High resolution molecular structure of a peptide in an amyloid fibril determined by magic angle spinning NMR spectroscopy, *Proc. Natl. Acad. Sci. USA 101*, 711–716.

41. Tycko, R. (2004) Progress towards a molecular-level structural understanding of amyloid fibrils, *Curr. Opin. Struct. Biol. 14*, 96–103.

42. Chiti, F., Webster, P., Taddei, N., Clark, A., Stefani, M., Ramponi, G., and Dobson, C. M. (1999) Designing conditions for in vitro formation of amyloid protofilaments and fibrils, *Proc. Natl. Acad. Sci. USA 96*, 3590-3594.

43. MacPhee, C. E., and Dobson, C. M. (2000) Formation of Mixed Fibrils Demonstrates the Generic Nature and Potential Utility of Amyloid Nanostructures, *J. Am. Chem. Soc. 122*, 12707-12713.

44. Hardy, J., and Allsop, D. (1991) Amyloid deposition as the central event in the aetiology of Alzheimer's disease, *Trends Pharmacol. Sci. 12*, 383–88.

45. Mudher, A., and Lovestone, S. (2002) Alzheimer's disease - do tauists and baptists finally shake hands?, *Trends Neurosci. 25*, 22–26.

46. Lesne, S., Koh, M. T., Kotilinek, L., Kayed, R., Glabe, C. G., Yang, A., Gallagher, M., and Ashe, K. H. (2006) A specific amyloid-beta protein assembly in the brain impairs memory, *Nature 440*, 352-357.

47. Townsend, M., Shankar, G. M., Mehta, T., Walsh, D. M., and Selkoe, D. J. (2006) Effects of secreted oligomers of amyloid beta-protein on hippocampal synaptic plasticity: a potent role for trimers, *J. Physiol. 572*, 477-492.

48. Haass, C., and Selkoe, D. J. (2007) Soluble protein oligomers in neurodegeneration: lessons from the Alzheimer's amyloid beta-peptide, *Nature reviews 8*, 101-112.

49. Klein, W. L., Krafft, G. A., and Finch, C. E. (2001) Targeting small Abeta oligomers: the solution to an Alzheimer's disease conundrum?, *Trends Neurosci. 24*, 219-224.

50. Mucke, L., Masliah, E., Yu, G. Q., Mallory, M., Rockenstein, E. M., Tatsuno, G., Hu, K., Kholodenko, D., Johnson-Wood, K., and McConlogue, L. (2000) High-level neuronal expression of abeta 1-42 in wild-type human amyloid protein precursor transgenic mice: synaptotoxicity without plaque formation, *J. Neurosci. 20*, 4050-4058.

51. Demuro, A., Mina, E., Kayed, R., Milton, S. C., Parker, I., and Glabe, C. G. (2005) Calcium dysregulation and membrane disruption as a ubiquitous neurotoxic mechanism of soluble amyloid oligomers, *J. Biol. Chem. 280*, 17294-17300.

52. Kourie, J. I., Culverson, A. L., Farrelly, P. V., Henry, C. L., and Laohachai, K. N. (2002) Heterogeneous amyloid-formed ion channels as a common cytotoxic mechanism: implications for therapeutic strategies against amyloidosis, *Cell Biochem. Biophys. 36*, 191-207.

53. Kayed, R., Sokolov, Y., Edmonds, B., McIntire, T. M., Milton, S. C., Hall, J. E., and Glabe, C. G. (2004) Permeabilization of lipid bilayers is a common conformation-dependent activity of soluble amyloid oligomers in protein misfolding diseases, *J. Biol. Chem. 279*, 46363-46366.

54. Fagan, T., Kagan, B., Corbin, D., Hwang, W., Glabe, C., Nault, L., Lal, R., Teplow, D., Albensi, B., and Sokolov, Y. (2006) Alzheimer Research Forum Live Discussion: Now you see them, now you don't: The amyloid channel hypothesis, *J. Alzheimers Dis. 9*, 219-224.

55. Lashuel, H. A., and Lansbury, P. T., Jr. (2006) Are amyloid diseases caused by protein aggregates that mimic bacterial pore-forming toxins?, *Q. Rev. Biophys. 39*, 167-201.

56. Lin, H., Bhatia, R., and Lal, R. (2001) Amyloid beta protein forms ion channels: implications for Alzheimer's disease pathophysiology, *FASEB J. 15*, 2433-2444.

57. Simakova, O., and Arispe, N. J. (2006) Early and late cytotoxic effects of external application of the Alzheimer's Abeta result from the initial formation and function of Abeta ion channels, *Biochemistry 45*, 5907-5915.

58. Dong, Z., Saikumar, P., Weinberg, J. M., and Venkatachalam, M. A. (2006) Calcium in cell injury and death, *Annu. Rev. Pathol. 1*, 405-434.

59. Kawahara, M., Kuroda, Y., Arispe, N., and Rojas, E. (2000) Alzheimer's beta-amyloid, human islet amylin, and prion protein fragment evoke intracellular free calcium elevations by a common mechanism in a hypothalamic GnRH neuronal cell line, *J. Biol. Chem. 275*, 14077-14083.

60. Arispe, N., Rojas, E., and Pollard, H. B. (1993) Alzheimer disease amyloid beta protein forms calcium channels in bilayer membranes: blockade by tromethamine and aluminum, *Proc. Natl. Acad. Sci. USA 90*, 567-571.

61. Arispe, N., Pollard, H. B., and Rojas, E. (1993) Giant multilevel cation channels formed by Alzheimer disease amyloid beta-protein [A beta P-(1-40)] in bilayer membranes, *Proc. Natl. Acad. Sci. USA 90*, 10573-10577.

62. Arispe, N., Pollard, H. B., and Rojas, E. (1996) Zn2+ interaction with Alzheimer amyloid beta protein calcium channels, *Proc. Natl. Acad. Sci. USA 93*, 1710-1715.

63. Quist, A., Doudevski, I., Lin, H., Azimova, R., Ng, D., Frangione, B., Kagan, B., Ghiso, J., and Lal, R. (2005) Amyloid ion channels: a common structural link for protein-misfolding disease, *Proc. Natl. Acad. Sci. USA 102*, 10427-10432.

CHAPTER II

Methodology Development of Single Molecule Photobleaching

2.1 Introduction

It has been discussed in Chapter I that the study of β-amyloid peptides and their early oligomer formation is very challenging for traditional techniques, because these peptides exist at extremely low physiological concentrations, and β-amyloid oligomers are very heterogeneous and dynamic. Due to these challenges, single molecule techniques appear to be very promising for studying the oligomerization of β-amyloid peptides.

Thanks to the advances of modern microscopy, individual molecules have been successfully detected and studied in the past two decades. In particular, single molecule fluorescence measurements have undergone an explosive growth in the past twenty years, with the number of publications increasing exponentially (1). The ability to conduct experiments at the single molecule level has opened up the possibility for more detailed studies of many biological processes at the molecular level (2-6).

In this chapter, a single molecule methodology based on photobleaching phenomenon is developed for the quantitative determination of the sizes of β-amyloid oligomers. Compared to the bulk/ensemble measurements, single molecule studies have the following unique advantages:

1. A typical single molecule experiment requires a sample concentration of nanomolar or even lower to maintain a good spatial separation between the individual molecules. This low sample concentration requirement is very beneficial for our research since β-amyloid peptides can be studied at their natural physiological concentration.
2. Because the oligomers are studied at an individual level, the heterogeneity of the oligomeric species can be directly observed. Thus single molecule measurements are not obscured by the "ensemble averaging". The construction of a size histogram based on a large quantity of measured individual oligomers can show the heterogeneity of the oligomeric species.
3. The immobilization techniques used in single molecule measurements allow the studies of the dynamics of a single β-amyloid oligomer. When the oligomers are quickly immobilized, a 'snapshot' of the oligomeric distribution is formed. Thus the dynamic properties of β-amyloid oligomers can be studied in a sequence of snapshots.

2.2 Review of single molecule measurements

2.2.1 A brief history

The first detection of single molecules dated back to 1989 when a single dopant molecule in a host crystal was spectrally isolated and detected at liquid-helium temperatures (7). Since then, as technology kept advancing, single molecule measurements have undergone a tremendous growth. It did not take long before the first spatially isolated single molecules were detected at room temperatures (8). Soon after that, the first biological application of single molecule techniques was successfully demonstrated, in which individual myosin molecules in aqueous solution were imaged with TIRF (Total Internal Reflection Fluorescence) microscopy (9). This opened up the possibilities for studying biological problems at a more fundamental level, and inspired numerous biological applications of single molecule measurements. In fact, since then, biological researches have completely dominated the single molecule field.

2.2.2 The major technical obstacle of single molecule measurements

The major technical obstacle for single molecule detection is the low signal-to-noise ratio (SNR). Therefore, the development of single molecule techniques in the past two decades was essentially all about improving the signal-to-noise ratio. Better fluorophores, which are brighter and can last longer, have been designed and synthesized to improve the signal levels. On the other hand, signal-to-noise ratio improvement through lowering the noise has also been achieved via the use of modern microscopy techniques. Theses microscopy techniques constrain the illumination volume so that the background noise can be effectively reduced. The advancements in photon-detection apparatus have also been crucial in the development of single molecule detection. Much better photon detectors with superb quantum efficiency and low noise have been manufactured and applied to various single molecule studies. In addition, the developments of high numerical aperture (NA) objectives and laser technologies have also contributed in the advancement of single molecule techniques.

2.2.3 Single molecule microscopy

The following modern microscopy is usually used for the detection of single molecules fluorescence: Confocal Scanning Microscopy (10-14), Near-field Scanning Optical Microscopy (NSOM) (15, 16), and Total Internal Reflection Fluorescence (TIRF) Microscopy (9, 17-20).

In a confocal scanning microscope, a laser beam is focused by an objective into a diffraction limited focal volume within the fluorescent specimen. The emitted fluorescent from the illuminated spot is collected by the same objective (in an inverted microscope), and then is passed through a spatial pinhole before finally reaching a photon detector (10, 11). The spatial pinhole serves to eliminate/block any out-of-focus emission. With the use of the pinhole, combined with the tight illumination, the background noise from a confocal setup can be minimized, thus a high signal-to-noise ratio is achieved. However, due to its point-illumination and point-detection geometry, a scanning mechanism is required for the 2D/3D image generation.

Near-field Scanning Optical Microscopy (NSOM) uses a similar point-illumination and point-detection geometry, and requires a scanning mechanism as well. But by exploiting the near-field properties, it can break the far-field diffraction limit, giving a spatial resolution of less than 50nm (16). This ultra-resolution is usually achieved through the use a sharp probing tip, which confines the illumination volume to be much smaller than that of a far-field diffraction limit.

In Total Internal Reflection (TIR) Microscopy, the high signal-to-noise ratio is achieved by evanescent wave illumination. When the incident laser beam is totally reflected at the glass-water/air interface, an exponentially decaying electromagnetic field is generated. This generated field, also called evanescent wave, can penetrate across the media boundary into the water/air to a depth of less than 150 nm. Due to this very thin illumination, the background noise from the sample is again minimized, leading to a high signal-to-noise ratio.

In addition to the optical detection of single molecules, force detection and mechanical manipulation have been successfully applied to single molecules as well (21, 22). Single molecule force spectroscopy typically involves Optical Tweezers (23, 24), Magnetic Tweezers (25), and Atomic Force Microscopy (AFM) (26-28). In these experiments, the mechanical properties of the individual molecules are studied.

2.3 Single Molecule Photobleaching

In this chapter, a relatively new methodology of single molecule measurements, based on the photobleaching of individual fluorophores, is developed for our β-amyloid oligomer studies.

Photobleaching is a well known phenomenon in which the fluorescence of a fluorophore disappears permanently even though the excitation field remains on. The fluorophore undergoes an irreversible photochemical destruction after it cycles through the ground-excitation transitions for a certain number of times (typically 10^5-10^6 for organic dye molecules). The exact mechanism of photobleaching can vary, but it is generally assumed to proceed through the excited singlet state to the excited triplet state. Since the excited triplet state lasts much longer, and is chemically much more reactive, the fluorophore has much higher possibilities to be photo-oxidized by the diffusing oxygen molecules.

This quantized, stochastic photobleaching behavior of a fluorophore is a very good measure of the sizes of β-amyloid oligomers. Since the oligomers are self-assembled from 100% single-fluorophore-labeled β-amyloid peptides, a continuous excitation of the fluorophores in an individual oligomer will generate the number of photobleaching events that equals the number of the subunits in the oligomer (Figure 2.1). Thus by counting the number of photobleaching steps in the observed fluorescence trajectory, a direct measure of the oligomer size can be achieved. During our development of this photobleaching methodology, a few other research groups have been applying the same “photobleaching and counting” idea to their research as well (29-31).

In practice, the fluorophore labeled β-amyloid oligomers are quickly deposited onto a clean glass surface by spin coating. And then the single molecule photobleaching trajectories are recorded. The duration and intensity of the fluorescence signal in the photobleaching trajectory is controlled by the laser power, the absorption cross-section of the fluorophore (a term that includes its orientation relative to the light’s electric field), the fluorescence quantum yield, and the photo-oxidation rate. For an accurate determination of the oligomer sizes, the recorded photobleaching trajectories are subject to some careful analysis and a stochastic simulation. Based on a dipole orientation model, this stochastic simulation provides a better understanding of the observed oligomer photobleaching behaviors.

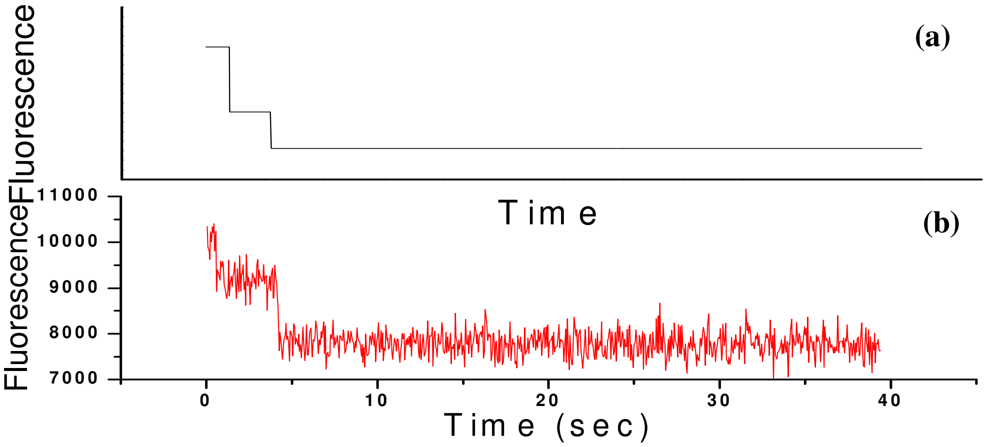

Figure 2.1: Single molecule photobleaching. (a) The concept of "photobleaching and counting". (b) A real photobleaching trajectory of a β-amyloid dimer.

2.4 Microscope instrumentation

Two different microscopes are used for our single molecule photobleaching experiments, a Confocal Scanning Microscope, as illustrated in Figure 2.2, and a Total Internal Reflection Fluorescence (TIRF) Microscope, as illustrated in Figure 2.3.

2.4.1 Confocal Scanning Microscope

The main components of the Confocal Scanning Microscope include:

1. Laser source: A line-tunable, air cooled argon ion laser (532RAP- AO1, Melles-Griot, Carlsbad, CA) is used. The operating wavelength of the laser is at 457.9nm. The vertically polarized light becomes circularly polarized after the laser beam is passed through a circular polarizer.
2. Excitation filter: An excitation filter (D457/l0x, Chroma, Brattleboro, VT) is used to block the plasma discharge of the laser.
3. Dichroic mirror: A two inch dichroic mirror (470/DCLP, Chroma, Brattleboro, VT) is used to reflect the laser beam into the objective for fluorophore excitation, while letting the fluorescence emission pass through for detection.
4. Microscope objective: A high performance objective (PLAP060XOITIRFM-SP, Olympus, Center Valley, PA) is used in our confocal scanning microscope for both focusing excitation light and collecting emission fluorescence. This infinity-corrected oil-immersion objective has a high NA (Numerical Aperture) of 1.45, a magnification of 60, and a working distance of 0.17 mm. It also has the highest level of axial chromatic aberration correction and flat-field correction. The matching immersion oil (Type FF, Cargille Laboratory, Cedar Grove, NJ) for the objective has a refractive index of 1.479. Therefore, standard coverglasses (12-545-102, 0.13-0.17mm, Fisher Scientific, Pittsburgh, PA) should be used with this objective. Since the objective is infinity-corrected, a matching tube lens (shown in Fig. 2.2, 180mm) purchased from Olympus as well is required in our system to focus the fluorescence signal to the intermediate image plane for detection.
5. Scanning stage: The scanning stage used in our system is the XYZ piezo flexure nanopositioner (P-5l7.3CL, Polytech PI, Germany). It comes with a high speed

digital piezoelectric controller (E-71 O.4CL, Polytech PI, Germany). This scanning apparatus can deliver sub-nanometer precision movements within a limited travel range of 100x100x20 μm in the XYZ axes, respectively.

6. Exit pinhole: An exit pinhole placed at the intermediate image plane in a confocal microscope can block out-of-focus light in the emission while let in-focus light pass through. By doing this, both signal-to-noise ratio and spatial resolution can be improved. Although the calculation of the pinhole size requires some elaborate considerations (32), it can be approximated as the product of the objective magnification and the size of the diffraction-limited focus at the sample plane. In practice, a pinhole is not required in our system, because the small active area (180μm in diameter) of the photon detector (avalanche photodiode) effectively acts as a light-restricting aperture.
7. Emission filter: Both an edge filter (LP02-458RU-25, Semrock, Rochester, NY) and a band-pass emission filter (D520/60M, Chroma, Brattleboro, VT) are used in our system for fluorescence detection. The edge filter has an OD (optical density) of larger than 6 at the laser wavelength so it is mainly used for blocking the scattered laser light. The band-pass emission filter sets the spectral window for fluorescence detection, thus the selection of an appropriate emission filter is extremely important for single molecule detection.
8. Photon detector: A single-photon-counting (Geiger mode) avalanche photodiode (SPCM-AQ 161, PerkinElmer Optoelectronics, Canada) is used as the photon detector in our system. The quantum efficiency of this unit at the fluorescence

emission wavelength (~520nm) is 50%. It has an extremely low dark current of 50 counts per second.

9. Data acquisition: The output signal of the APD (TTL pulses) is sent to a Counter/Timer card (PCI-6602, National Instruments, Austin, TX) in the computer. The acquisition software is written in LabVIEW (National Instruments, Austin, TX).

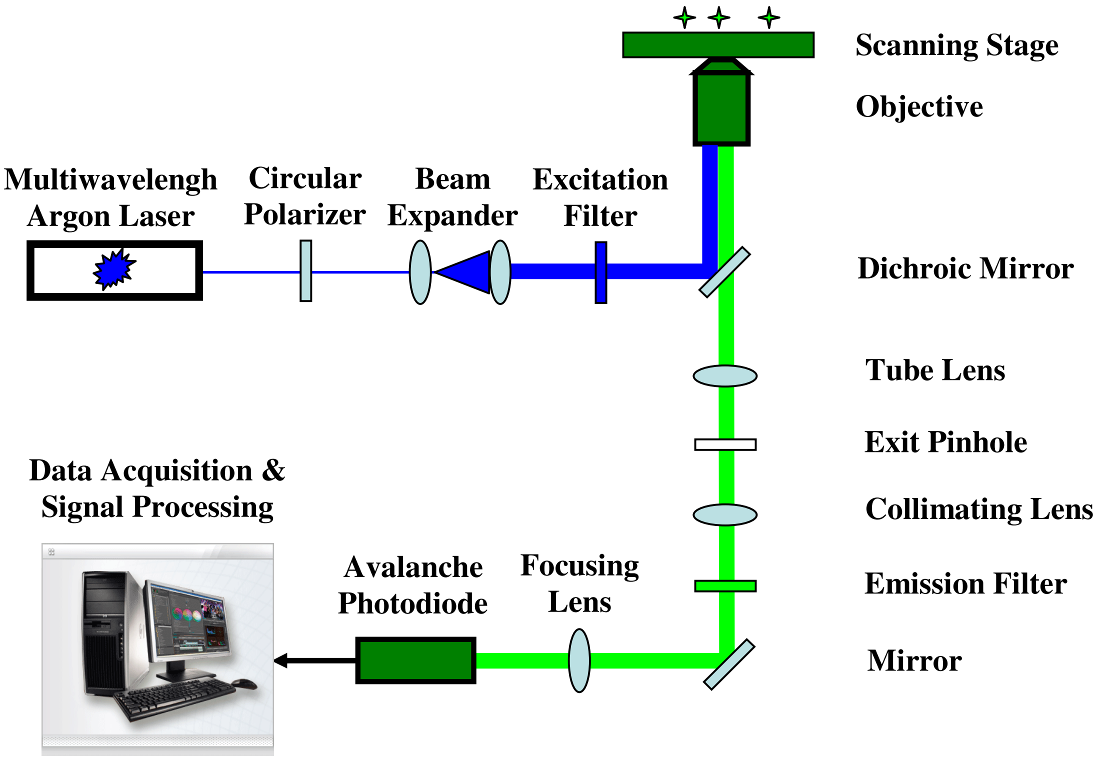

Figure 2.2: Block diagram of a Confocal Scanning Microscope

When the confocal scanning microscope is used for single molecule photobleaching experiments, the β-amyloid oligomer coated coverglass surface is raster scanned. Therefore, a threshold needs to be pre-set such that, when the detected fluorescence signal is higher than this threshold, the scanning can be paused and the recording of a photobleaching trajectory can be triggered. However, due to this pre-set threshold, missing of oligomers with low fluorescence emission can occur during the scanning. Thus the collected data are subject to some careful corrections, which will be discussed in Chapter III.

2.4.2 Total Internal Reflection Fluorescence Microscope

The Total Internal Reflection Fluorescence (TIRF) Microscope in our lab uses a very similar platform (block diagram shown in Figure 2.3) to that of the confocal scanning microscope. The major differences are listed below:

1. Laser source: The total internal reflection microscope is equipped with a more powerful, water cooled argon ion laser (I-90, Coherent, Santa Clara, CA).
2. TIR illumination: An additional focusing lens, which sits on a translational stage in front of the dichroic mirror, is used to focus the collimated laser beam to an off-axis position in the back focal plane of the objective. After re-collimation by the objective, a very narrow (~120μm in diameter) and tilted beam is generated for the sample illumination. With the lateral movement of the focusing lens, the angel of the tilted illumination beam can be changed such that, once it is larger than the critical angel, total internal reflection will occur.
3. No scanning stage and exit pinhole: TIR illumination covers a much larger area than the point-illumination in a confocal scanning microscope. Therefore, a scanning stage is not needed. Due to a 2D image being formed at the intermediate image plane in TIRF microscopy, an exit pinhole should not be used either.

4. Image recorder: A back-illuminated (back-thinned) Electron-Multiplying Charge Coupled Device (EMCCD camera, iXon DV887ACS-BV, Andor Technology, Allentown, NJ) is used as the image recorder in our system. The quantum efficiency of this camera at the fluorescence emission wavelength (~520nm) is 90%. The camera is usually deeply cooled to -75 °C for both reducing the thermal noise and increasing the on-chip gain. Though the typical read-out noise of the unit is ~50 photoelectrons, it can be completely neglected with an appropriate setting of the on-chip gain, thus a high sensitivity is achieved (see Appendix A).

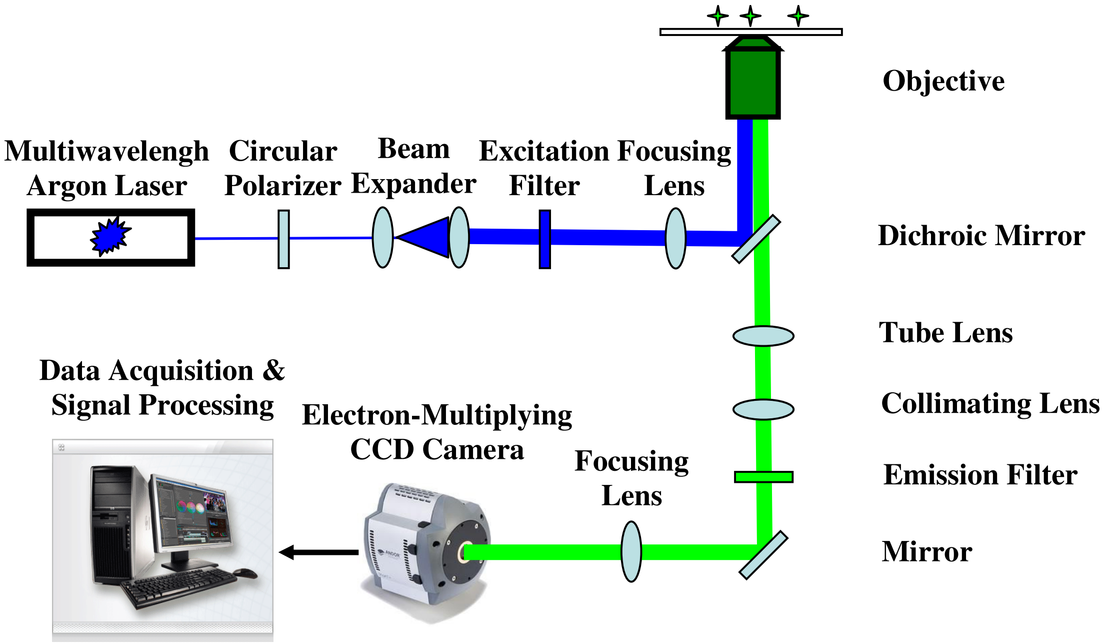

Figure 2.3: Block diagram of a Total Internal Reflection Fluorescence Microscope

With TIRF microscopy, a movie (stack of images) of the immobilized β-amyloid oligomers being photobleaching is recorded. Hence, some image processing is required to identify and locate the individual oligomers (see Appendix B) before the photobleaching trajectories can be extracted from the video.

2.4.3 Confocal Scanning *vs.* TIRF Microscopy

Compared to TIRF microscopy, confocal scanning microscopy has better signal-to-noise ratio and spatial resolution because of the confocal geometry, in which an exit pinhole is used to block much of the out-of-focus light. However, due to the raster scanning mechanism used in confocal scanning microscopy, the data collection efficiency is extremely low.

Although TIRF microscopy has slightly lower signal-to-noise ratio and poorer spatial resolution than confocal scanning microscopy does, it has extremely high data collection efficiency due to the parallel (array) recording mechanism of cameras. With the camera technologies (for both CCD and CMOS cameras) and the computer technologies (for data storage and processing) rapidly advancing, real-time or even high-speed imaging in biological applications has been gaining much popularity.

2.5 Trajectory analysis

The counting of the number of photobleaching steps in a trajectory gives a direct measure of the size of that particular oligomer. Therefore, an accurate identification of the photobleaching steps is very crucial. In general, the determination of photobleaching steps in the recorded trajectories employs an analysis that includes both visual inspection and more careful signal processing.

As a common feature observed in all the photobleaching trajectories, the photobleaching steps from bright fluorophores are typically much larger and quicker than those from dimmer ones. Based on this observation, our data are analyzed in the following way: For the “large digital jump” type photobleaching events, which usually correspond to bright fluorophores, visual inspection is adequate for counting the number of photobleaching steps. In contrast, for the photobleaching trajectories where only a small fluorescence change occurs (Figure 2.4 (a)), some careful analysis involving both noise filtering and photon counting histogramming is required for an accurate determination of the photobleaching steps. It can be shown that this analysis provides an improved differentiation of two rather close fluorescence intensity levels.

2.5.1 Noise filtering

The idea of applying a noise filtering technique to the photobleaching trajectories is to remove some of the noise component so that the small photobleaching steps can be more visible. However, the challenge lies in that both the noise and the photobleaching steps contain high frequency components. Therefore, low-pass digital filters, which are commonly used for removing high frequency noises, will cause severe edge blurring in the photobleaching steps.

While most of the commonly used filters fail to work, one particular digital filtering technique, named the forward-backward non-linear digital filter, seems to be very suitable for our trajectory analysis. It was initially developed for extracting small signals from ion channel recordings (33), and was later introduced to the single molecule fluorescence field (34). Based on a simple running-average algorithm, this digital filtering technique can adjust the size of the averaging-windows such that, when a sudden change occurs in the signal, the filter shrinks its averaging-window significantly to preserve the fast transients. Therefore, it has the unique feature of preserving sudden changes in the signal with minimum edge blurring, making it very suitable for our photobleaching trajectory analysis (Figure 2.4 (b)). It should be noted that the parameters of this digital filter need to be carefully chosen to avoid signal distortions.

2.5.2 Photon counting histogramming

Photon counting histogramming is the other technique we use in our trajectory analysis. It has been widely used in Fluorescence Correlation Spectroscopy to differentiate multiple fluorescence intensity levels (35, 36). This technique has also been used in photobleaching experiments (29-31). The number of photons detected per unit time from fluorophores (at excitation levels below the saturation intensity) follows a Poisson distribution. The construction of a photon counting histogram can help reveal multiple fluorescence intensities by showing the corresponding Poisson distribution for each intensity level. As indicated in Figure 2.4 (c), the photon counting histogram of the raw trajectory is well fit with two Gaussian distributions, indicating there are two close fluorescence intensity levels.

It can be shown that the combination of the noise filtering technique and the photon counting histogram allows for improved resolution of different fluorescence intensities. After the implementation of the forward-backward non-linear filter to the raw trajectory, the two very close fluorescence intensities are clearly separated on the photon counting histogram (Figure 2.4(d)).

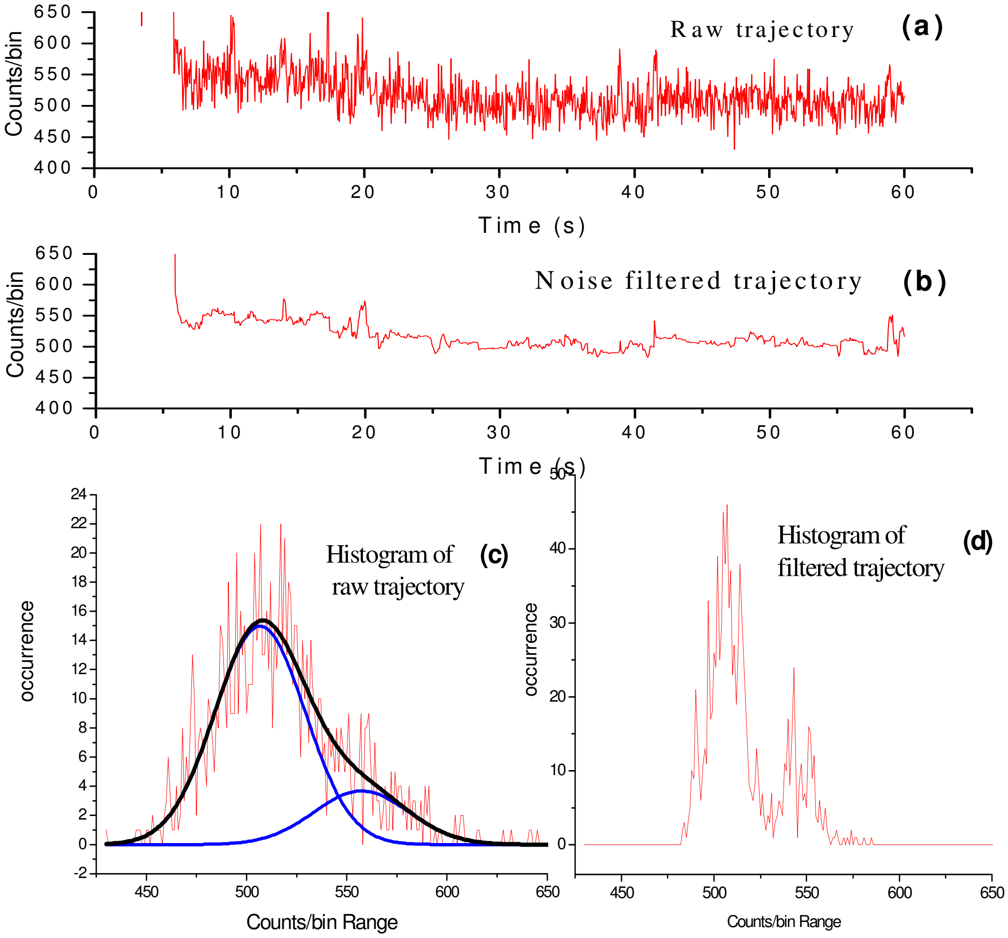

Figure 2.4: Noise filtering and photon counting histogramming in trajectory analysis (a) A photobleaching trajectory showing two close fluorescence intensity levels; (b) The same trajectory after being filtered by the forward-backward non-linear filter; (c) The photon counting histogram of the raw trajectory. The solid curves show that this histogram is well fitted with two Gaussian distributions (with widths being equal to the square root of their means). (d) The photon counting histogram of the filtered trajectory. The two fluorescence levels have now been clearly separated after the noise reduction.

These close fluorescence intensity levels, resolved by noise reduction and photon counting histogram, usually correspond to dim fluorophores. Thanks to the typically long duration of these weak fluorescence signals, an adequate number of photons could still be collected to allow us to resolve these dim fluorophore photobleaching events.

2.6 Stochastic simulations of single molecule photobleaching

Further inspection of the analyzed photobleaching trajectories indicates that they could be characterized by two features:

1. The photobleaching steps in fluorescence intensity in a given oligomer are not equal.
2. The trajectories often have a large and fast initial fluorescence drop, which is often followed by a long and low fluorescence tail before photobleaching (see Figure 2.6 (a) and (b) for examples).

In order to gain a better understanding of these photobleaching behaviors, a simple dipole orientation model was developed. Considering that our sample is spin coated onto a coverglass and that the β-amyloid oligomers are immobilized on the glass surface by non-specific interactions, it is reasonable to assume that the fluorophores, which are attached to the oligomers, do not adopt the same dipole orientation. The fact that the noise in the photobleaching trajectories is nearly shot noise limited indicates these photobleached fluorophores have relatively fixed dipole orientations. The above two considerations suggest that fluorophores with a less favorably oriented transition dipole would be excited less frequently, emit fewer photons per unit time and hence photobleach more slowly (since the excitation rate is lower) (see figure 2.5 for illustration).

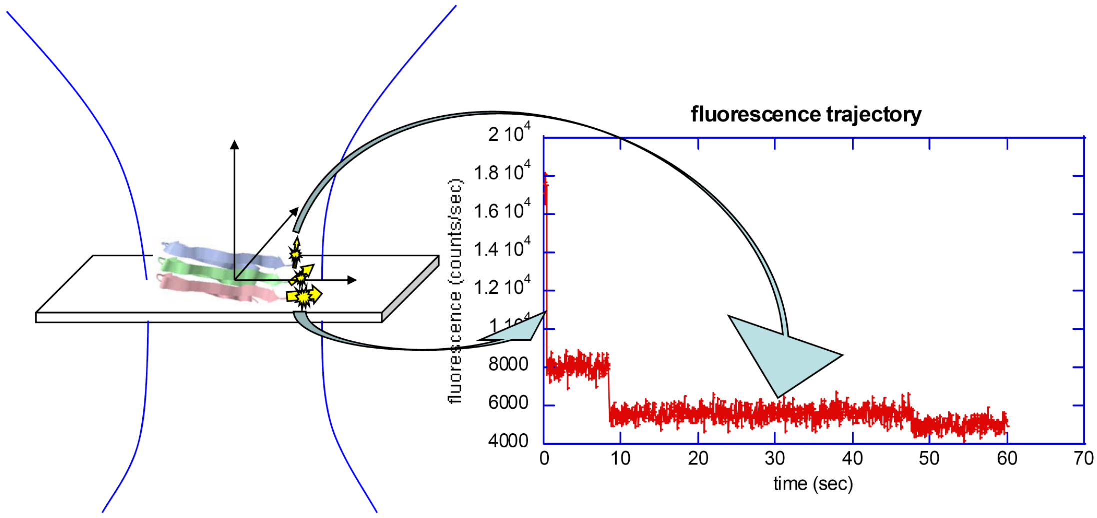

Figure 2.5: Illustration of the dipole orientation model.

To test this hypothesis, we simulate the photobleaching trajectories of individual oligomers assuming that the fluorophores have random, but fixed, dipole orientations and the excitation field is circularly polarized. Based on this model, it is anticipated that with a more parallel orientation of the fluorophore dipole relative to the coverglass surface, the more frequently excited that fluorophore will be, the higher the fluorescence intensity and the shorter the duration of the time to photobleach. (Note: in the plane parallel to the coverglass, the laser is circularly polarized, so there is no dependence of the excitation on the absorption dipole angle projected on to the coverglass plane.)

A program to generate simulated stochastic photobleaching trajectories was written in LabVIEW, and involves the following steps:

1. A random number generator is used to generate an integer (with a preset upper limit) as the number of subunits in the oligomer.
2. A photobleaching time is assigned to each of the fluorophores in the oligomer. These photobleaching times are randomly generated based on the exponential probability distribution $p = (1/\tau)\exp(-t/\tau)$, τ is the preset photobleaching lifetime, reflecting the photostability of the fluorophores that are maximally excited.
3. A position γ relative to the center of the laser beam focus is assigned to the oligomer (we also assume that the intensity of the laser beam falls off as a Gaussian profile $\exp(-\gamma^2/2)$). This oligomer position is generated randomly (with a preset upper limit) based on a uniform probability of the oligomer being deposited on the coverglass.
4. A fixed absorption dipole orientation angle θ (relative to the coverglass surface) is assigned to each of the fluorophores in the oligomer by a random number generator.
5. According to the dipole orientation of each fluorophore and the position of the oligomer, each fluorophore's photobleaching time is adjusted by $\left(\cos^2(\theta)\exp(-\gamma^2/2)\right)^{-1}$, and the fluorescence intensity is adjusted by $\cos^2(\theta)\cos^2(\theta+\vartheta)\exp(-\gamma^2/2)$, in which ϑ is the angle between absorption

dipole and emission dipole. For simplicity and with no impact on the qualitative features of the simulation, we assume $\vartheta = 0$ since, while the relative angle between the absorption and emission dipoles of the fluorophore (HiLyte Fluor^{TM} 488) has not been determined, the strong mirror image relationship between absorption and emission spectra indicates that they reflect the same electronic transition.

6. The fluorescence signals of all the fluorophores within the oligomer are added to yield a single photobleaching trajectory.
7. Poisson noise is added to the trajectory.

Using the stochastic simulation described above and the random dipole orientation model, photobleaching trajectories are produced (see Appendix C for an example). Typical simulation trajectories are shown in Figure 2.6 (c) and (d), and clearly resemble the experimental trajectories in 2.6 (a) and (b), which represent a monomer and a trimer respectively.

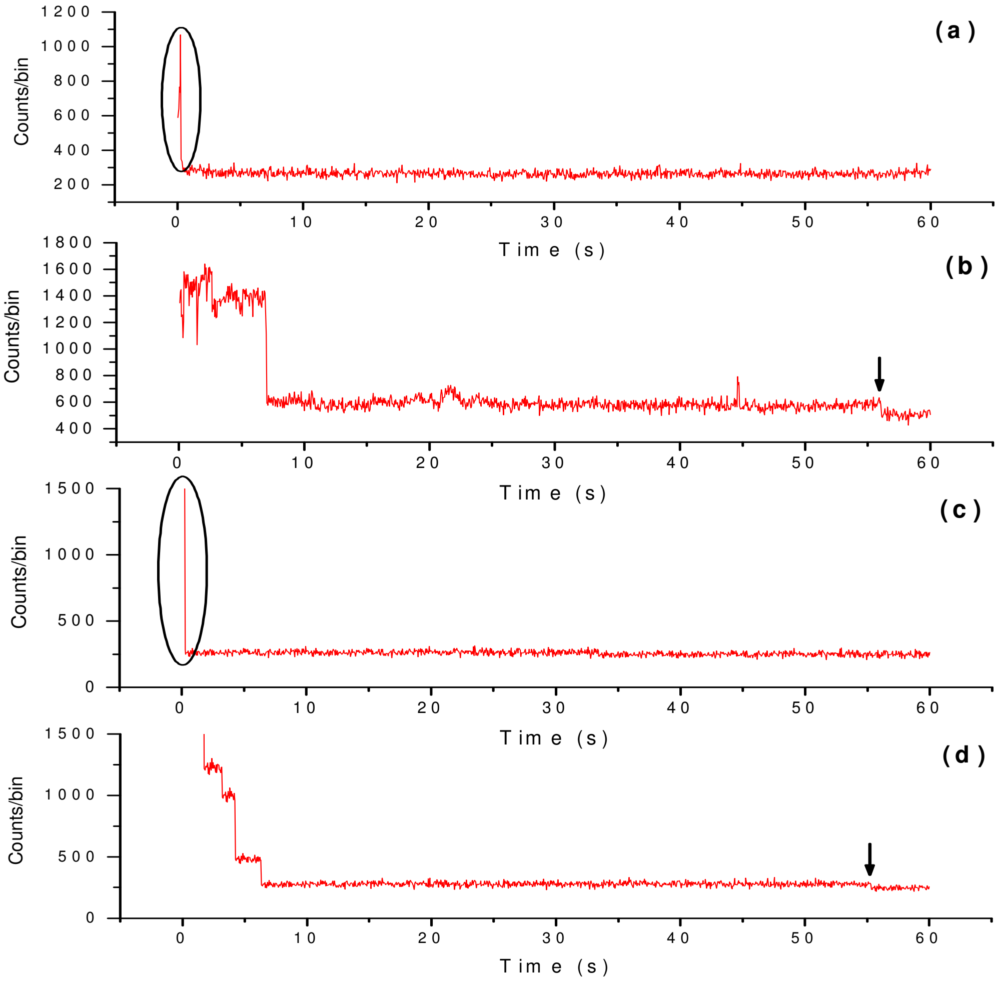

Figure 2.6: Stochastic simulations of single molecule photobleaching, and their comparison with experimental data (a) Experimental photobleaching trajectory with a large & fast initial jump. (b) Experimental photobleaching trajectory with a long & low tail. (c) Simulated photobleaching trajectory with a large & fast initial jump. (d) Simulated photobleaching trajectory with a long & low tail. (Photobleaching events are highlighted by the circles and arrows).

While such a simulation does not prove the proposed model for the origin of the variability in the trajectories, it supports the notion that different dipole orientations are a major contributor to the variations in the photobleaching trajectories. In fact, we have observed the same variability in fluorescence intensities and photobleaching behavior in the fluorophore-only control experiments as that in the fluorophore-labeled β-amyloid experiments.

It will be shown in the next chapter that, besides its likely important contribution to the variation in the photobleaching trajectories, the random dipole orientation model is also critical for an accurate construction of the size distribution of β-amyloid oligomers.

2.7 Summary

In this chapter, the advantages of single molecule studies on β-amyloid oligomers are first discussed. And then following a brief review of the single molecule measurements in general, a new methodology based on single molecule photobleaching is developed, including its concept, instrumentation, and data analysis. Finally a stochastic simulation of single molecule photobleaching is presented. The simulation, which is based on the random dipole orientation model, helps us understand the photobleaching behaviors of the fluorophores.

Reference

1. Joo, C., Balci, H., Ishitsuka, Y., Buranachai, C., and Ha, T. (2008) Advances in Single-Molecule Fluorescence Methods for Molecular Biology, *Annu. Rev. Biochem. 77*, 51-76.

2. Lu, H. P., Xun, L., and Xie, X. L. (1998) Single-Molecule Enzymatic Dynamics, *Science 282*, 1877-1882.

3. Yildiz, A., Forkey J. N., McKinney S. A., Ha, T., Goldman, Y. E., and Selvin, P. R. (2003) Myosin V Walks Hand-Over-Hand: Single Fluorophore Imaging with 1.5-nm Localization, *Science 300*, 2061-2065.

4. Nishizaka T., Oiwa, K., Noji, H., Kimura, S., Muneyuki, E., Yoshida, M. and Kinosita, K. Jr. (2004) Chemomechanical coupling in F1-ATPase revealed by simultaneous observation of nucleotide kinetics and rotation, *Nat. Struct. Mol. Biol. 11*, 142-148.

5. Liu, S., Bokinsky, G., Walter, N. G., and Zhuang, X. (2007) Single-Molecule Chemistry and Biology Special Feature: Dissecting the multistep reaction pathway of an RNA enzyme by single-molecule kinetic “fingerprinting”, *Proc. Natl. Acad. Sci. USA 104*, 12634-12639.

6. Kural, C., Kim, H., Syed, S., Goshima, G., Gelfand, V. I., and Selvin, P. R. (2005) Kinesin and Dynein Move a Peroxisome in Vivo: A Tug-of-War or coordinated Movement?, *Science 308*, 1469-1472.

7. Moerner, W. E., and Kador, L. (1989) Optical Detection and Spectroscopy of Single Molecules in a Solid, *Phys. Rev. Lett. 62*, 2535-2538.

8. Betzig, E., and Chichester, R. J. (1993) Single Molecules Observed by Near-Field Scanning Optical Microscopy, *Science 262*, 1422-1425.

9. Funatsu, T., Harada, Y., Tokunaga, M., Salto, K., and Yanagida, T. (1995) Imaging of single fluorescent molecules and individual ATP turnovers by single myosin molecules in aqueous solution, *Nature 374*, 555-559.

10. Minsky, M. (1961) Microscopy Apparatus, *US Pat*. 3,013,467.

11. Minsky, M. (1988) Memoir on Inventing the Confocal Scanning Microscopy, *Scanning 10*, 128-138.

12. Shi, J., Palfey, B. A., Dertouzos, J., Jensen, K. F., Gafni, A., and Steel, D. G. (2004) Multiple states of the Tyr318Leu mutant of dihydroorotate dehydrogenase revealed by single-molecule kinetics, *J. Am. Chem. Soc. 126*, 6914-6922.

13. Shi, J., Dertouzos, J., Gafni, A., Steel, D. G., and Palfey, B. A. (2006) Single-molecule kinetics reveals signatures of half-sites reactivity in dihydroorotate dehydrogenase A catalysis, *Proc. Natl. Acad. Sci. USA 103*, 5775-5780.

14. Brender, J. R., Dertouzos, J., Ballou, D. P., Massey, V., Palfey, B. A., Entsch, B., Steel, D. G., and Gafni, A. (2005) Conformational dynamics of the isoalloxazine in substrate-free p-hydroxybenzoate hydroxylase: Single-molecule studies, *J. Am. Chem. Soc. 127*, 18171-18178.

15. Hecht, B., Sick, B., Wild, U. P., Deckert, V., Zenobi, R., Martin, O. J. F., and Dieter, D.W. (2000) Scanning near-field optical microscopy with aperture probes: Fundamentals and applications, *J. Chem. Phys. 18*, 7761-7774.

16. Oshikane, Y., Kataoka, T., Okuda, M., Hara, S., Inoue, H., and Nakano, M. (2007) Observation of nanostructure by scanning near-field optical microscope with small sphere probe, *Sci. Technol. Adv. Mater. 8*, 181–185.

17. Axelrod, D., Thompson, N. L., and Burghardt, T. P. (1983) Total Internal-Reflection Fluorescence Microscopy, *J. Microsc. (Oxf) 129*, 19-28.

18. Axelrod, D. (2001) Total internal reflection fluorescence microscopy in cell biology, *Traffic 2*, 764-774.

19. Tokunaga, M., Kitamura, K., Saito, K., Iwane, A. H., and Yanagida, T. (1997) Single molecule imaging of fluorophores and enzymatic reactions achieved by objective-type total internal reflection fluorescence microscopy, *Biochem. Biophys. Res. Commun. 235*, 47-53.

20. Iino, R., Koyama, I., and Kusumi, A. (2001) Single molecule imaging of green fluorescent proteins in living cells: E-cadherin forms oligomers on the free cell surface, *Biophys. J. 80*, 2667-2677.

21. Clausen-Schaumann, H., Seitz, M., Krautbauer, R., and Gaub, H. E. (2000) Force spectroscopy with single bio-molecules, *Curr. Opin. Chem. Biol. 4*, 534-530.

22. Janshoff, A., Neitzert, M., Oberdorfer, Y., and Fuchs, H. (2000) Force spectroscopy of molecular systems - Single molecule spectroscopy of polymers and biomolecules, *Angew. Chem. Int. Ed. 39*, 3213-3237.

23. Mehta, A. D., Rief, M., Spudich, J. A., Smith, D. A., and Simmons, R. M. (1999) Single-molecule biomechanics with optical methods, *Science 283*, 1689-1695.

24. Bustamante, C., Bryant, Z., and Smith, S. B. (2003) Ten years of tension: single-molecule DNA mechanics, *Nature 421*, 423-427.

25. Gosse, C., and Croquette, V. (2002) Magnetic tweezers: Micromanipulation and

force measurement at the molecular level, *Biophys. J. 82*, 3314-3329.

26. Rief, M., Gautel, M., Oesterhelt, F., Fernandez, J. M., and Gaub, H. E. (1997) Reversible unfolding of individual titin immunoglobulin domains by AFM, *Science 276*, 1109-1112.

27. Engel, A., and Muller, D. J. (2000) Observing single biomolecules at work with the atomic force microscope, *Nat. Struct. Biol. 7*, 715-718.

28. Fisher, T. E., Marszalek, P. E., and Fernandez, J. M. (2000) Stretching single molecules into novel conformations using the atomic force microscope, *Nat. Struct. Biol. 7*, 719-724.

29. Shu, D., Zhang, H., Jin, J., and Guo, P. (2007) Counting of six pRNAs of phi29 DNA-packaging motor with customized single-molecule dual-view system, *EMBO J. 26*, 527-537.

30. Ulbrich, M.H., and Isacoff, E.Y. (2007), Subunit counting in membrane-bound proteins, *Nat. Methods 4*, 319-321.

31. Ji, W., Xu, P., Li, Z., Lu, J., Liu, L., Zhan, Y., Chen, Y., Hille, B., Xu, T., and Chen, L. (2008) Functional stoichiometry of the unitary calcium-release-activated calcium channel, *Proc. Natl. Acad. Sci. USA 105*, 13668-13673.

32. Sandison, D. R., Williams, R. M., Wells, K. S., Strickler, J. and Webb, W. W. (1995) Quantitative fluorescence confocal laser scanning microscopy, *The Handbook of Biological Confocal Microscopy*, Plenum Press, New York, 39-53.

33. Chung, S. H., and Kennedy, R. A. (1991) Forward-backward non-linear filtering technique for extracting small biological signals from noise, *J. Neurosci. Meth. 40*, 71-86.

34. Haran, G (2004) Noise reduction in single-molecule fluorescence trajectories of folding proteins, *Chem. phys. 307*, 137-145.

35. Thompson, N. L., Lieto, A. M., and Allen, N. W. (2002) Recent advances in fluorescence correlation spectroscopy. *Curr. Opin. Struct. Biol. 12*, 634-641.

36. Chen, Y., Müller, J. D., Ruan, Q., and Gratton, E. (2002) Molecular Brightness Characterization of EGFP In Vivo by Fluorescence Fluctuation Spectroscopy. *Biophys. J. 82*, 133-144.

CHAPTER III

Quantitative Construction of β-amyloid(1-40) Oliogomer Distribution Based on Single Molecule Photobleaching

3.1 Introduction

It has been shown in Chapter I that β-amyloid peptides can form both oligomers and fibrils, and are associated with the pathology of Alzheimer's disease (AD) (1-6). However, despite the intensive efforts and substantial progress made in β-amyloid studies in recent years, the mechanism by which these peptides gain their neurotoxic function upon oligomerization and aggregation remains unclear. With evidence from recent experiments, it has been suggested that the toxic agents at the origin of Alzheimer's disease are oligomeric forms of β-amyloid peptides (7-9), contrary to the historical view that implicated fibrils. The toxic oligomeric form may consist of only a few monomeric units. Indeed, AFM (Atomic Force Microscopy) and STEM (Scanning Transmission Electron Microscopy) studies have shown that small annular structures, resembling the pores formed by bacterial toxins, are generated by β-amyloid and α-synuclein (10-13).

While the identification of the toxic oligomer species has become one of the important topics in β-amyloid studies, understanding their role in toxicity has been challenging. These β-amyloid oligomers usually occur at an extremely low physiological concentration, often in the range of nano to sub-nano molar. Moreover, they are highly heterogeneous and metastable. In some cases there is evidence that the structures of the small oligomers are in dynamic equilibrium (14, 15). Hence, ensemble studies mask the details of these features.

In Chapter II, we presented a new approach to the study of β-amyloid oligomers and their identification based on single molecule fluorescence spectroscopy. In this chapter we build on this work and use the developed single molecule photobleaching methodology to quantitatively construct the β-amyloid oligomer distribution.

In this work, we focus on the study of β-amyloid(1-40), a 40 amino acid peptide that has been identified as the major component of the extracellular plaques found in Alzheimer patients' brains (16). Due to the high sensitivity of Confocal Scanning Microscopy and Total Internal Reflection Fluorescence (TIRF) Microscopy, single oligomers made of fluorescently labeled β-amyloid(1-40) peptides can be readily identified and differentiated from other oligomers containing a different number of subunits. By counting the number of photobleaching steps, we show we can determine the number of monomers of each detected β-amyloid(1-40) oligomer, allowing us to resolve different equilibrium mixtures of β-amyloid while working at a protein concentration below 1nM. It has been shown that the stochastic simulations, in which β-amyloid oligomers are modeled as structures with random dipole orientations of the fluorophore associated with each monomer, can account for observed variations in photobleaching trajectories. It will be further discussed in this chapter that these simulations are also critical for correcting the bias in constructing β-amyloid(1-40) oligomer distributions, allowing us to improve the quantitative interpretation of the data.

3.2 Methods

3.2.1 β-amyloid(1-40) preparation

The HiLyte Fluor^{TM} 488 β-amyloid(1-40) (AnaSpec, San Jose, CA) was kept frozen at -20°C. For the purpose of consistency, before the use of any samples, the peptide was re-dissolved in TFA (Trifluoroacetic Acid, Sigma-Aldrich, St. Louis, MO) at 1mg/ml first, then bath sonicated for at least 30min to break apart any pre-formed aggregates (17). The solution was then aliquotted into small samples, and finally lyophilized and stored at -20°C. To make a fresh β-amyloid(1-40) sample, the lyophilized powder was directly dissolved into 10mM Sodium Phosphate, 100mM Sodium Chloride, pH7.4 buffer, followed by a 60-second bath sonication.

3.2.2 Gel filtration HPLC

An aliquot of 20μl of 5μM fresh HiLyte Fluor^{TM} 488 β-amyloid(1-40) sample was run through a gel filtration column (TOSOH Bioscience, South San Francisco, CA) at room temperature in 10mM Sodium Phosphate, 100mM Sodium Chloride, pH7.4 buffer with a flow rate of 1ml/min in order to get fractions of different oligomer species. The molecular weight calibration for this column was done by using the following proteins/molecules at exactly the same separation condition: thyroglobulin (669kDa), γ-globulin (165kDa), ovalbumin (43kDa), RNase A (14kDa), ubiquitin (8.6kDa), aprotinin (6.5kDa) and NATA (180Da).

3.2.3 Sample preparation for single molecule photobleaching

For photobleaching experiments of incubated HiLyte Fluor^{TM} 488 β-amyloid(1-40) samples, the dissolved peptides were diluted to 100nM concentration. For the gel filtration chromatography separated HiLyte Fluor^{TM} 488 β-amyloid(1-40) monomer/dimer fraction sample, the peptide was used directly after fractionation. A further dilution of either sample to a final concentration of between 1nM and 0.1nM was applied before the HiLyte Fluor^{TM} 488 β-amyloid(1-40) oligomers were deposited onto a coverglass. Two droplets of this diluted peptide solution were spin coated onto the coverglass at 2000RPM, until the coverglass became dry (approximately 30-40 seconds at room temperature). Coverglasses were pre-cleaned by rinsing with Milli-Q water and then baking in a kiln at ~500°C for two hours.

The low spinning speed in the sample deposition process suggests the β-amyloid(1-40) oligomers are minimally perturbed. In particular, fragmentation of the oligomers upon being immobilized on the glass surface is very unlikely to occur, because the slow spinning of the coverglass at 2000rpm only yields a rate of centrifugation of less than 20xg, while a typical study on subunit stoichiometry of non-covalent protein complexes needs an unltracentrifugation at an acceleration rate of about three orders of magnitude higher than this (18).

3.2.4 Single molecule photobleaching microscopy

When a confocal scanning microscope was used for single molecule photobleaching, the sample coated coverglass was raster-scanned on a piezoelectric stage (Physik Instrumente, Auburn, MA) until a pre-set count rate threshold indicating the presence of a fluorescent oligomer was reached for initiating the recording of a photobleaching trajectory. When a total internal reflection fluorescence microscope was used, the sample was directly imaged by an EMCCD camera (iXon DV887ACS-BV, Andor Technology, Allentown, NJ). The photobleaching trajectories were recorded in time steps of 50ms in both microscopies. The details of the microscopy techniques and instrumentation can be found in Chapter II.

3.2.5 Photobleaching trajectory analysis

An accurate determination of the photobleaching steps in the trajectories is very crucial in this work. In general, the photobleaching trajectory analysis involved both visual inspection and more careful analysis, including noise filtering and photon counting histogramming. The details of trajectory analysis can be found in Chapter II.

3.2.6 Stochastic simulations of single molecule photobleaching

Stochastic simulations of single molecule photobleaching, which are based on the random dipole orientation model, were written in LabVIEW (National Instruments, Austin, TX). These simulations not only helped us understand the photobleaching behaviors of the fluorophores, but also played a critical role in improving the quantitative interpretation of the single molecule data. The details of the stochastic simulations can be found in Chapter II.

3.3 Results and Discussions

3.3.1 Gel filtration HPLC of HiLyte Fluor^{TM} 488 β-amyloid(1-40) oligomers

An aliquot of 20μl of 5μM freshly dissolved HiLyte Fluor^{TM} 488 β-amyloid(1-40) in 10mM Sodium Phosphate, 100mM Sodium Chloride, pH7.4 buffer was run through a gel filtration column and the elution profile is shown in Figure 3.1 (data obtained by Wong, P.). Three elution peaks centered at 11.3, 11.8 and 12.4 min are clearly visible. According to the molecular weight calibration curve for this column, these peaks correspond to molecular weights of about 14.5kDa, 9.6kDa and 5.9kDa respectively. A fourth, minor, peak elutes at 8.3min, corresponding to a molecular weight of about 150kDa, representing a small amount of high oligomeric species. The gel filtration chromatography results clearly show that the β-amyloid(1-40) oligomers in solution are heterogeneous.

While the gel filtration chromatography clearly demonstrates the presence of at least 3 elution peaks, identification of the species involved based on the molecular weight standards is not straightforward for two main reasons:

1. They do not correspond to the molecular weights of any specific oligomers, but rather fall between two oligomers.
2. The elution peaks are broader than those expected for pure single species.

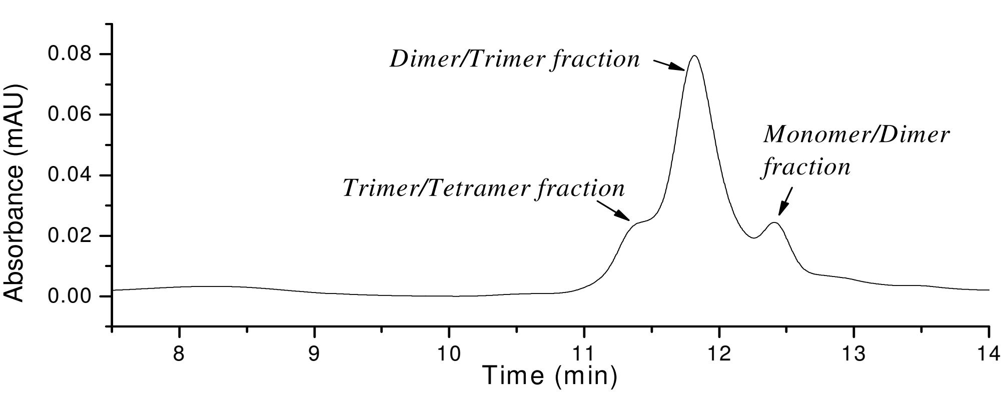

Figure 3.1: HPLC Gel filtration of HiLyte Fluor^{TM} 488 β-amyloid(1-40) oligomers. (data in courtesy of Wong, P.)

We conclude that these peaks are mixtures of two or more oligomeric species as indicated by the peak assignments in the figure. This may be due to interaction between the oligomers and the column material, as suggested by the asymmetric long tail on the elution profile, or due to some structural heterogeneity or some re-equilibration among different β-amyloid(1-40) oligomer species during the column separation. Hence, while the HPLC data is instructive, it appears challenging to extract a molecular level understanding of the sizes of the different oligomers of β-amyloid(1-40).

3.3.2 Size determination of the fluorescently labeled β-amyloid(1-40) oligomers

At 10μW laser power under the confocal scanning microscope, the HiLyte Fluor^{TM} 488 fluorophores that are labeled on β-amyloid(1-40) peptides would typically photobleach within a few seconds, occasionally extending to more than 30 seconds. Figure 3.2 (a) shows a typical fluorescence confocal scanning image of the coverglass surface coated with HiLyte FluorTM 488 labeled β-amyloid oligomers, as well as a few typical photobleaching trajectories (Figure 3.2 (b)-(d)).

Among all the trajectories that were collected, about 40% are “clean” trajectories (only shot noise present) with recognizable photobleaching events (Figure 3.2 (b) and (c) as examples, showing the trajectories of a dimer and a hexamer). The remaining 60% contain significant intensity fluctuations (much larger than shot noise) that lack any resolvable photobleaching features (Figure 3.2 (d) is an example). This may be due to the fluorophores’ dipole movement and/or interactions with the coverglass surface impurities, charges, etc. While we have determined that cleaning the coverglass reduces the number of trajectories containing these fluctuations, it has not been possible at this point to improve the performance beyond the current ca. 40% of “clean” trajectories. Since we could only reliably use the “clean” trajectories to determine the total number of photobleaching events and extract the oligomer size, only these were considered in our data analysis.

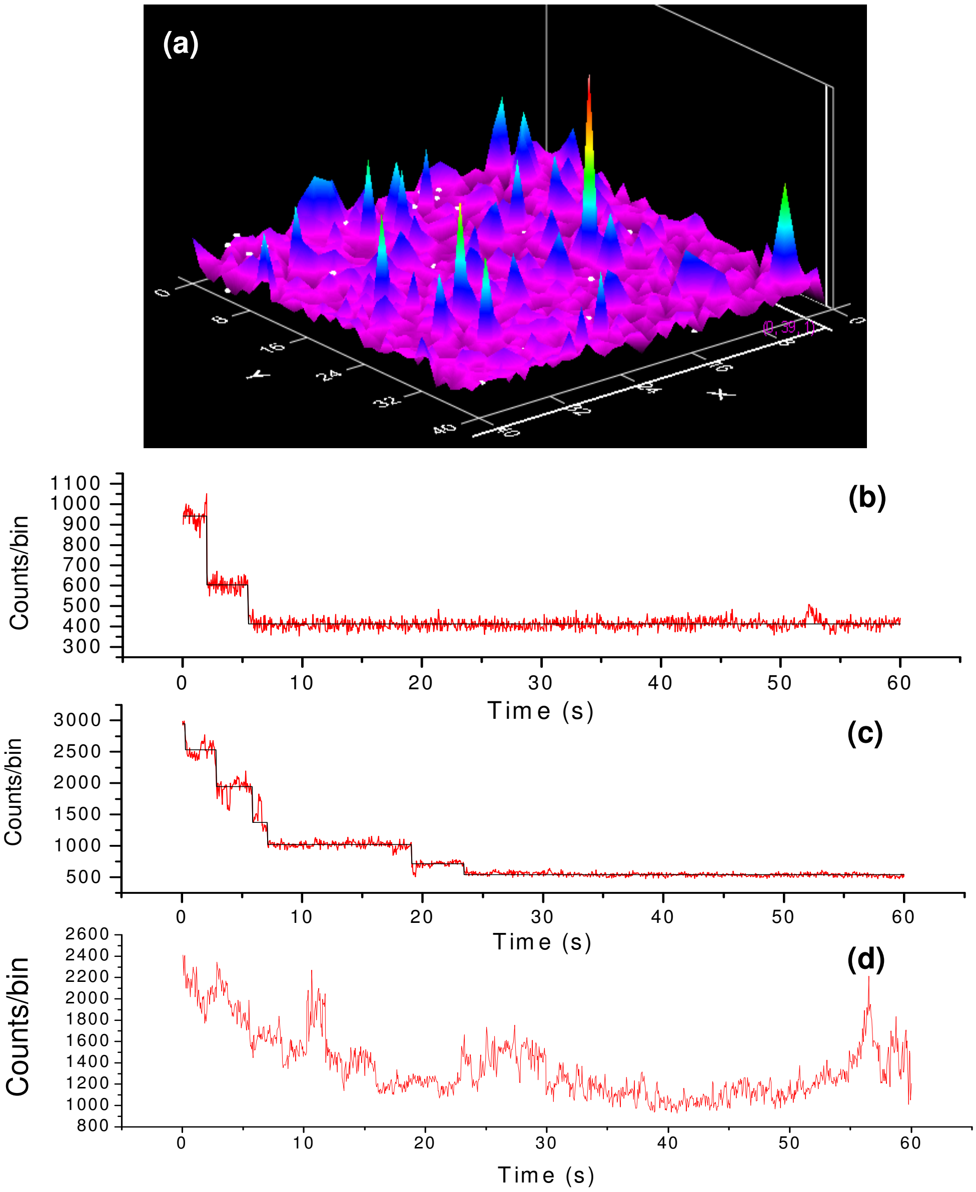

Figure 3.2: Confocal scanning image and photobleaching trajectories (a) A typical fluorescence confocal scanning image (40×40 pixels for 20×20 μm^2), and (b-d) three photobleaching trajectories of HiLyte Fluor^{TM} 488 Aβ(1-40) oligomers: (b) a dimer, (c) a hexamer and (d) an example of trajectory with fluctuations that makes determining the number of photobleaching steps ambiguous. These trajectories are removed from the data set.

Dark states were also occasionally observed in the photobleaching trajectories. These appear as photobleaching events but recover (usually to the original fluorescence intensity level) after some time. The reason for this behavior is not clear but could be due to electron traps within the fluorophore local environment or to slow changes in the fluorophore dipole orientation, since the β-amyloid(1-40) oligomers were non-specifically adsorbed onto the coverglass surface. Agarose gel was also tested as a matrix for immobilizing β-amyloid(1-40) oligomers for single molecule experiments. However, the large "pore" size in agarose gel makes it very difficult to trap peptide monomers, and the high viscosity also makes an even distribution of oligomers in the agarose gel very unlikely.

3.3.3 Construction of the β-amyloid(1-40) oligomer size distribution

Using the photobleaching trajectories of a large number of individual HiLyte Fluor^{TM} 488 β-amyloid(1-40) oligomers, it is possible to construct an oligomer size distribution by making a histogram of the number of photobleaching events in each trajectory, which represents the number of subunits in each photobleached oligomer.

As a demonstration of the ability to differentiate different oligomer distributions using the single molecule spectroscopy approach, we used a sample of unresolved HiLyte Fluor^{TM} 488 β-amyloid(1-40) and a sample of the monomer/dimer fraction collected from the HPLC gel filtration (indicated in Figure 3.3 inset). The unresolved β-amyloid(1-40) sample is expected to be a mixture of oligomers of different sizes, while the gel filtration separated fraction is expected to contain only monomers and dimers.

Figure 3.3 compares the histograms obtained for these two different samples. This comparison clearly confirms the higher degree of heterogeneity of the unresolved sample compared to the gel filtration separated sample. More importantly, the histogram shows that the single molecule approach can distinguish between the two mixtures and that oligomers as large as hexamers are found in the unchromatographed mixture. The HPLC separation does not detect oligomers larger than tetramers, possibly because interactions with the column result in a breakup of the larger oligomers.

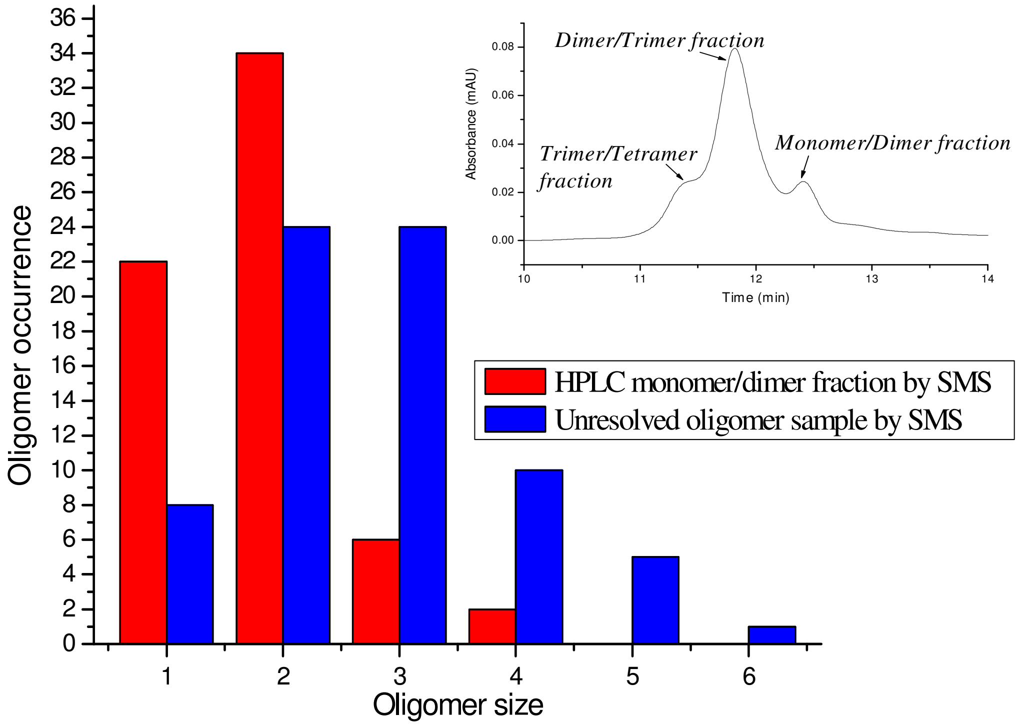

Figure 3.3: Oligomer size distribution comparison between an unresolved β-amyloid(1-40) sample and gel filtration chromatography separated Monomer/Dimer sample (The inset presents the same data shown in Figure 3.1, shown here for convenience). The monomer/dimer fraction was deposited onto coverglass immediately after its collection from the column. The single molecule approach found significant contributions from larger oligomers compared to the HPLC. Please note that these are raw data and corrections are needed as described below.

3.3.4 A bias in the oligomer size distribution, and the correction for it

It has been shown in Chapter II that though the stochastic simulation does not prove the proposed dipole orientation model for the origin of the variability of the trajectories, it supports the notion that different dipole orientations are a major contributor to the variations in the photobleaching trajectories. Besides its likely important contribution to the fluorescence variation, the random dipole orientation model also suggests some possible systematic errors embedded in the data.

For the photobleaching experiments with the confocal scanning microscope, a threshold needs to be pre-set such that, when the detected fluorescence signal is higher than this threshold, the scanning is paused and the recording of a photobleaching trajectory triggered. This helps ignore background fluorescence and prevent any unwanted triggering by the occasionally very high local background noise from the coverglass. However, thresholding may also bias the data set towards brighter fluorophores, thus against monomers and to a less extent other small oligomers. (Note: with TIRF microscopy, a thresholding process is also required in the image processing for the identification of individual oligomers (see Appendix B). Thus the collected data are subject to the same bias.)

In order to quantify the effect of thresholding, another stochastic simulation was performed. In this simulation, the same photobleaching trajectory generation program described in Chapter II was used. Based on the discussion above it is expected that, depending on the initial fluorescence intensities of these simulated trajectories, some will be recorded while others will be missed being below the preset threshold. Hence, for each oligomer species, we let the program continuously generate photobleaching trajectories, until the number of the 'observed' (above threshold) trajectories matched that in our experimental single molecule data. The total number of these generated trajectories contains both 'recorded' and 'missed' oligomers, and thus represents the corrected number for those specific oligomeric species. Due to the stochastic nature of this simulation, it was repeated 10,000 times for each oligomer species. Figure 3.4 shows a comparison of the observed oligomer distribution from Figure 3.3 and the corrected distribution of the same data.

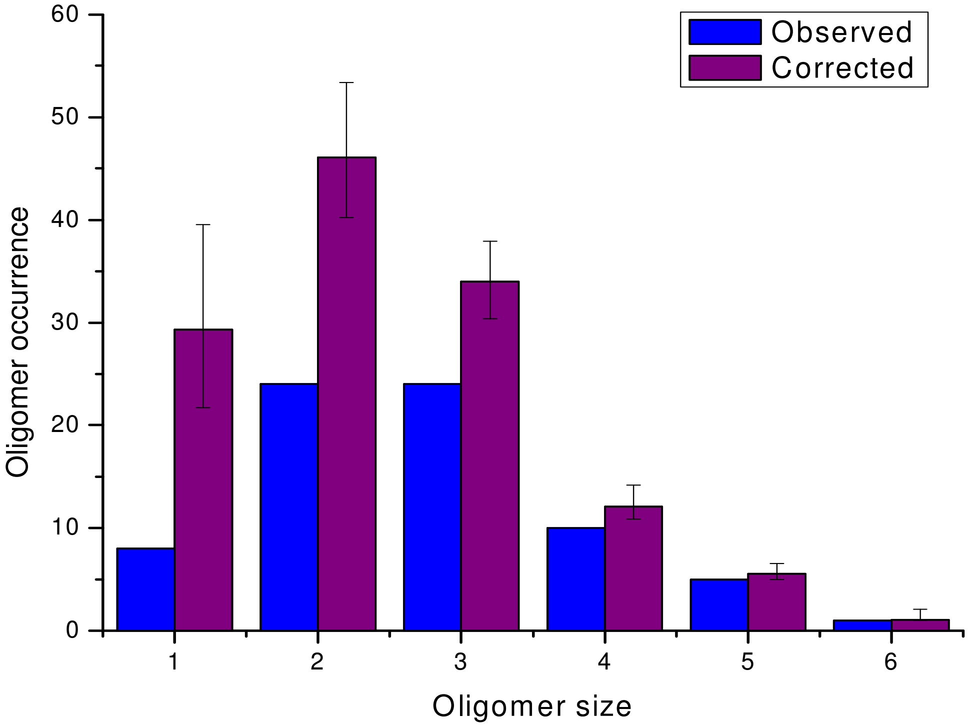

Figure 3.4: Comparison of the observed oligomer distribution and the corrected oligomer distribution.

Not surprisingly, the effect of the correction decreases with the increase in oligomer size, since the more fluorophores an oligomer contains, the less likely it is to be missed due to thresholding. The simulation results confirmed this. It should also be noted that, in this simulation, an empirical value was used to estimate the maximum fluorescence emission rate from a single fluorophore under the microscope (This corresponds to the fluorophores that are at the center of the beam focus and whose dipole orientations are along the excitation field). Different values for this maximum emission rate yield slightly different corrected distributions, but the overall shape of the corrected oligomer distributions remain similar.

3.3.5 A control experiment verifying the correction to the oligomer distribution

To test the validity of our procedure for correcting the photobleaching-derived distribution, we did a control experiment on dye labeled parvalbumin. The mass spectroscopy data of this parvalbumin sample indicates a 48.6% single labeling, 44.5% double labeling, and 6.9% triple labeling mixture. Figure 3.5 shows the comparison of the corrected single molecule spectroscopy data with the mass-spec data. It clearly demonstrates that our single molecule approach can accurately reconstruct the correct distribution of the studied sample. (Note: The smaller error bars here compared to those in Figure 3.4 are due to an improved thresholding algorithm with an EMCCD camera used in the control experiment. The real errors, however, should be larger than those error bars because the uncertainties of the empirical estimates used in the simulation were not indicated in the figure.)

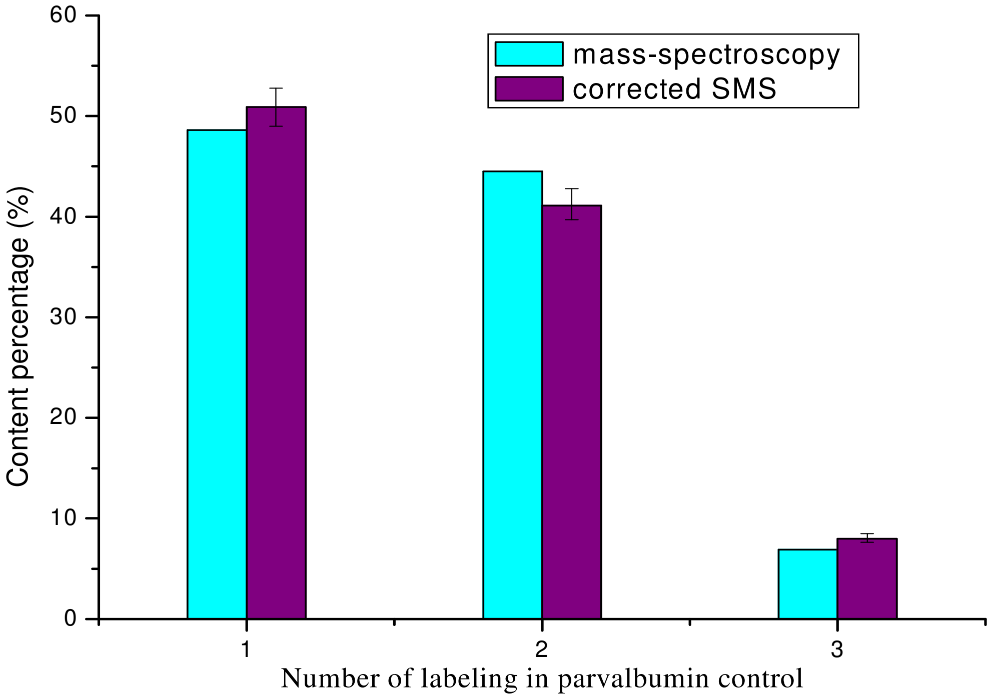

Figure 3.5: Comparison of the mass-spectroscopy distribution with the corrected single molecule distribution in the parvalbumin control experiment.

Besides the threshold effect, there are other factors that might cause systematic errors in the estimation of oligomer size, such as self-quenching between fluorophores within an oligomer, which could result in an underestimate of this size. Also, the random dipole orientation assumption may not represent the true distribution for real samples on coverglass, and possible slow movements of fluorophore dipoles on the coverglass will complicate the data analysis as well. In general, an immobilization of free rotating oligomers in aqueous environment will be preferable.

3.3.6 β-amyloid(1-40) oligomer size distribution: the comparison between single photobleaching and HPLC gel filtration

We did a further analysis on our β-amyloid(1-40) sample by comparing the single molecule data with the HPLC gel filtration-derived oligomer distribution of the same sample. This allows us to gain more insight into this heterogeneous and dynamic mixture.

In order to correlate these two sets of data, a multiple Gaussian distribution fitting was applied to the gel filtration elution profile as shown in Figure 3.6. Depending on the choice of the fitting windows and on the initial parameters, this procedure yields several different fits with only slightly different peak heights, widths, and positions, and with nearly the same quality of fit. Figure 3.6 shows a typical fit with four Gaussian peaks and a fifth, low and broad distribution describing the slowly varying background. According to their elution times, these four peaks most probably represent four different oligomer species: monomer, dimer, trimer, and tetramer, respectively.

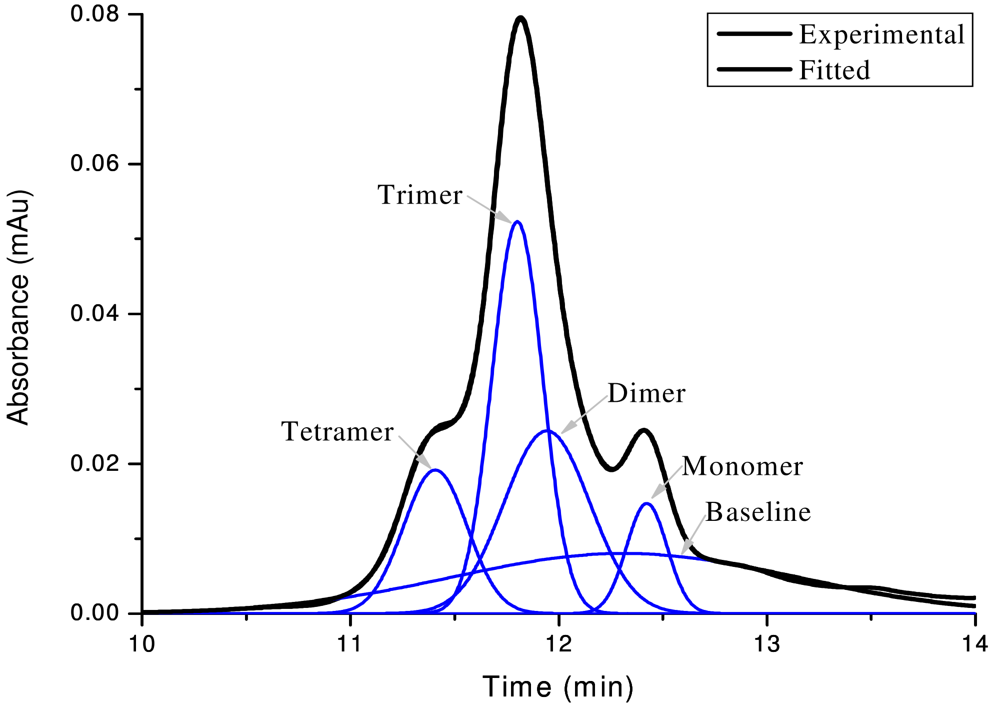

Figure 3.6: Multiple Gaussian fitting applied to the gel filtration elution profile. The ‘experimental’ curve indicates the raw data of the elution profile; the’ fitted’ curve indicates a typical good fitting result, which is the summation of monomer, dimer, trimer, tetramer, and baseline. These two curves are well on top of each other.

Integration of the area under each peak yields the total far UV absorption for each β-amyloid (1-40) oligomer species. Assuming that the average absorptivity of the peptide backbone does not change upon oligomerization (i.e., that the average absorptivity of a dimer is twice of that of a monomer), an oligomer size distribution of β-amyloid(1-40) was derived from the absorption of each specie. This was done for each of the best four fits to the HPLC elution profile, and an averaged oligomer distribution was derived. A similar relative distribution was constructed from the corrected single molecule data shown in Figure 3.4. Figure 3.7 presents the comparison of these two relative distributions obtained from our two different methods.

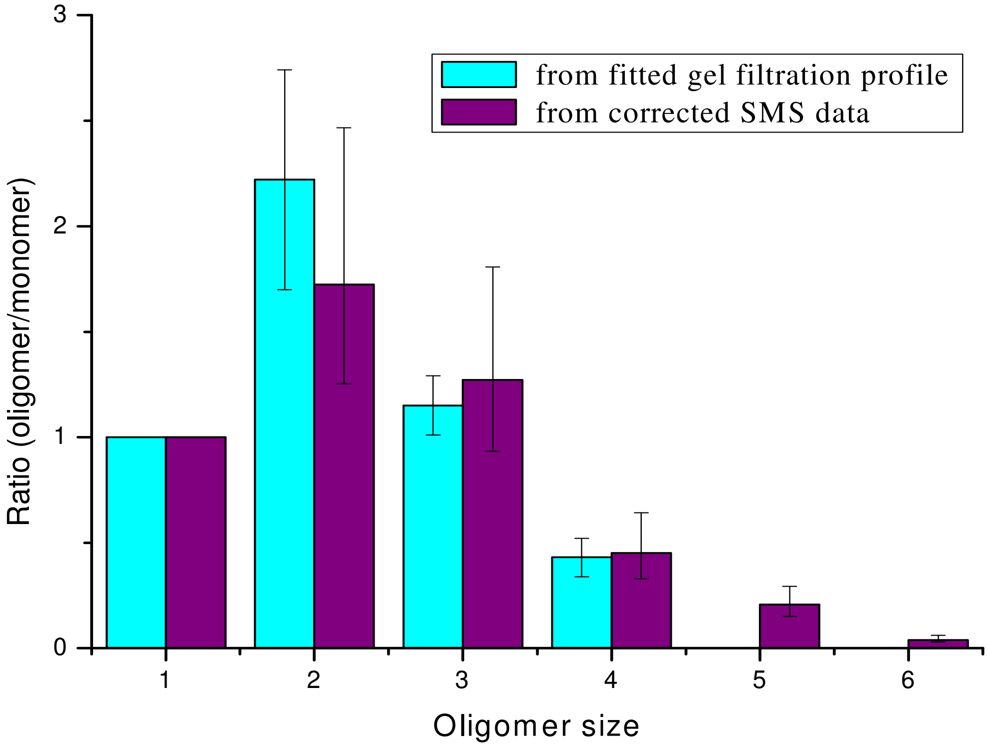

Figure 3.7: Comparison of the relative oligomer size distributions derived from different data sets: gel filtration profile and the corrected single molecule data. The data are normalized so that they give the same ratio for the monomer.

The results show good agreement on the oligomer size distribution between the single molecule approach and the gel filtration chromatography approach. This indicates that the re-equilibration of the oligomer distribution is not very fast for our experimental conditions for gel filtration chromatography, thus both approaches are able to quantitatively reconstruct the oligomer size distribution.

However, the single molecule approach has some other advantages. Single molecule methodologies work at nano-molar or lower sample concentration, which could be extremely beneficial for β-amyloid studies. The determination of oligomer size is more direct in a single molecule approach. In addition, there is some ambiguity on determining the oligomer size in the gel filtration method since the positions of the elution peaks do not correspond to individual oligomers very well. There is also a broad baseline peak indicating the existence of an interaction between some labeled peptides and column material. In our results, the single molecule approach has successfully detected oligomers larger than tetramers, while the gel filtration method missed them. This suggests that β-amyloid (1-40) oligomers that are larger than a tetramer might not be stable during gel filtration. These large oligomers might have re-equilibrated themselves into smaller species during the separation, contributing to the baseline peak. Importantly for future experiments, the single molecule approach allows to study oligomer sizes on membranes, which is very difficult to do using HPLC since the membrane/detergent interferes with the separation.

3.4 Conclusions

In this chapter, an approach based on single molecule spectroscopy was used to study the heterogeneity of HiLyte Fluor^{TM} 488 β-amyloid(1-40) oligomers. Fluorescently labeled β-amyloid(1-40) oligomer mixture was ‘frozen’ at a given time point by depositing it onto coverglass. The surface bound oligomers were then photobleached, and the number of subunits in individual oligomers was determined by counting the photobleaching events.

By constructing a histogram of the number of subunits in all the individual oligomers, an oligomer size distribution was extracted, which was then corrected according to our computer simulations. As an indication of heterogeneity, the oligomer size distribution reveals the intrinsic properties of a given β-amyloid(1-40) oligomer mixture at a given time point. Besides the work described above, the single molecule approach can also be used to extract dynamic information. Real time monitoring of oligomer formation is possible if the laser power is lowered and the observation time window extended. Hence, single molecule spectroscopy has the potential to also be used to reveal transient events, which might occur in such a dynamic and heterogeneous mixture and might be masked by any ensemble-averaging measurements.

For large oligomers (we have identified oligomers as large as 8 by photobleaching), the photobleaching events in the fluorescence trajectory may become more difficult to distinguish and in some cases, self-quenching among the fluorophores may increase as well. However, since most of the recent evidence points to small oligomers, such as the pore-like annular structures which are probably made of hexamer units, as the pathologically relevant species in Alzheimer's disease (10-13), the single molecule approach appears very promising for studies on these small oligomers. We anticipate that the detailed information on the early oligomers of β-amyloid peptides gained through single molecule techniques will provide deeper understanding of Alzheimer’s disease.

Reference

1. Alzheimer, A., Stelzmann, R. A., Schnitzlein, H. N., and Murtagh, F. R. (1995) An English translation of Alzheimer's 1907 paper, "Uber eine eigenartige Erkankung der Hirnrinde", *Clin Anat 8*, 429-431.

2. Luhrs, T., Ritter, C., Adrian, M., Riek-Loher, D., Bohrmann, B., Dobeli, H., Schubert, D., and Riek, R. (2005) 3D structure of Alzheimer's amyloid-beta(1-42) fibrils, *Proc. Natl. Acad. Sci. U.S.A. 102*, 17342-17347.

3. Harper, J. D., and Lansbury, P. T., Jr. (1997) Models of amyloid seeding in Alzheimer's disease and scrapie: mechanistic truths and physiological consequences of the time-dependent solubility of amyloid proteins, *Annu. Rev. Biochem. 66*, 385-407.

4. Selkoe, D. J. (1991) The molecular pathology of Alzheimer's disease, *Neuron 6*, 487-498.

5. Glenner, G. G., and Wong, C. W. (1984) Alzheimer's disease: initial report of the purification and characterization of a novel cerebrovascular amyloid protein, *Biochem. Biophys. Res. Commun. 120*, 885-890.

6. LaFerla, F. M., and Oddo, S. (2005) Alzheimer's disease: Abeta, tau and synaptic dysfunction, *Trends Mol. Med. 11*, 170-176.

7. Bitan, G., and Teplow, D. B. (2004) Rapid Photochemical Cross-Linking-A New Tool for Studies of Metastable, Amyloidogenic Protein Assemblies, *Acc. Chem. Res. 37*, 357 -364.

8. Watson, D., Castaño, E., Kokjohn, T. A., Kuo, Y. M., Lyubchenko, Y., Pinsky, D., Connolly, E. S., Esh, C., Luehrs, D. C., Stine, W. B., Rowse, L. M., Emmerling, M. R., and Roher, A. E. (2005) Physicochemical characteristics of soluble oligomeric Aβ and their pathologic role in Alzheimer's disease, *Neurol. Res. 27*, 869-881.

9. Lansbury Jr., P. T. (1999) Evolution of amyloid: What normal protein folding may tell us about fibrillogenesis and disease, *Proc. Natl. Acad. Sci. U.S.A. 96*, 3342-3344.

10. Quist, A., Doudevski, I., Lin, H., Azimova, R., Ng, D., Frangione, B., Kagan, B., Ghiso, J., and Lal, R. (2005) Amyloid ion channels: A common structural link for protein-misfolding disease, *Proc. Natl. Acad. Sci. U.S.A. 102*, 10427-10432.

11. Lyubchenko, Y. L., Sherman, S., Shlyakhtenko, L. S., and Uversky, V. N. (2006) Nanoimaging for protein misfolding and related diseases, *J. Cell. Biochem. 99*, 52–70.

12. Losic, D., Martin, L. L., Mechler, A., Aguilar, M. I., and Small, D. H. (2006) High resolution scanning tunnelling microscopy of the β-amyloid protein (Aβ1–40) of Alzheimer's disease suggests a novel mechanism of oligomer assembly, *J. Struct. Biol. 155*, 104-110.

13. Lashuel, H. A., Petre, B. M., Wall, J., Simon, M., Nowak, R. J., Walz, T., and Lansbury Jr., P. T. (2002) α-Synuclein, Especially the Parkinson's Disease-associated Mutants, Forms Pore-like Annular and Tubular Protofibrils, *J. Mol. Biol. 322*, 1089-1102.

14. Bitan, G., Kirkitadze, M. D., Lomakin, A., Vollers, S. S., Benedek, G. B., and Teplow, D. B. (2003) Amyloid β-protein (Aβ) assembly: Aβ40 and Aβ42 oligomerize through distinct pathways, *Proc. Natl. Acad. Sci. U.S.A. 100*, 330-335.

15. Sabella, S., Quaglia, M., Lanni, C., Racchi, M., Govoni, S., Caccialanza, G., Calligaro, A., Bellotti, V., and Lorenzi, E. D. (2004) Capillary electrophoresis studies on the aggregation process of beta-amyloid 1-42 and 1-40 peptides, *Electrophoresis. 25*, 3186-3194.

16. Wong, C.W., Quaranta, V., and Glenner, G. G. (1985) Neuritic plaques and cerebrovascular amyloid in Alzheimer disease are antigenically related, *Proc. Natl. Acad. Sci. U.S.A. 82*, 8729–8732.

17. Zagorski, M. G., Yang, J., Shao, H., Ma, K., Zeng, H., and Hong, A. (1999) Methodological and Chemical Factors Affecting Amyloid β Peptide Amyloidogenicity. *Methods-Enzymol. 309*, 189-204.

18. Thomas, R. M., Zampieri, A., Jumel, K., and Harding, S. E. (1997) A trimeric, alpha-helical, coiled coil peptide: association stoichiometry and interaction strength by analytical ultracentrifugation, *Eur. Biophys. J. 25*, 405-410.

CHAPTER IV

Single Molecule Studies of β-amyloid(1-40) Peptide Interacting with Supported Anionic Lipid Membrane

4.1 Introduction

The formation of senile plaques in the brain tissue of patients has been the hallmark of Alzheimer's disease (1-3). It has been found that β-amyloid peptides, which are 39-43 amino acid residues in length, are the major component of these plaques (4-6). And among all the β-amyloid isoforms, β-amyloid(1-40) peptide is the most abundant one. It has also been shown that β-amyloid peptides can self-assemble and form highly ordered fibrillar structures in aqueous solution (7, 8).

Due to their presence in Alzheimer's disease patients' brains, these β-amyloid fibrils have been believed to be neurotoxic to neuronal cells and were often linked to the cause of the disease (9, 10). However, recent experimental evidence has indicated that the early β-amyloid oligomers, rather than the mature fibrils, might be the neurotoxic species (11-14). This led to a new hypothesis for the neurotoxicity mechanism in Alzheimer's disease, namely that β-amyloid peptides form ion conducting pores in neuronal cell membranes, and the resulting imbalance of calcium ions across the membranes can either lead to direct cell death or trigger the signaling for apoptosis (15). Small oligomeric structures, which consist of a minimum of 4~6 monomeric units, are likely to be involved in the pore formation in the membrane (13, 16). Moreover, anionic membranes have been documented as required in the pore formation process (17-21).

Despite the growing research effort on these early β-amyloid oligomers, the study of these potentially pore forming species is very challenging, because they are heterogeneous, dynamic, and exist at extremely low physiological concentrations. Single molecule techniques have been shown to be very promising tools for studying these small oligomeric structures, since individual β-amyloid oligomers can be detected and identified at very low peptide concentrations.

In this work, we used single molecule imaging techniques to study the interactions between β-amyloid(1-40) peptide and supported anionic lipid membrane. The study of this peptide membrane interaction is essential for understanding the mechanism of β-amyloid neurotoxicity. In our experiments, the evolution of β-amyloid species in anionic lipid membranes was monitored for up to a few days. The results indicate a tight, uniform binding of β-amyloid(1-40) peptide to the lipid membrane, followed by oligomer formation in the membrane. This result is in good agreement with a two-state model proposed for peptide membrane interactions (22, 23). The concentration dependent oligomer formation observed in our single molecule experiments suggests there are two different pathways of oligomer formation in the membrane. The different oligomer species formed via the two pathways were then compared.

4.2 Methods

4.2.1 β-amyloid(1-40) preparation

The HiLyte Fluor^{TM} 488 β-amyloid(1-40) (AnaSpec, San Jose, CA) was kept frozen at -20°C upon being received. For the purpose of consistency, the peptide was re-dissolved in 2% Ammonium Hydroxide (J. T. Baker Inc., Phillipsburg, NJ) at 1mg/ml, then aliquotted into small samples, and finally lyophilized and stored at -20°C. To make a fresh β-amyloid(1-40) solution, the lyophilized powder was directly dissolved into 10mM Sodium Phosphate, 100mM Sodium Chloride, pH7.4 buffer. In all the experiments conducted in this work, only freshly dissolved β-amyloid(1-40) peptide was used.

4.2.2 TIRF Microscopy

Fluorescence emission from HiLyte Fluor^{TM} 488 β-amyloid(1-40) peptide was collected by a custom made inverted TIRF (Total Internal Reflection Fluorescence) microscope. The microscope was equipped with a 1.45NA 60X oil-immersion objective (Olympus, Center Valley, PA). The excitation source was an Ar^+-ion laser (I-90, Coherent, Santa Clara, CA) at 488.0 nm. The fluorescence signal was filtered by a 520/60 nm band-pass filter (Chroma, Rockingham, VT), and recorded by an EMCCD camera (Electron Multiplying CCD camera, Andor, South Windsor, CT). Due to the evanescent wave in the TIRF geometry, only fluorophores that are very close to the glass/water interface (~150nm) are excited and detected. The details of the microscopy techniques and instrumentation can be found in Chapter II.

4.2.3 Supported Anionic Lipid Membrane preparation

Palmitoyl-2-Oleoyl-sn-Glycero-3-Phosphocholine (POPC) and 1-Palmitoyl-2-Oleoyl-sn-Glycero-3-[Phospho-rac-(1-glycerol)] (POPG) (both from Avanti Polar Lipids, Alabaster, AL) (see figure 4.1 (a) for structures) were kept at -20°C upon being received. In all of our experiments, a mixture of POPC (neutral/zwitterionic) and POPG (negative) lipids was used to form the supported anionic membranes on coverglasses (Fisher Scientific, Pittsburgh, PA). These coverglasses had been pre-cleaned with MilliQ (Millipore, Billerica, MA) water rinsing followed by kiln baking at ~500°C for two hours.

In order to form an anionic lipid membrane on a coverglass, small unilamellar vesicles (SUVs) were first made (24). 0.5mg POPC and 0.5mg POPG were mixed in chloroform, and then dried under gaseous nitrogen in a fume hood. A further removal of the residual chloroform was achieved by vacuum drying of the sample overnight. Before the preparation for SUVs, the dried lipids were hydrated in buffer (10mM Sodium Phosphate, 100mM Sodium Chloride, pH 7.4) for 2 hours at room temperature, during which the sample was vortexed a few times to completely re-suspend the lipids. SUVs were then formed by sonication of the lipid suspension in an ice water bath for 2-5min until the suspension became clear. Finally the supported lipid membranes were spontaneously assembled during the incubation of the freshly prepared SUVs on a clean coverglass surface and let stand overnight (see figure 4.1 (b)) (25). After the formation of the supported lipid membranes, the unbound SUVs were gently washed off with buffer.

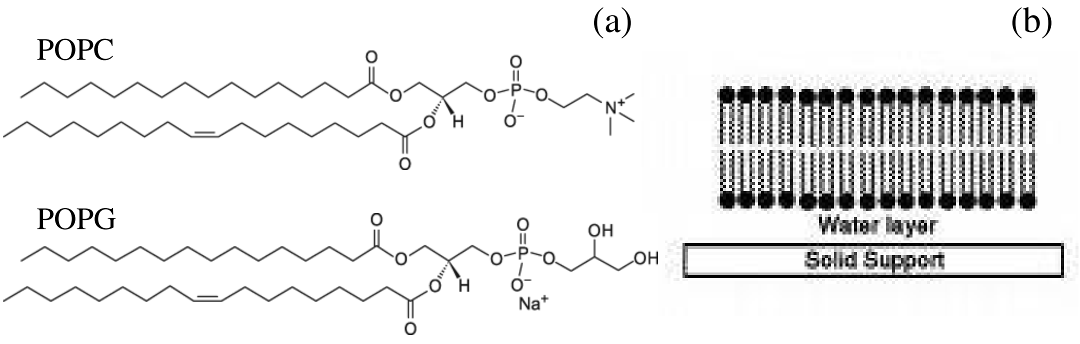

Figure 4.1: POPC & POPG lipid molecules, and lipid bilayer. (a) shows the structures of POPC and POPG lipid molecules. (b) shows the formation of a lipid bilayer on a solid surface.

4.2.4 Application of FRAP to determine membrane fluidity

FRAP (Fluorescence Recovery After Photobleaching) experiments (26, 27) were used to measure the mobility of the lipid molecules (or the membrane bound β-amyloid(1-40) peptide) in the membranes. In a typical FRAP experiment, a circular area of about 45μm in diameter in the membrane was photobleached by high intensity laser illumination for a very short duration (5sec). Then the fluorescence recovery in the photobleached region was recorded with much weaker illumination intensity (1/2500 of the photobleaching power). Since all the free lipid molecules (or β-amyloid(1-40) peptide) in solution had been washed off extensively, the fluorescence recovery was purely due to the lateral diffusion of the lipid molecules (or the membrane bound β-amyloid(1-40) peptide) in the membrane.

In order to extract the diffusion coefficient and recovery percentage from the FRAP experiments, the fluorescence recovery curves were fit to the following equation (27) using Mathematica: $f(t) = \exp(-2\tau_D / t)[I_0(2\tau_D / t) + I_1(2\tau_D / t)]$. In this equation,

$f(t)$ is the integrated fluorescence intensity over the photobleached region: I_0 and I_1 are the modified Bessel functions of the first kind ($I_n(z) = \frac{1}{2\pi i}\oint e^{(z/2)(t+1/t)} t^{-n-1} dt$). And $\tau_D = w^2 / 4D$ is the characteristic diffusion time, with w being the radius of the photobleached region, and D being the diffusion coefficient.

4.3 Results

All the experiments presented in this chapter started with the formation of a supported anionic membrane on a clean coverglass, followed by the addition of HiLyte Fluor$^{\text{TM}}$ 488 β-amyloid(1-40) peptide to the membrane. A TIRF microscope was then used to monitor the interactions between the peptide and the membrane. Depending on the concentration of the added β-amyloid(1-40), the peptide-membrane interactions were monitored for a period of a few hours (with high peptide concentration in solution, ~100nM) to over six days (with low peptide concentration in solution, ~nM).

Based on the results observed under the TIRF microscope, the interactions between β-amyloid(1-40) peptide and anionic membrane can be divided into two stages, uniform binding and oligomer formation. During these two stages, a tight and uniform binding of β-amyloid(1-40) peptide to the anionic membrane, and the formation of β-amyloid(1-40) oligomers in the membrane were observed, respectively.

4.3.1 Uniform binding

After the addition of freshly dissolved HiLyte Fluor$^{\text{TM}}$ 488 β-amyloid(1-40) to the anionic membrane, a uniform binding of the peptide to the membrane was observed (see figure 4.2 (a), revealed by an elevated fluorescence background, the variation in the background intensity corresponds to the TIR illumination pattern). The duration of the uniform binding ranges from less than two hours (for high peptide concentration in solution, ~100nM) to a few days (for low peptide concentration in solution, ~2nM).

4.3.1.1 Binding Kinetics

During the period of uniform binding, the observed fluorescence intensity from the membrane bound β-amyloid(1-40) continued to increase, indicating the solution peptide continued to bind to the membrane (see figure 4.2 (b), the fluorescence intensity in the binding plot represents the mean value of the field of view shown in figure 4.2 (a)). The binding plot is well fit by a single exponential, suggesting the binding process obeys first order kinetics.

The following model was proposed for the binding process: $[Membrane Binding Sites]+[Free A\beta]\xleftrightarrow[k_{off}]{k_{on}}[Membrane Bound A\beta]$. We can further simplify this model based on the following two observations in our experiments.

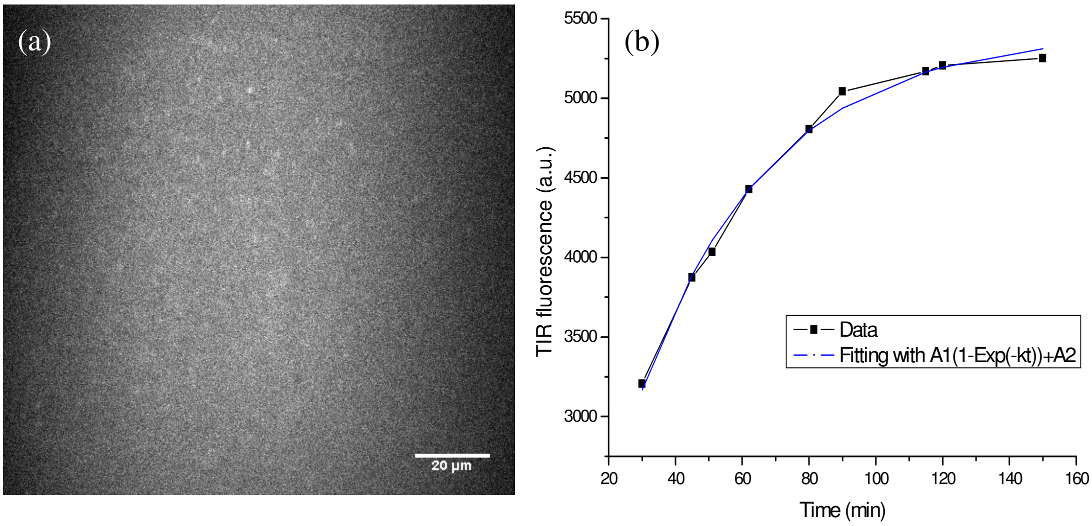

Figure 4.2: The uniform binding, and the binding kinetics of β-amyloid(1-40) peptide to anionic membrane. (a) shows a typical TIRF image of HiLyte Fluor^{TM} 488 β-amyloid(1-40) peptide bound to POPC:POPG (50%:50%) lipid membranes. (b) shows the kinetics of the β-amyloid(1-40) peptide binding to the same membrane. The data could be well fit to a single exponential, indicating a first order binding kinetics.

The first observation is that k_{off} is extremely small. In our experiment, after the unbound β-amyloid(1-40) was washed off extensively, the fluorescence intensity of the membrane bound peptide did not show any noticeable decrease over our longest observation period of 130 hours. This set the upper limit of k_{off} to be less than $2\times 10^{-6} s^{-1}$.

The second observation is that small amount of membrane bound peptide saturates the binding of β-amyloid(1-40) to the membrane. We found that the concentration of the free β-amyloid(1-40) in solution, as measured by its fluorescence intensity, did not measurably decrease over the entire binding process. This indicates that the fraction of peptide that bound to the membrane was extremely small ($[Free\ A\beta] \approx$

$[Free\ A\beta]_0 >> [Membrane\ Bound\ A\beta]$). The density of the membrane bound β-amyloid(1-40) peptide will be further discussed in the discussion session.

Combining the above two observations, the model for β-amyloid(1-40) peptide binding to lipid membranes can be simplified as: $[MembraneBinding\,Sites] + [FreeA\beta]_0 \xrightarrow{k_{on}} [MembraneBound\,A\beta]$. Therefore, the binding process shown in figure 4.2 (b) is described by a single exponential curve $A_1(1-Exp(-k_{on}[FreeA\beta]_0 \times t))+A_2$. $k_{on} = (4.3 \pm 0.4) \times 10^3 s^{-1} M^{-1}$ was extracted from the curve fitting. With the estimated upper limit for k_{off} ($< 2 \times 10^{-6} s^{-1}$), the dissociation constant for the peptide from the membrane can be calculated: $K_d = k_{off} / k_{on} < 470pM$. This extremely low K_d indicates a very tight binding of β-amyloid(1-40) peptide to the anionic membrane.

4.3.1.2 The membrane bound β-amyloid(1-40) is very mobile

The mobility of lipid molecules or of the membrane bound β-amyloid(1-40) peptide was measured by FRAP (Fluorescence Recovery After Photobleaching) experiments. A circular region in the membrane was photobleached, and the recovery process due to lateral diffusion was then recorded (Figure 4.3 (a)-(d) show four typical images in a FRAP experiment. In order to measure the mobility of the lipid molecules, the membrane was made using lipids containing 0.5% NBD-POPC (Avanti Polar Lipids, Alabaster, AL) for the purpose of fluorescence imaging). The diffusion coefficient can be extracted from the mathematical fitting of the recovery curve to the model above (Figure 4.3 (e) shows the recovery curve of the membrane bound β-amyloid(1-40) peptide and the corresponding curve fitting).

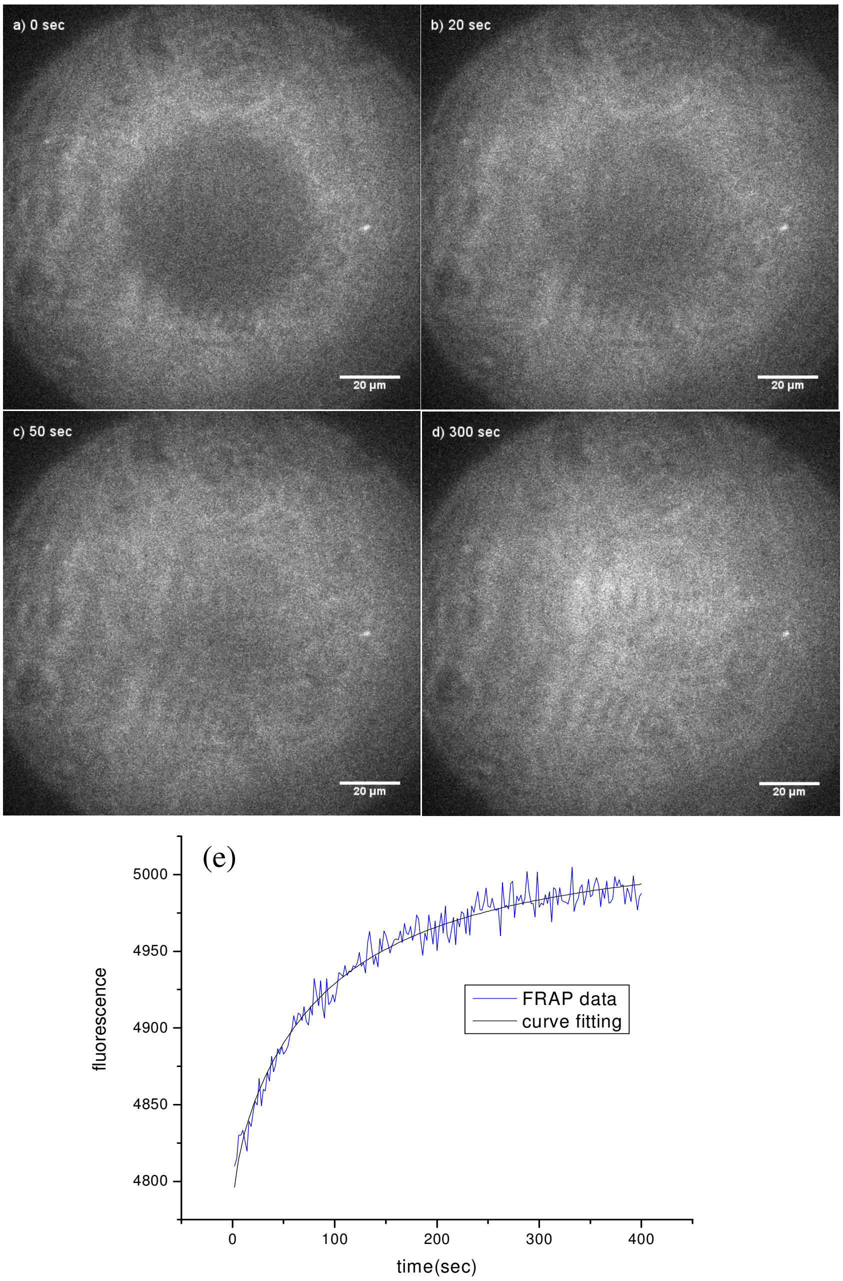

Figure 4.3: FRAP images and recovery curve. (a)-(d) show the snapshot images of the FRAP (Fluorescence Recovery After Photobleaching) experiment. (e) shows the fluorescence recovery curve which was fit to the equation $f(t) = \exp(-2\tau_D / t)[I_0(2\tau_D / t) + I_1(2\tau_D / t)]$ to extract the diffusion coefficient and the recovery percentage.

The diffusion coefficients of both the lipid molecules and the membrane bound β-amyloid(1-40) measured in our FRAP experiments are compared in Table 4.1. These results indicate that the membrane bound β-amyloid(1-40) is very mobile, showing a diffusion coefficient similar to that of the lipid molecules.

	Diffusion Coefficient (μm^2/sec or x$10^{-8}cm^2$/sec)	Recovery Percentage (%)
POPC :POPG lipids	1.6±0.1	91±1
Membrane bound β-amyloid	2.3±0.2	60±1

Table 4.1: The diffusion coefficient and recover percentage comparison between the POPC:POPG lipid molecules and the membrane bound β-amyloid(1-40) peptide

4.3.2 Oligomer formation

After β-amyloid(1-40) peptide bound to the membrane uniformly (Fig. 3(1)), continuing incubation of the sample led to oligomer formation. These oligomers appeared as bright spots in the fluorescence images (see Figure 4.4 (b)-(d)). It was also shown in these images that, the previously bound peptide was still attached to the membrane during oligomer formation, as indicated by the presence of elevated fluorescence backgrounds in all the images. Contrary to those uniformly bound peptide which showed good mobility in the membrane, the oligomers appeared to be stationary.

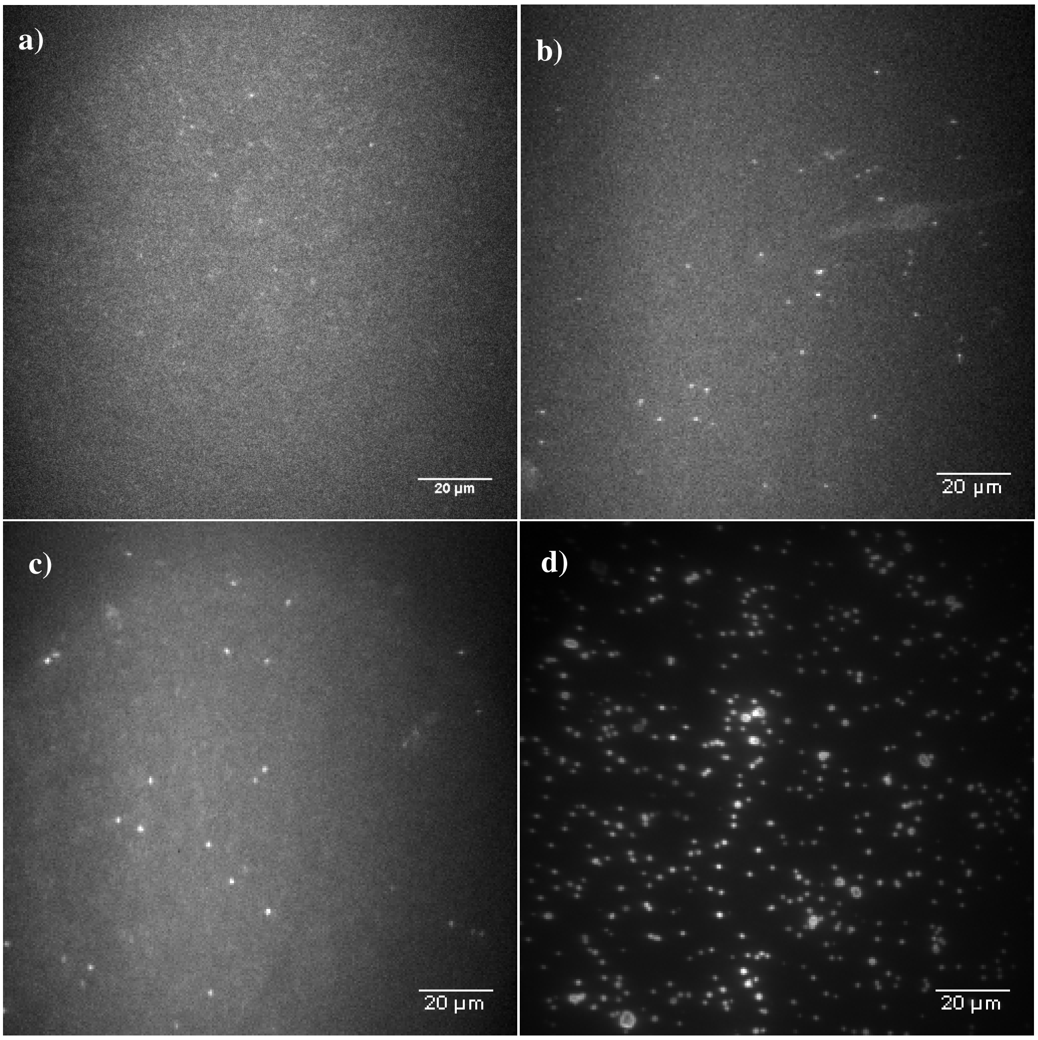

Figure 4.4: Concentration dependent oligomer formation. (a) shows the image before oligomer formation in the membrane. (b)-(d) show that further incubations with different concentrations of β-amyloid(1-40) yielded different degrees of oligomer formation in the membrane: (b) further incubation with NO β-amyloid(1-40) in solution for 130 hours; (c) further incubation with 2nM β-amyloid(1-40) in solution for 130 hours; (d) further incubation with 100nM β-amyloid(1-40) in solution for 3 hours.

4.3.2.1 Concentration dependence of oligomer formation

Our experiments reveal that the rate of oligomer formation in the membrane depends on the concentration of the β-amyloid(1-40) peptide in solution. Therefore, three sets of experiments of oligomer formation with different peptide concentrations were conducted. All the anionic membranes used in these experiments were pre-incubated with β-amyloid(1-40) (for 20 hours with 2nM peptide concentration, or 25 minutes with 100nM peptide concentration), since oligomer formation occurs after a uniform binding of β-amyloid(1-40) to the membrane. The three concentrations used in the experiments were: no peptide (peptide being washed off after the 20 hour pre-incubation), 2nM peptide, and 100nM peptide in solution.

A. Oligomer formation with no peptide in solution

Despite the absence of any β-amyloid(1-40) in solution, monitoring the pre-incubated membrane for 130 hours led to oligomer formation in the membrane (see figure 4.4 (b)). There were 34±4.4 oligomers observed per field of view (~120μm in diameter) after the 130 hour incubation.

Since there was no β-amyloid(1-40) available in solution, these oligomers must have formed within the membrane, and from the β-amyloid(1-40) peptide that bound to the membrane during the pre-incubation.

B. Oligomer formation with low concentration (2nM) of peptide in solution

When the pre-incubated membrane with 2nM β-amyloid(1-40) peptide in solution was followed for 130 hours, a very similar oligomer formation was seen (see figure 4.4 (c)). The number of the observed oligomers per field of view was 41±6.9 in this case, only slightly higher than that observed with no peptide in solution. The fluorescence intensities of the oligomers in both experiments were very similar as well.

Though the large amount of free β-amyloid(1-40) in solution served as a reservoir for oligomer formation, the number of oligomers formed in the membrane was not much different from that without free peptide. This suggests a similar mechanism of oligomer formation in both experiments.

C. Oligomer formation with high concentration (100nM) of peptide in solution

Monitoring the pre-incubated membrane with 100nM β-amyloid(1-40) in solution for only 2.5 hours led to drastically increased oligomer formation (see figure 4.4 (d)). Though the incubation time was much shorter, the density and the fluorescence intensities of the oligomers formed in the membrane were much higher than that in the previous two scenarios. With 100nM peptide in solution, 150±16 oligomers per field of view were observed after the short incubation.

This much faster oligomer formation suggests that these oligomers were formed via a different mechanism. This will be further discussed in the Discussion section.

4.3.2.2 Comparison of oligomer species

In Chapter II, we have developed a methodology based on single molecule photobleaching to quantitatively determine the β-amyloid oligomer sizes. However, when these oligomers were formed in the membrane, the photobleaching of the oligomers yielded much more complicated trajectories, which is believed to be due to the presence of the membrane bound peptide that diffuses in the membrane. Since these membrane bound β-amyloid(1-40) are mobile, they are diffusing around the immobilized oligomers during photobleaching, making the photobleaching trajectories appear quasi-ensemble. This complication hinders the application of the photobleaching technique to characterize the β-amyloid oligomers in the membrane.

Therefore, here we used fluorescence intensity as the indicator of oligomer size in the membrane. However, due to the illumination gradient caused by both the Gaussian profile of the laser beam and the TIRF geometry, the absolute intensities of the oligomers' fluorescence may not always faithfully reflect their sizes. Thus a relative intensity method was developed.

Based on the rationale that smaller regions, such as 9x9 pixels in our images, are more likely to have approximately uniform illumination, a comparison of the oligomer fluorescence relative to that of its local environment can more correctly reflect its size. Mathematically, the relative fluorescence intensity is calculated as the ratio of the intensity of a pixel over the average intensity of the small surrounding region. Thus in these relative fluorescence intensity images, the background pixels, which represent the mobile peptide that bound to the membrane uniformly, have relative fluorescence intensities of around unity, while the oligomers have relative fluorescence intensities well above unity.

Using the relative fluorescence intensity method, the sizes of the oligomers in an image can be correctly compared. Due to the very similar fluorescence intensities in the background pixels in figure 4.4 (c) & (d) (the background in (d) appears to be much darker due to the different contrast setting for image display and gain setting for data acquisition), the sizes of the oligomers in different images can also be compared. From the comparison of the data in figure 4.5 (a) & (b), it was concluded that with a low concentration of peptide in solution small oligomers were formed, since they had much lower brightness and appeared to be diffraction limited objects. In contrast, with a high concentration of peptide in solution, much larger oligomers, which showed much higher brightness and occupied much larger pixel areas, were formed. The sizes of the oligomers will be further analyzed in the Discussion section.

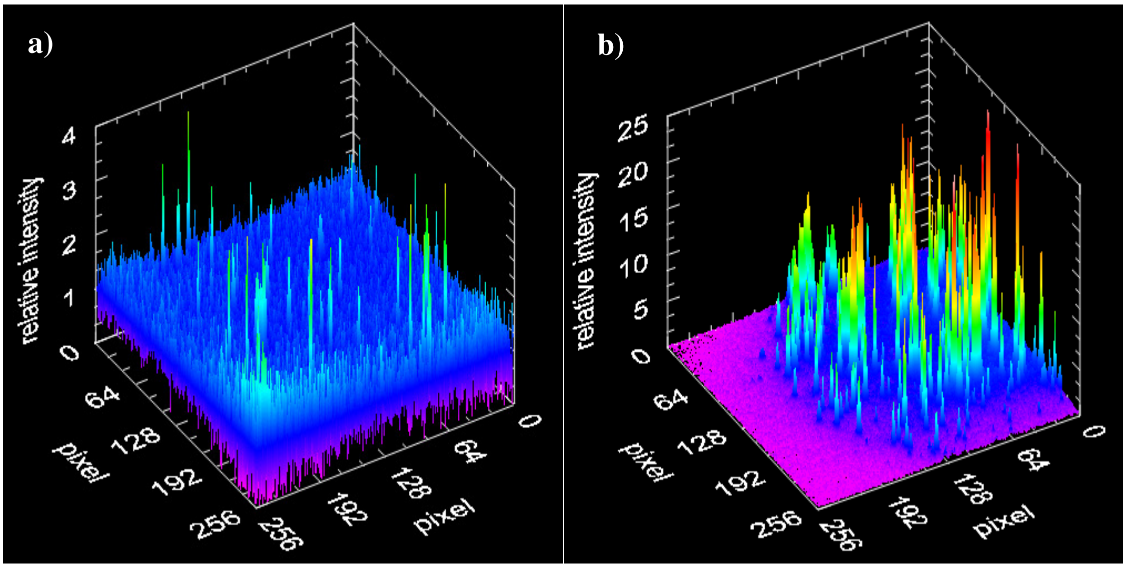

Figure 4.5: Comparison of the oligomers formed at (a) low concentration of β-amyloid(1-40) peptide in solution (2nM), and (b) high concentration of β-amyloid(1-40) peptide in solution (100nM). A relative intensity method (see the text) is used to correct the illumination gradient.

4.4 Discussions

Though there is strong evidence to support the pore formation hypothesis in Alzheimer's disease (11-14), the molecular mechanism of this process remains poorly understood. Thus studies of peptide membrane interactions are critical for understanding the underling mechanism. Since β-amyloid peptides exist at extremely low physiological concentration and can form heterogeneous and dynamic oligomeric species, these studies appear to be very challenging for traditional techniques. In our research, single molecule fluorescence imaging techniques were used to study the peptide membrane interactions.

Our results show that the interactions between β-amyloid(1-40) and anionic membrane start with a very tight and uniform binding of the peptide to the membrane (see figure 4.2 (a)), followed by the formation of different oligomer species in the membrane (see figure 4.4 (b)-(d)). These two different behaviors (uniform binding *vs.* oligomer formation) of peptide membrane interactions suggest that there are two molecular states for the β-amyloid(1-40) peptide in the membrane.

4.4.1 A two-state model for peptide membrane interaction

A two-state model has been proposed for peptide membrane interaction (see figure 4.6) (22, 23). Though the authors originally developed the model specifically for antimicrobial peptides, they have observed that the model would be general and applicable for all peptide membrane interaction.

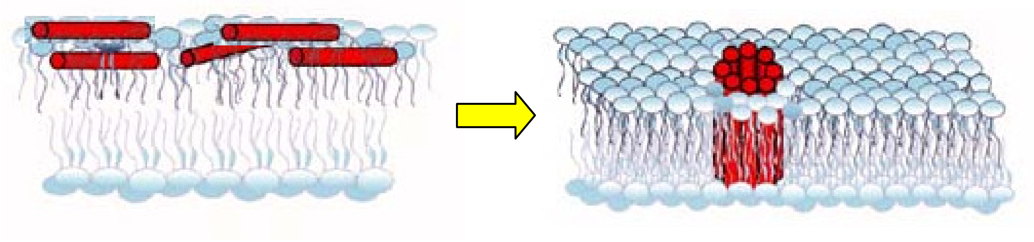

Figure 4.6: Illustration of the two state model.

In this model, membrane interacting peptides exist in two different states: the membrane bound monomeric state and the oligomeric state. It has been shown that these two states are directly related to the peptide/lipid ratio (the number of membrane bound peptide over the number of lipid molecules). At low peptide/lipid ratio, the membrane bound peptide is in the monomeric state, and is at the interface between the hydrophilic head groups and hydrophobic regions, with an orientation parallel to the membrane surface. When the peptide/lipid ratio is above a critical value, the peptide in the membrane is in the oligomeric state, with a perpendicular orientation relative to the membrane surface.

Our results for β-amyloid(1-40) interacting with anionic membranes showed good agreement with the two state model. During the initial incubation of β-amyloid with the membrane (typically corresponding to a lower peptide/lipid ratio), all the membrane bound peptide is in the mobile state and is evenly distributed in the membrane with a high binding affinity. Since the peptide was freshly dissolved for all the experiments, it was highly likely to be a monomer upon binding to the membrane. When β-amyloid(1-40) was further incubated with the membrane (typically corresponding a higher peptide/lipid ratio), the appearance of the oligomers in the membrane indicated these peptides were in a second state, the oligomeric state. According to the two-state model, the peptide in the oligomeric state is oriented perpendicularly to the membrane. This perpendicular orientation may explain the lack of mobility of these oligomers in the membrane. Since the length of the oligomeric peptide is larger than the thickness of the membrane, oligomers spanning through the membrane are likely to be anchored by the underneath glass substrate.

4.4.2 Surface density of the membrane bound mobile peptide

Our results show that for uniform binding of β-amyloid(1-40) to the membrane, membrane saturation occurs at extremely low peptide/lipid ratio. Thus, the fraction of the peptide in solution that binds to the membrane is small. Since the membrane-bound peptide molecules are mobile and are evenly distributed, they are seen as elevated fluorescence backgrounds in the image (see figure 4.4 (a)). Thus by comparing the intensity of the fluorescence background with a standard, the surface density of the mobile peptide in the membrane can be estimated. The standard we used in this work is HiLyte Fluor^{TM} 488, the same fluorophore which was labeled on β-amyloid(1-40) peptide.

In order to get the fluorescence intensity of the standard, we immobilized HiLyte Fluor^{TM} 488 fluorophores on the coverglass surface (see figure 4.7 (a)). Due to the uneven illumination in the imaging, the fluorescence intensities of the 124 collected fluorophores were adjusted according to the illumination gradient. The same adjustments were done for the fluorescence from the background pixels representing the membrane bound β-amyloid(1-40). Since the labeling of the peptide by the fluorophore does not change the absorption and emission properties of the fluorophores, the ratio of the background fluorescence intensities over the average fluorescence intensities of the individual fluorophores yields the surface density (monomeric units/pixel) of the mobile β-amyloid(1-40) peptide in the membrane. The histogram of the membrane bound mobile peptide density is shown in figure 4.7 (b).

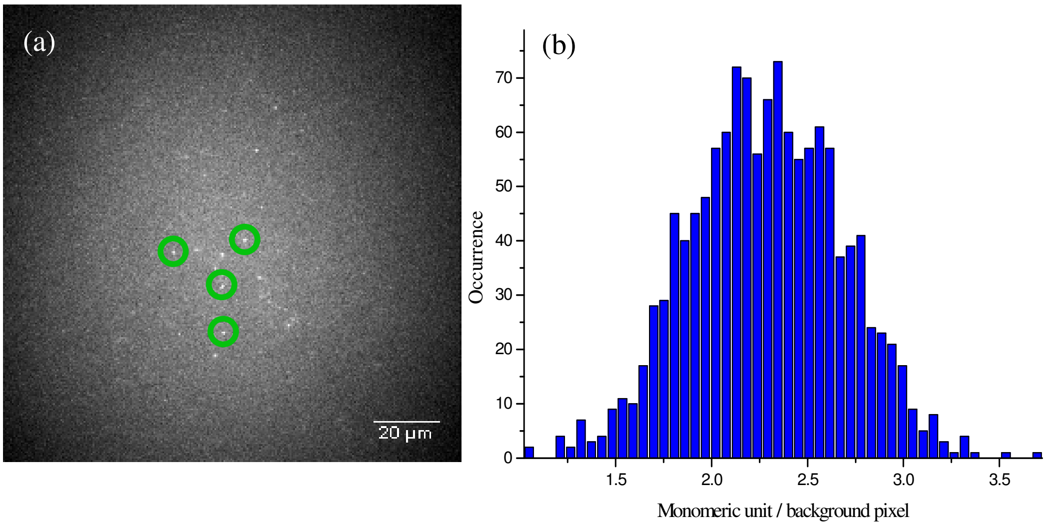

Figure 4.7: Calibration of the fluorescence intensity and estimation of the peptide surface density. (a) shows the image of the immobilized individual HiLyte Fluor^{TM} 488 fluorophores. The fluorescence intensities of these fluorophores were used for surface density estimation of the membrane bound mobile peptide. (b) shows the histogram of the estimated surface density (monomeric units per background pixel).

The estimated density of the membrane bound β-amyloid(1-40) peptide is 2.3±0.4 monomeric units per pixel, which translates to 8.1±1.4 monomeric units/μm^2. The average surface area of a lipid molecule in the membrane is about 70$Å^2$ (28, 29), making for ca 1.43×10^6 lipid molecules/μm^2. Thus the estimated peptide density indicates an extremely low peptide/lipid ratio of about 10^{-5}~10^{-6}. This low peptide/lipid ratio also supports our experimental observation that the fraction of β-amyloid(1-40) that binds to the membrane is extremely small. It could be calculated from this low peptide/lipid ratio that, even with low peptide concentration (e.g. 2nM) in solution, the majority of the peptide (99.8%) was still in solution after the membrane binding sites were saturated. Murphy et. al. have observed a similar low peptide/lipid ratio and tight binding of β-amyloid(1-40) peptide to anionic membrane in surface plasmon resonance experiments (30). Isothermal titration calorimetry experiments conducted in our group also suggest a very tight binding of the peptide to the membrane at low peptide/lipid ratio conditions (31).

4.4.3 Pathways of oligomer formation

It was shown in Results that oligomer formation in the membrane did not start until a uniform binding of β-amyloid(1-40) peptide to the anionic membrane was observed. The concentration dependent oligomer formation suggests there are at least two different pathways for oligomer formation.

In the absence of β-amyloid(1-40) in solution, oligomer formation in the membrane was still observed. This indicates the membrane bound peptide undergoes an internal conversion from the mobile state to the oligomeric state. It was also shown in Results that, with low peptide concentration being present in solution, the internal conversion pathway still dominates the oligomer formation.

Based on the surface density and the diffusion coefficient of the membrane bound mobile peptide (assuming they are monomers), we calculated the two dimensional collision frequency of these mobile peptide in the membrane via the following equation $\Phi = 4\pi C^2 D \ln[(\pi C)^{-1/2} / a]$ (32, 33), in which Φ is the collision frequency, C is the density of the peptide (8.1×10^8/cm^2), D is the diffusion coefficient (2.3×10^{-8}cm^2/sec), and a is the distance between adjacent peptide within β-amyloid(1-40) oligomers. From the sizes of the oligomeric pore reported in the literature (13, 16), this distance a should be on the order of nanometer. This theoretical calculation on collision frequency yields about 4×10^{10} collisions/cm^2/sec for the monomers diffusing in the membrane, which translates to about 50 collisions/sec for each monomer. It is thus indicated that the internal conversion pathway of oligomer formation is unlikely to be a diffusion controlled process, since the collision frequency between the mobile peptide is much higher than the rate of oligomer formation.

In the presence of a high peptide concentration in solution, however, the rate of oligomer formation in the membrane was found to be much higher. Due to the same surface density of the membrane bound mobile peptide being observed for both high and low peptide concentrations in solution (see figure 4.4 (c) & (d)), the rate of oligomer formation via the internal conversion pathway should be the same as well. This suggests that the internal conversion pathway alone cannot account for the much faster oligomer formation in the membrane. Therefore, a different pathway of oligomer formation must exist, in which a direct insertion of solution peptide into the membrane must be involved. This direct insertion mechanism is highly dependent on the concentration of β-amyloid(1-

40) peptide in solution. Oligomer formation with a low concentration of 2nM solution peptide did not show any contribution from the direct insertion pathway, while with a high concentration of 100nM solution peptide, it was dominated by the direct insertion pathway.

4.4.4 Oligomer size analysis

In the previous discussion we used the fluorescence intensities of HiLyte Fluor^{TM} 488 fluorophores to estimate the surface density of the membrane bound mobile β-amyloid(1-40) peptide. We can further use the estimated surface density to analyze the oligomer sizes via their relative fluorescence intensities (see figure 4.5 (a) & (b)). Since a relative intensity of unity represents 2.3±0.4 monomeric peptide, the size of an oligomer can be estimated as "*(relative intensity – 1)* × *2.3*" monomeric units. Figure 4.8 (a) plots the size histogram of the oligomers formed via the internal conversion pathway (also corresponding to low concentration of β-amyloid(1-40) peptide in solution), and 4.8 (b) plots the size histogram of the oligomers formed via the direct insertion pathway (also corresponding to high concentration of β-amyloid(1-40) peptide in solution). It should be noted that, due to a possible fluorophore self-quenching, the sizes of these oligomers might be underestimated, especially for those large ones created via the direct insertion pathway.

A comparison of the histograms in figure 4.8 not only shows the huge size differences between the oligomers formed via different pathways, but also indicated that even via the same pathway, there is a wide range of oligomer species formed in the membrane, especially in the case of the direct insertion pathway. However, among the oligomers formed via the internal conversion pathway, a significant fraction (34.5%) contains smaller species, as highlighted in figure 4.8 (a). These smaller species are estimated to be trimers or tetramers. In fact, high resolution AFM imaging has revealed similar small oligomer species in the membranes as well (13, 16). This suggests that they might be the smallest stable pore structures in the membrane.

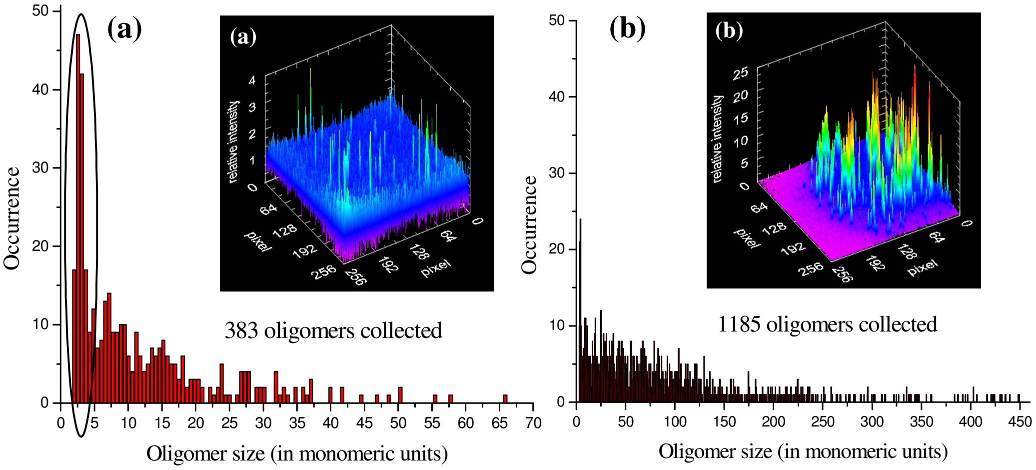

Figure 4.8: Histograms of the oligomers formed in the membrane via (a) the internal conversion pathway, and (b) the direct insertion pathway. A significant fraction (34.5%) of the oligomers, as highlighted in histogram (a), are smaller species (trimers/tetramers).

4.5 Conclusions

While the pore formation hypothesis for β-amyloid peptides has been supported by recent evidence, there is a lack of understanding of the underlying mechanism at the molecular level. In this work, we used single molecule studies to follow the interactions between β-amyloid(1-40) and anionic membrane, and the subsequent oligomer formation.

Our results show that the interaction between β-amyloid(1-40) and anionic membrane starts with an extremely tight binding, and the membrane-bound peptide is diffusing in the membrane. A further incubation of the peptide with the membrane leads to oligomer formation in the membrane, which is concentration dependent. At low concentrations (less than few nM) of β-amyloid(1-40) in solution, a slow conversion pathway from the membrane bound mobile state to the oligomeric state dominates the oligomer formation; while at high peptide concentrations (greater than a few tens of nM), a fast insertion pathway, in which the peptide in solution go directly into the membrane bound oligomeric state, is the major pathway for oligomer formation. It was found that both pathways generate wide ranges of oligomer species in the membrane. However, in the slow conversion pathway, a large fraction of those oligomers exists as small species (trimer/tetramer). Our single molecule studies of β-amyloid(1-40) peptide interacting with supported anionic membranes revealed the details of the peptide-membrane interaction at the molecular level, which are also in good agreement with the two-state model proposed by Huang et. al.

Reference

1. Alzheimer, A., Stelzmann, R. A., Schnitzlein, H. N., and Murtagh, F. R. (1995) An English translation of Alzheimer's 1907 paper, "Uber eine eigenartige Erkankung der Hirnrinde", Clin Anat 8, 429-431.

2. Kidd, M. (1963) Paired Helical Filaments in Electron Microsocpy of Alzheimer's Disease, *Nature 197*, 192-193.

3. Terry, R., Gonatas, N. K., and Weiss, M. (1964) Ultrastructural Studies in Alzheimer's Presenile Dementia, *Am. J. Pathol. 44*, 269-281.

4. Glenner, G. G., and Wong, C. W. (1984) Alzheimer's disease: initial report of the purification and characterization of a novel cerebrovascular amyloid protein, *Biochem. Biophys. Res. Commun. 120*, 885-890.

5. Selkoe, D. J., Abraham, C. R., Podlisny, M. B., and Duffy, L. K. (1986) Isolation of low-molecular-weight proteins from amyloid plaque fibers in Alzheimer's disease, *J. Neurochem. 146*, 1820-1834.

6. Masters, C. L., Simms, G., Weinman, N. A., Multhaup, G., McDonald, B. L., and Beyreuther, K. (1985) Amyloid plaque core protein in Alzheimer disease and Down syndrome, *Proc. Natl. Acad. Sci. USA 82*, 4245-4249.

7. Serpell, L. C., and Smith, J. M. (2000) Direct visualization of the β-sheet structure of synthetic Alzheimer’s amyloid, *J. Mol. Biol. 299*, 225–231.

8. Luhrs, T., Ritter, C., Adrian, M., Riek-Loher, D., Bohrmann, B., Dobeli, H., Schubert, D., and Riek, R. (2005) 3D structure of Alzheimer's amyloid-beta(1-42) fibrils, *Proc. Natl. Acad. Sci. USA 102*, 17342-17347.

9. Hardy, J., and Allsop, D. (1991) Amyloid deposition as the central event in the aetiology of Alzheimer's disease, *Trends Pharmacol. Sci. 12*, 383–88.

10. Mudher, A., and Lovestone, S. (2002) Alzheimer's disease - do tauists and baptists finally shake hands?, *Trends Neurosci. 25*, 22–26.

11. Demuro, A., Mina, E., Kayed, R., Milton, S. C., Parker, I., and Glabe, C. G. (2005) Calcium dysregulation and membrane disruption as a ubiquitous neurotoxic mechanism of soluble amyloid oligomers, *J. Biol. Chem. 280*, 17294-17300.

12. Kourie, J. I., Culverson, A. L., Farrelly, P. V., Henry, C. L., and Laohachai, K. N. (2002) Heterogeneous amyloid-formed ion channels as a common cytotoxic mechanism: implications for therapeutic strategies against amyloidosis, *Cell Biochem. Biophys. 36*, 191-207.

13. Lin, H., Bhatia, R., and Lal, R. (2001) Amyloid beta protein forms ion channels: implications for Alzheimer's disease pathophysiology, *FASEB J. 15*, 2433-2444.

14. Arispe, N., Pollard, H. B., and Rojas, E. (1993) Giant multilevel cation channels formed by Alzheimer disease amyloid beta-protein [A beta P-(1-40)] in bilayer membranes, *Proc. Natl. Acad. Sci. USA 90*, 10573-10577.

15. Dong, Z., Saikumar, P., Weinberg, J. M., and Venkatachalam, M. A. (2006) Calcium in cell injury and death, *Annu. Rev. Pathol. 1*, 405-434.

16. Quist, A., Doudevski, I., Lin, H., Azimova, R., Ng, D., Frangione, B., Kagan, B., Ghiso, J., and Lal, R. (2005) Amyloid ion channels: a common structural link for protein-misfolding disease, *Proc. Natl. Acad. Sci. USA 102*, 10427-10432.

17. Terzi, E., Holzemann, G., and Seelig, J. (1994) Alzheimer beta-amyloid peptide 25-35: electrostatic interactions with phospholipid membranes, *Biochemistry 33*, 7434-7441.

18. Terzi, E., Holzemann, G., and Seelig, J. (1995) Self-association of beta-amyloid peptide (1-40) in solution and binding to lipid membranes, *J Mol Biol 252*, 633-642.

19. McLaurin, J., and Chakrabartty, A. (1997) Characterization of the interactions of Alzheimer beta-amyloid peptides with phospholipid membranes, *Eur J Biochem 245*, 355-363.

20. Del Mar Martinez-Senac, M., Villalain, J., and Gomez-Fernandez, J. C. (1999) Structure of the Alzheimer beta-amyloid peptide (25-35) and its interaction with negatively charged phospholipid vesicles, *Eur J Biochem 265*, 744-753.

21. Bokvist, M., Lindstrom, F., Watts, A., and Grobner, G. (2004) Two types of Alzheimer's beta-amyloid (1-40) peptide membrane interactions: aggregation preventing transmembrane anchoring versus accelerated surface fibril formation, *J Mol Biol 335*, 1039-1049.

22. Huang, H. W. (2000) Action of antimicrobial peptides: two-state model, *Biochemistry 39*, 8347-8352.

23. Huang, H. W. (2006) Molecular mechanism of antimicrobial peptides: the origin of cooperativity, *Biochim Biophys Acta 1758*, 1292-1302.

24. Morrissey Lab Protocol for Preparing Phospholipid Vesicles (SUV) by Sonication, at Avanti Polar Lipids website: http://www.avantilipids.com/pdf/MorrisseyLabProtocolForPrepSuvBySonication.pdf

25. Cremer, P. S., and Boxer, S. G. (1999) Formation and Spreading of Lipid Bilayers On Planar Glass Supports, *J. Phys. Chem. 103*, 2554-2559.

26. Axelrod, D., Koppel, D. E., Schlessinger, J., Elson, E., and Webb, W. W. (1976) Mobility Measurement by Analysis of Fluorescence Photobleaching Recovery Kinetics, *Biophys. J. 16*, 1055-1069.

27. Soumpasis, D. M. (1983) Theoretical Analysis of Fluorescence Photobleaching Recovery Experiments, *Biophys. J. 41*, 95-97.

28. Lantzsch, G., Binder, H., and Heerklotz, H. (1994) Surface area per molecule in lipid/$C_{12}E_n$ membranes as seen by fluorescence resonance energy transfer, *J. Fluoresc. 4*, 339-343.

29. Burke, L. I., Patil, G. S., Panganamala, R. V., Geer, J. C., and Cornwell, D. G. (1973) Surface areas of naturally occurring lipid classes and the quantitative microdetermination of lipids, *J. Lipid Res. 14*, 9-15.

30. Kremer, J. J., Murphy, R. M. (2003) Kinetics of adsorption of beta-amyloid peptide A beta(1-40) to lipid bilayers, *J. Biochem. Bioph. Meth. 57*, 159-169.

31. Kathleen, C. W., and Schauerte, J. A. (unpublished work).

32. Hardt, S. L. (1979) Rates of diffusion controlled reactions in one, two and three dimensions, *Biophys. Chem. 10*, 239-243.

33. Gupte, S., Wu, E., Hoechli, L., Hoechli, M., Jacobson, K., Sowers, A. E., and Hackenbrock, C., R. (1984) Relationship between lateral diffusion, collision frequency, and electron transfer of mitochondrial inner membrane oxidationreduction components, *Proc. Natl. Acad. Sci. USA 81*, 2606-2610.

CHAPTER V

Conclusions

5.1 Introduction

Alzheimer's disease (AD) is an irreversible, progressive, and fatal brain disease that affects millions of people worldwide (1, 2). The formation of amyloid plaques in brain tissues has been the hallmark of the disease (3-5). Since the discovery of β-amyloid peptides as the major components of amyloid plaques in the 1980s (6, 7), numerous studies have confirmed that these peptides are directly involved in the development of Alzheimer's disease (8-10).

Although β-amyloid peptides are neurotoxic, the underlining mechanism remains unclear. Initially, β-amyloid fibrils are believed to be the fundamental cause of Alzheimer's disease (11). However, more recent evidence suggests β-amyloid oligomers are the origin of neurotoxicity, potentially through membrane permeabilization (12-14). Despite the shift of emphasis to β-amyloid oligomers recently, the studies of these small oligomers have been challenging, because they are metastable, occur at low concentration, and are characterized by a high degree of heterogeneity.

In this thesis, we presented a novel single molecule approach to the study of β-amyloid(1-40) oligomers and their interaction with lipid membranes. This single molecule capability provides us a direct and quantitative method to address the heterogeneous and dynamic nature of β-amyloid(1-40) oligomers at their extremely low physiological concentration.

5.2 Thesis summaries

In Chapter II, the advantages of single molecule studies of β-amyloid oligomers are discussed. Following a brief review of the single molecule measurements in general, a new methodology based on single molecule photobleaching is presented. Through this photobleaching method, a direct measure of the oligomer size can be achieved by counting the number of photobleaching steps in the observed fluorescence trajectory. Therefore, in order to have an accurate determination of the photobleaching steps, the recorded photobleaching trajectories are subject to careful analysis. It was shown that the combination of the forward-backward non-linear noise filtering and the photon counting histogram allows for an improved identification of the photobleaching steps.

Chapter II also discusses a dipole orientation model for explaining the observed variability in the size of photobleaching steps. To test this model, a stochastic simulation for generating photobleaching trajectories of individual oligomers was developed. The simulated trajectories clearly resemble the experimental ones by showing very similar photobleaching behaviors. Though the simulation does not prove the proposed model for the origin of the variability in the trajectories, it supports the notion that different dipole orientations are a major contributor to the variations in the photobleaching trajectories.

In Chapter III, we built on the work presented in Chapter II and studied the heterogeneity of β-amyloid(1-40) oligomers. By comparing the oligomer distributions of the unresolved β-amyloid(1-40) mixture and the monomer/dimer fraction from HPLC gel filtration, the ability to differentiate different oligomer distributions using the single molecule approach is demonstrated. Furthermore, a more quantitative and accurate construction of the β-amyloid(1-40) oligomer distribution can be achieved by correcting the bias in the collected single molecule data. Due to the thresholding in data acquisition or image processing, smaller oligomers with less number of fluorophores have a greater tendency to be missed, thus are under-represented in the distribution. The correction to this bias is carried out by the same stochastic simulation described in Chapter II.

The correction via the computer simulation is verified by a control experiment, in which the corrected single molecule distribution of parvalbumin is in good agreement with the mass-spectroscopy distribution. A further analysis of β-amyloid(1-40) oligomers is shown at the end of Chapter III by comparing the corrected single molecule data with the HPLC gel filtration-derived oligomer distribution. The results show good agreement on the oligomer size distribution between the single molecule approach and the gel filtration chromatography approach. Finally, the advantages of the single molecule approach over the conventional gel-filtration chromatography are also discussed.

In Chapter IV, the interaction between β-amyloid(1-40) peptides and supported anionic lipid membranes is studied using the single molecule approach. It was shown that an extremely tight binding between β-amyloid(1-40) peptides and anionic membranes is first observed, followed by the appearance of oligomers in the membrane. While the tightly bound peptides show good mobility in the membrane, the oligomers appear to be stationary. The observation of the two different states, the membrane bound mobile state and the oligomeric state, of β-amyloid(1-40) peptides interacting with anionic membrane suggests good agreement with the two-state model proposed by Huang et al. (15, 16).

A further study of the β-amyloid(1-40) oligomer formation in the membrane shows a strong concentration dependence. At low concentrations (less than few nM) of β-amyloid(1-40) peptides in solution, a slow conversion pathway from the membrane bound mobile state to the oligomeric state dominates the oligomer formation; while at high peptide concentrations (greater than a few tens of nM), a fast insertion pathway, in which the free peptides in solution go directly into the membrane bound oligomeric state, is the major pathway for oligomer formation. It was found that both pathways generate wide ranges of oligomer species in the membrane. However, in the slow conversion pathway, a large fraction of those oligomers exists as small species (trimer/tetramer), which is in agreement with the AFM studies of β-amyloid oligomers (14, 17). Therefore, our single molecule studies reveal the molecular details of how β-amyloid(1-40) peptides interact with supported anionic lipid membranes.

5.3 Future directions

5.3.1 Identification of toxic oligomeric species

Although the single molecule fluorescence microscopy provides a unique approach to the study of β-amyloid oligomer formation in lipid membranes, the identification of the membrane-permeabilizing species remains challenging. Since membrane conductivity has been readily measured by patch clamping or similar techniques, and membrane permeabilization by β-amyloid oligomers has been consistently confirmed by different groups (17-19), the combination of optical detection and conductivity measurement will be able to provide a more complete understanding of β-amyloid neurotoxicity (20).

Figure 5.1 presents the preliminary results of the combined optical detection and conductivity measurements (data obtained by Schauerte, J. A.). In figure 5.1 (a), three consecutive scans of the fluorescently labeled β-amyloid(1-40) oligomers indicate some progression of the oligomers in the membrane. Figure 5.1 (b) shows the corresponding evolution of the membrane conductivity, in which a significant increase in conductance was observed during the third scan.

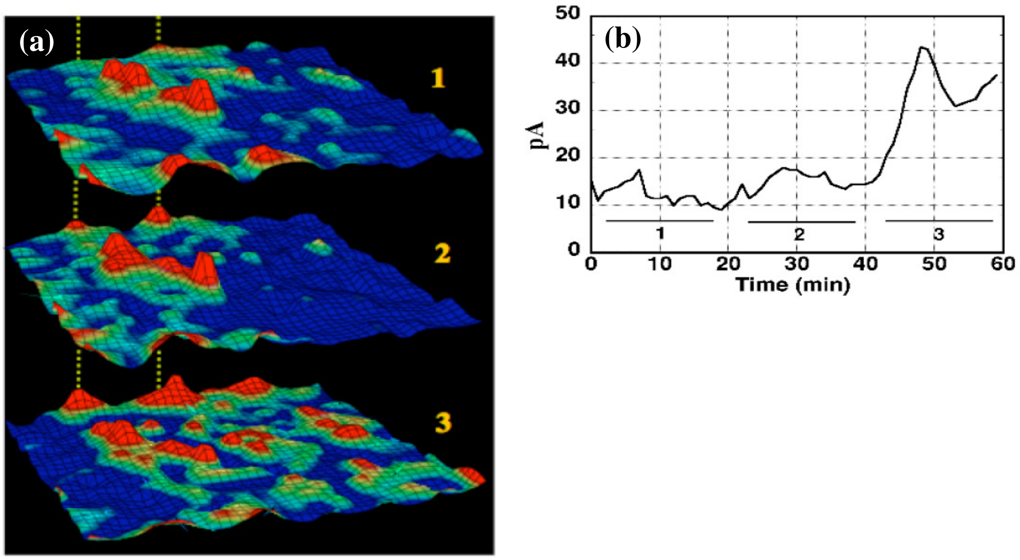

Figure 5.1: Preliminary results of the combined optical detection and conductivity measurements. (a) shows three consecutive scans of the fluorescently labeled β-amyloid(1-40) oligomers in the membrane. (b) shows the corresponding evolution of the membrane conductivity. (data in courtesy of Schauerte, J. A.)

5.3.2 *In vivo* studies of β-amyloid oligomers

In the work presented in this thesis, artificial membranes (e.g. POPC and POPG) were used in the study of peptide-membrane interaction. While model membranes simplify the system and provide the freedom to manipulate the lipid composition, in vivo studies give a more biologically relevant approach for the study of β-amyloid neurotoxicity. Figure 5.2 shows the preliminary results of single molecule studies of β-amyloid(1-40) peptides binding to live cells (SH-SY5Y neuroblastoma cells, data obtained by Johnson, R.).

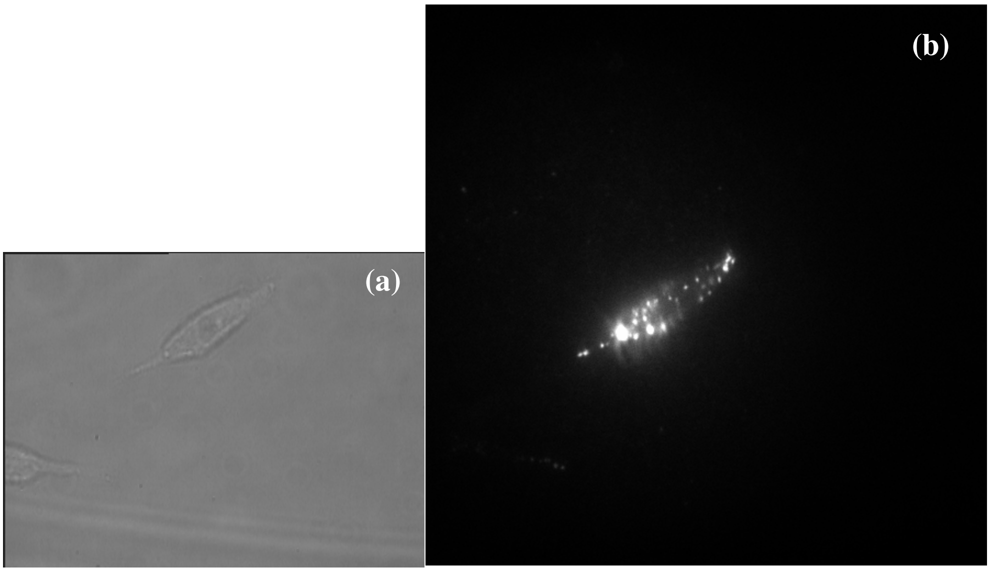

Figure 5.2: Preliminary results of single molecule studies of β-amyloid(1-40) peptides binding to live cells. (a) shows the phase contrast image of the cell. (b) shows the fluorescence image of β-amyloid(1-40) oligomers binding to the cell. (data in courtesy of Johnson, R.)

5.3.3 Closing

In closing, this thesis has opened up new opportunities for the study of Alzheimer's disease at the molecular level. It has been shown in this thesis that, single molecule technique is a useful new tool for detecting, monitoring, and characterizing β-amyloid oligomers at their physiological concentration. The methods developed and utilized in this thesis hold promise for the fundamental insights into the early stage of Alzheimer's disease, and pave the way for further studies on amyloid diseases.

References

1. (2009) National Institute on Aging.

2. (2007) World population prospects: the 2006 revision, highlights, *Working Paper No. ESA/P/WP.202. Population Division, Department of Economic and Social Affairs, United Nations.*

3. Alzheimer, A., Stelzmann, R. A., Schnitzlein, H. N., and Murtagh, F. R. (1995) An English translation of Alzheimer's 1907 paper, "Uber eine eigenartige Erkankung der Hirnrinde", Clin Anat 8, 429-431.

4. Kidd, M. (1964) Alzheimer's Disease: An Electron Microscopic Study, *Brain 86*, 309-310.

5. Terry, R., Gonatas, N. K., and Weiss, M. (1964) Ultrastructural Studies in Alzheimer's Presenile Dementia, *Am. J. Pathol. 44*, 269-281.

6. Glenner, G. G., and Wong, C. W. (1984) Alzheimer's disease: initial report of the purification and characterization of a novel cerebrovascular amyloid protein, *Biochem. Biophys. Res. Commun. 120*, 885-890.

7. Selkoe, D. J., Abraham, C. R., Podlisny, M. B., and Duffy, L. K. (1986) Isolation of low-molecular-weight proteins from amyloid plaque fibers in Alzheimer's disease, *J. Neurochem. 146*, 1820-1834.

8. Revesz, T., Ghiso, J., Lashley, T., Plant, G., Rostagno, A., Frangione, B., and Holton, J. L. (2003) Cerebral amyloid angiopathies: a pathologic, biochemical, and genetic view, *J. Neuropathol. Exp. Neurol. 62*, 885–898.

9. Harper, J. D., and Lansbury, P. T., Jr. (1997) Models of amyloid seeding in Alzheimer's disease and scrapie: mechanistic truths and physiological consequences of the time-dependent solubility of amyloid proteins, *Annu Rev Biochem 66*, 385-407.

10. Chauhan, N. B., and Siegel, G. J. (2002) Reversal of amyloid beta toxicity in Alzheimer's disease model Tg2576 by intraventricular antiamyloid beta antibody, J Neurosci Res 69, 10-23.

11. Hardy, J., and Allsop, D. (1991) Amyloid deposition as the central event in the aetiology of Alzheimer's disease, *Trends Pharmacol. Sci. 12*, 383–88.

12. Demuro, A., Mina, E., Kayed, R., Milton, S. C., Parker, I., and Glabe, C. G. (2005) Calcium dysregulation and membrane disruption as a ubiquitous neurotoxic mechanism of soluble amyloid oligomers, *J. Biol. Chem. 280*, 17294-17300.

13. Kayed, R., Sokolov, Y., Edmonds, B., McIntire, T. M., Milton, S. C., Hall, J. E., and Glabe, C. G. (2004) Permeabilization of lipid bilayers is a common conformation-dependent activity of soluble amyloid oligomers in protein misfolding diseases, *J. Biol. Chem. 279*, 46363-46366.

14. Lin, H., Bhatia, R., and Lal, R. (2001) Amyloid beta protein forms ion channels: implications for Alzheimer's disease pathophysiology, *FASEB J. 15*, 2433-2444.

15. Huang, H. W. (2000) Action of antimicrobial peptides: two-state model, *Biochemistry 39*, 8347-8352.

16. Huang, H. W. (2006) Molecular mechanism of antimicrobial peptides: the origin of cooperativity, *Biochim Biophys Acta 1758*, 1292-1302.

17. Quist, A., Doudevski, I., Lin, H., Azimova, R., Ng, D., Frangione, B., Kagan, B., Ghiso, J., and Lal, R. (2005) Amyloid ion channels: a common structural link for protein-misfolding disease, *Proc. Natl. Acad. Sci. USA 102*, 10427-10432.

18. Kourie, J. I., Culverson, A. L., Farrelly, P. V., Henry, C. L., and Laohachai, K. N. (2002) Heterogeneous amyloid-formed ion channels as a common cytotoxic mechanism: implications for therapeutic strategies against amyloidosis, *Cell Biochem. Biophys. 36*, 191-207.

19. Arispe, N., Pollard, H. B., and Rojas, E. (1993) Giant multilevel cation channels formed by Alzheimer disease amyloid beta-protein [A beta P-(1-40)] in bilayer membranes, *Proc. Natl. Acad. Sci. USA 90*, 10573-10577.

20. Schauerte, J. A., Wong, P. T., Wisser, K. C., Ding, H., Steel, D. G., and Gafni, A., Simultaneous Single Molecule Fluorescence and Conductivity Studies Reveal Distinct Classes of Aβ Species on Lipid Bilayers (unpublished results).

APPENDIX A

Noise of Photon Detectors

A.1 Ideal detector

For an ideal detector, shot noise is the only noise source. Shot noise reflects the stochastic nature of photon flux, and follows a Poisson distribution.

If N_{pi} represents the received photon counts in the i^{th} unit time ($i = 1, 2, \ldots, I$),

$$\text{Signal Average} = \overline{N_p} = \sum_{i=1}^{I} N_{pi} \Big/ I$$

$$\text{Noise} = \sigma_{ideal} = \sqrt{\frac{\sum_{i=1}^{I}(N_{pi} - \overline{N_p})^2}{I}} = \sqrt{\overline{N_p}}$$

$$\text{Signal/Noise} = \overline{N_p} \Big/ \sqrt{\overline{N_p}} = \sqrt{\overline{N_p}}$$

A.2 Single-photon-counting (Geiger mode) avalanche photodiode

For a single-photon-counting (Geiger mode) avalanche photodiode, besides the shot nose, there is one additional noise source, dark noise. Dark noise is the noise from the detector in the absence of light, and is typically thermally induced. The avalanche photodiode (SPCM-AQ 161, PerkinElmer Optoelectronics, Canada) used in our experiments has an extremely low dark current of 50 counts per second.

$$\text{Noise} = \sigma_{APD} = \sqrt{\sigma_{shot}^2 + \sigma_{dark}^2} = \sqrt{\overline{N_p} + \sigma_{dark}^2}$$

$$\text{Signal/Noise} = \overline{N_p} \Big/ \sqrt{\overline{N_p} + \sigma_{dark}^2}$$

A.3 CCD camera

For a Charge-Coupled Device (CCD), the read-out noise dominates the noise source. Since most scientific grade CCD cameras are deeply cooled (<-70℃), the dark noise (thermal noise) is typically very low. Therefore, the sensitivity of a CCD camera is mostly determined by the read-out noise (~10 photoelectrons per reading).

If N_{pi} represents the received counts in photoelectrons, and N_{ci} represents the received counts in camera units, in the i^{th} unit time ($i = 1, 2, \ldots, I$),

$N_{ci} = {}^{N_{pi}}\!/_{G}$, in which G is the pre-amplification gain, representing the number of photoelectrons needed to register one count in camera units. G is determined by the A/D converter of the camera.

$$\text{Signal Average (in camera counts)} = \overline{N_c} = {}^{\overline{N_p}}\!/_{G}$$

$$\text{Shot noise (in camera counts)} = \sigma_{shot} = \sqrt{\frac{\sum_{i=1}^{I}(N_{pi} - \overline{N_p})^2}{G^2 \cdot I}} = \sqrt{\frac{\overline{N_p}}{G^2}} = \sqrt{\frac{\overline{N_c}}{G}}$$

$$\text{Noise (in camera counts)} = \sigma_{CCD} = \sqrt{\sigma_{shot}^2 + \sigma_{read-out}^2} = \sqrt{\frac{\overline{N_c}}{G} + \frac{\sigma_{read-out}^2}{G^2}}$$

$$\text{Signal/Noise} = {}^{\overline{N_c}}\!\Big/_{\sqrt{\frac{\overline{N_c}}{G} + \frac{\sigma_{read-out}^2}{G^2}}} = {}^{\overline{N_p}}\!\Big/_{\sqrt{\overline{N_p} + \sigma_{read-out}^2}}$$

A.4 Electron-Multiplying CCD camera

In order to increase sensitivity (which is limited by the read-out noise in a conventional CCD camera), Electron-Multiplying CCD cameras amplify the signal before the read-out takes place, so that the read-out noise can be effectively suppressed. This is a new type of camera which allows high sensitivity measurements to be taken at relatively high frame rates. However, the amplification process also brings additional noise, which is characterized by a multiplicative noise factor *F*.

$N_{ci} = \frac{M}{G} N_{pi}$, in which *M* is the amplification to the signal, and *G* is the pre-amplification gain.

Signal Average (in camera counts) $= \overline{N_c} = \frac{M}{G}\overline{N_p}$

Shot noise (in camera counts) =

$$\sigma_{shot} = \sqrt{\frac{F^2 \cdot M^2}{G^2} \frac{\sum_{i=1}^{I}(N_{pi} - \overline{N_p})^2}{I}} = \sqrt{\frac{F^2 \cdot M^2}{G^2}\overline{N_p}} = \sqrt{\frac{F^2 \cdot M}{G}\overline{N_c}}$$

Noise (in camera counts) = $\sigma_{EMCCD} = \sqrt{\sigma_{shot}^2 + \sigma_{read-out}^2} = \sqrt{\frac{F^2 \cdot M}{G}\overline{N_c} + \frac{\sigma_{read-out}^2}{G^2}}$

When the amplification *M* is very large, $\sigma_{EMCCD} \approx F \cdot \sqrt{\frac{M}{G}\overline{N_c}}$

Signal/Noise $= \sqrt{\frac{G}{F^2 \cdot M}} \cdot \sqrt{\overline{N_c}} = \frac{1}{F}\sqrt{\overline{N_p}}$

The Electron-Multiplying CCD camera (iXon DV887ACS-BV, Andor Technology, Allentown, NJ) used in our lab has a read-out noise of 53.6 photoelectrons per reading, a pre-amplification of 15.4 photoelectrons per camera count, and a noise factor of 1.56 (all the parameters were measured in the lab).

A.5 Signal/Noise Comparison

Figure A.1 shows the theoretical Signal/Noise ratio comparison of the different detectors described above. It clearly shows that, for weak light detection (such as for single molecule fluorescence measurements, the signal is often <50 detected photons per unit time), both single-photon-counting APD and Electron-Multiplying CCD camera have fairly good signal/noise ratios. However, it should be noted that, only the primary sources of noise are included in the above Signal/Noise analysis. In reality, most detectors have much more complicated noise sources, such as CCD cameras are subject to various kinds of internally and externally generated noise and other spurious signals as well. Furthermore, beside photon detectors, there are other critical components that can affect the signal and/or noise in the measurements, such as objective, fluorophore, ect.

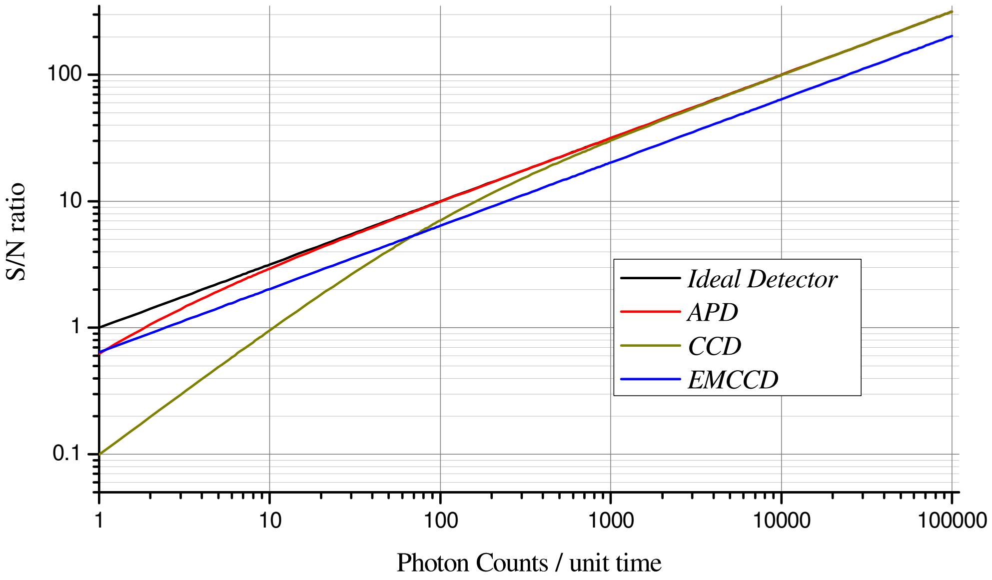

Figure A.1: Theoretical Signal/Noise ratio comparison of different detectors. A unit time of 25ms, which is a typical exposure time in single molecule fluorescence measurements, is used in the plot.

APPENDIX B

Image Processing for Single Molecule Identification

B.1 Thresholding

Thresholding, as a method of image processing, is to segment an image into two groups, object and background. During the thresholding process, each pixel in the image is marked as either "object" (e.g. when the pixel value is greater than the threshold) or "background" (e.g. when the pixel value is less than or equal to the threshold).

For single molecule detection, thresholding is one of the most commonly used methods for fluorophore identification in images/videos. However, due to the presence of an illumination gradient in our images, which is caused by both the Gaussian profile of the laser beam and the TIRF geometry, the conventional thresholding, in which a global threshold is used for all the pixels, does not perform well (see figure B.1).

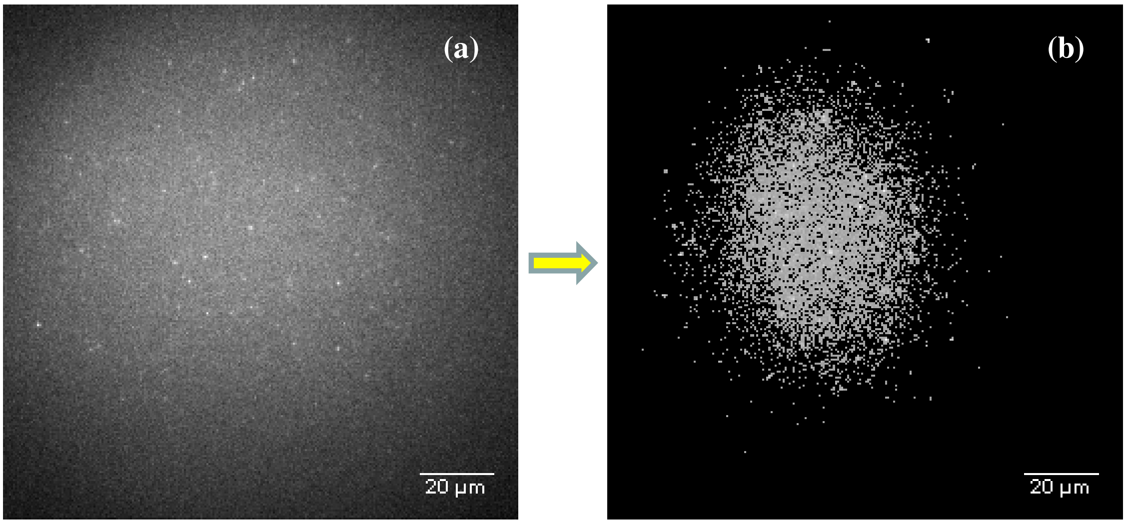

Figure B.1: Conventional thresholding fails due to the presence of an illumination gradient. (a) shows the raw image (the first frame in a photobleaching video). The bright dots in the image are individual β-amyloid(1-40) oligomers. (b) shows the image after thresholding.

B.2 Adaptive thresholding

Based on the rational that smaller regions, such as 9x9 pixels regions in our images, are more likely to have approximately uniform illumination, an adaptive thresholding technique (also called dynamic thresholding) is used in our data analysis.

During the adaptive thresholding process, a “local S/B (signal to background)” ratio for each pixel in the image is first calculated. This “local S/B” indicates how a pixel is compared to its local surrounding, and is calculated as the ratio of the pixel value over the surrounding (e.g. 9x9 pixels) average. This removes the signal variations in the image due to the illumination gradient, and generates a “Local S/B image” (see figure B.2 (b)). The histogram of this “Local S/B image” is shown in figure B.2 (c), which contains a normal distribution around unity, with a few outliers on the right. The unity corresponds to the background pixels and the outliers correspond to the β-amyloid(1-40) oligomers. Then a conventional thresholding is applied to this “Local S/B image”, with the selection of the threshold based on the histogram (e.g. a selection of 4σ (σ is the standard deviation of the normal distribution) can reject 99.9937% of the background pixels). After the thresholding, the identified β-amyloid(1-40) oligomer are shown in figure B.2 (d).

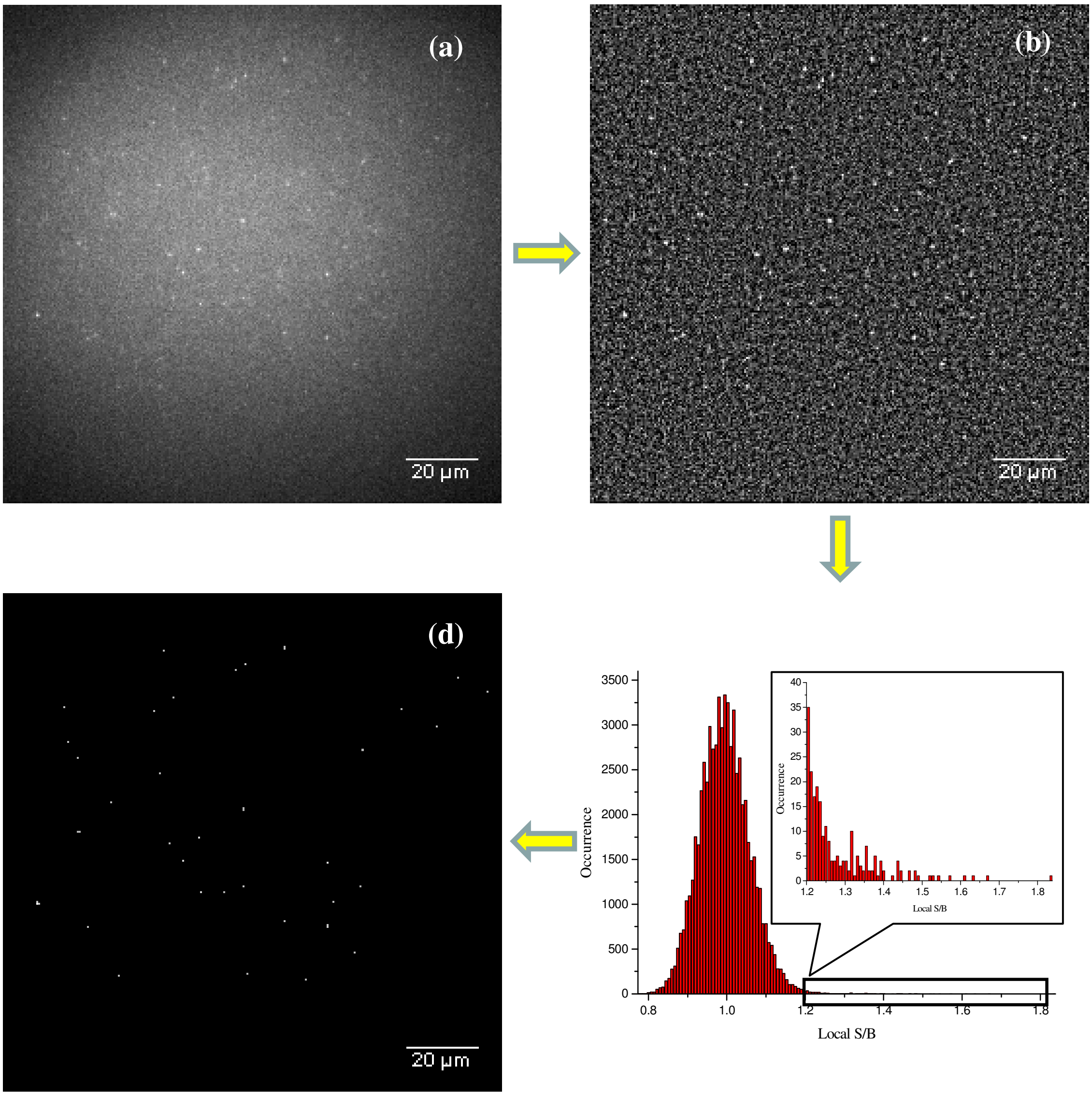

Figure B.2: Adaptive thresholding for identifying and locating the individual β-amyloid(1-40) oligomers. (a) shows the raw image. (b) show the Local S/B image. (c) shows the histogram of image (b). (d) shows the thresholded image.

B. 3 Photobleaching trajectory extraction

Once the β-amyloid(1-40) oligomers are identified in the image, their photobleaching trajectories can be readily extracted from the photobleaching video.

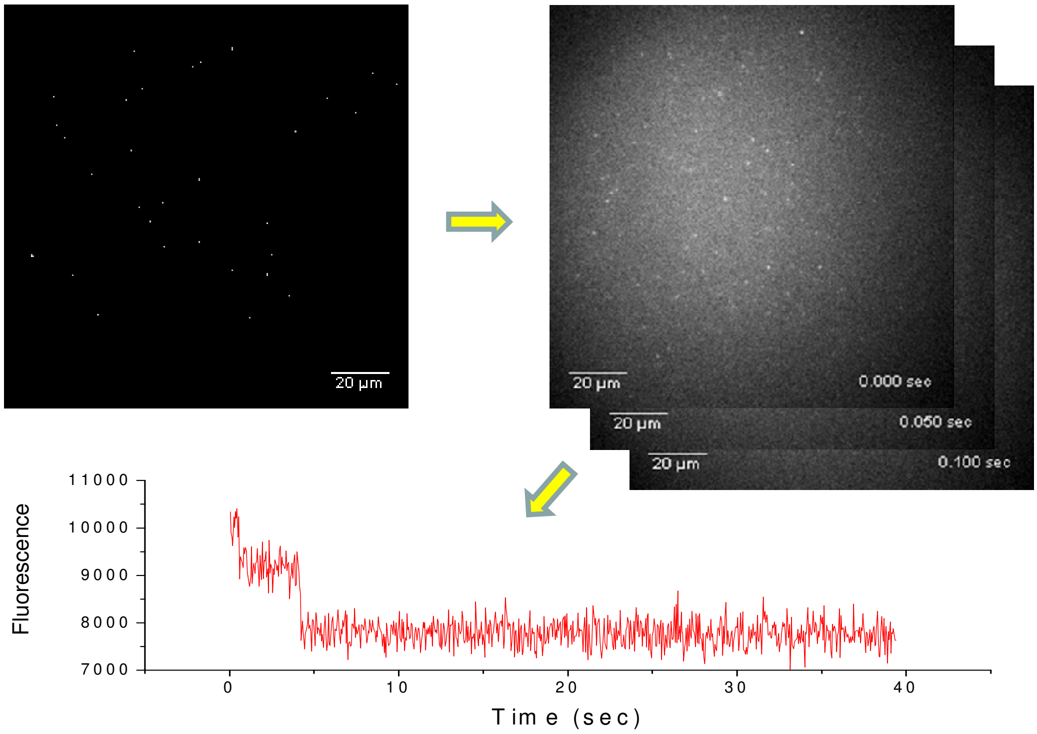

Figure B.3: Photobleaching trajectories are extracted from the photobleaching video.

APPENDIX C

Stochastic Simulation of Single Molecule Photobleaching: An Example

As an example of the stochastic simulation, the photobleaching trajectory of a trimer is randomly generated and illustrated below. For each step in the simulation, the generated photobleaching trajectory is updated in figure C.4.

C.1 The random generation of the photobleaching times

Photobleaching times are randomly assigned to the three fluorophores in the trimer based on the exponential probability distribution $p = (1/\tau)\exp(-t/\tau)$, in which τ is the preset photobleaching lifetime, reflecting the photostability of the fluorophores that are maximally excited. The three fluorophores are indicated as a, b, and c in figure C.1.

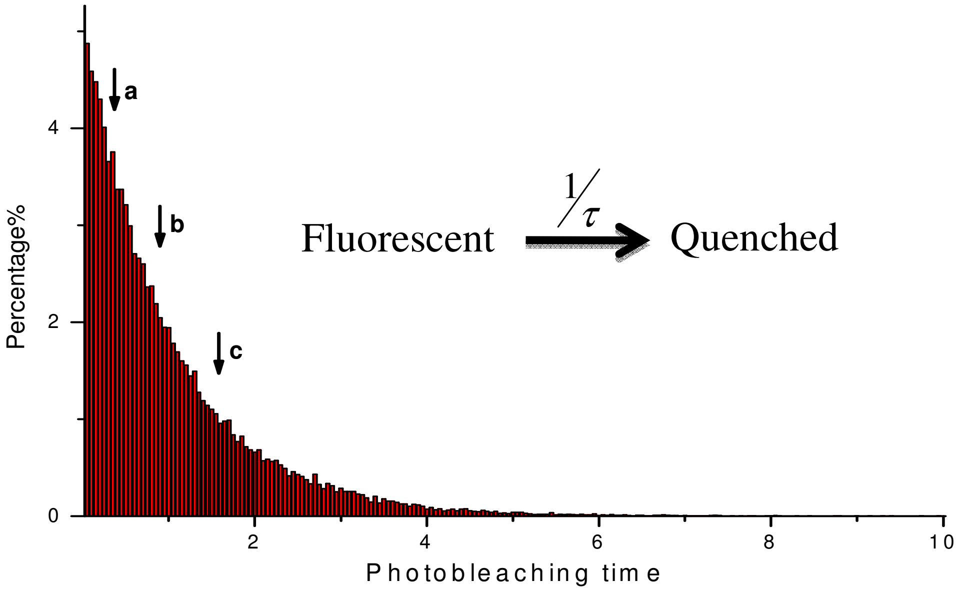

Figure C.1: The exponential probability distribution of the photobleaching time.

C.2 The random generation of the position of the trimer

A random position γ relative to the center of the Gaussian beam/focus is assigned to the trimer. This random generation of the position (with a preset upper limit) is based on a uniform probability of the oligomers being deposited on the coverglass. Therefore, both the photobleaching times and the fluorescence intensities of the fluorophores in the trimer are adjusted according to the excitation intensity $\exp(-\gamma^2/2)$ (see figure C.2).

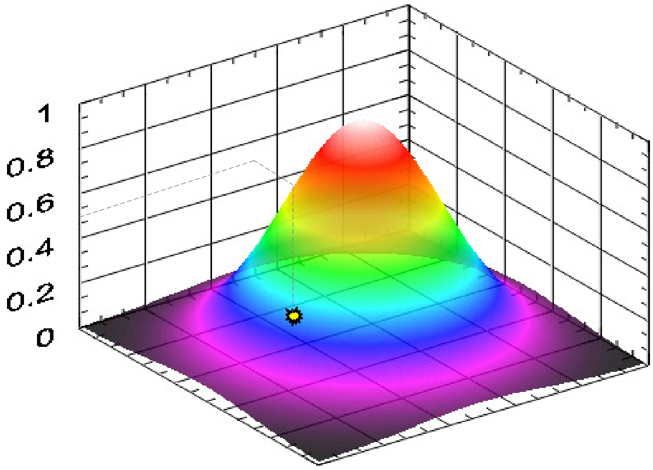

Figure C.2: The position of the trimer in the Gaussian beam/focus.

C.3 The random generation of the dipole orientations of the fluorophores

A fixed dipole orientation angle θ (relative to the coverglass surface) is randomly assigned to each fluorophore in the trimer (based on a flat distribution) (see figure C.3). According to the different dipole orientations of the fluorophores, each fluorophore's photobleaching time is adjusted by $\left[\cos^2(\theta)\right]^{-1}$, and the fluorescence intensity is adjusted by $\left[\cos^4(\theta)\right]^{-1}$.

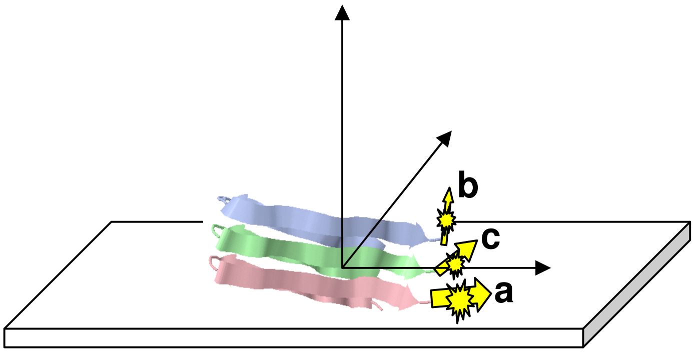

Figure C.3: The dipole orientations of the three fluorophores in the trimer.

C.4 Addition of Poisson noise to the trajectory

Figure C.4 shows the generated photobleaching trajectory after each step.

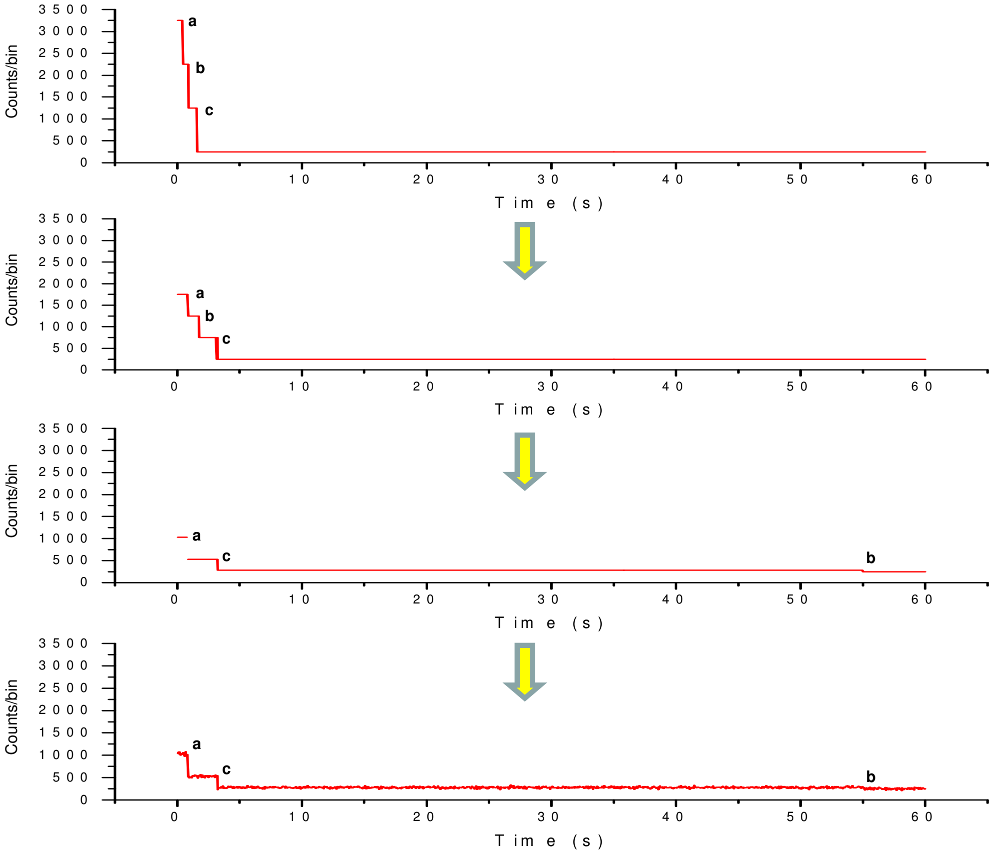

Figure C.4: The generated or adjusted photobleaching trajectory after each step.